Anisotropy & Self-assembly. A walk through intricate free-energy landscapes.

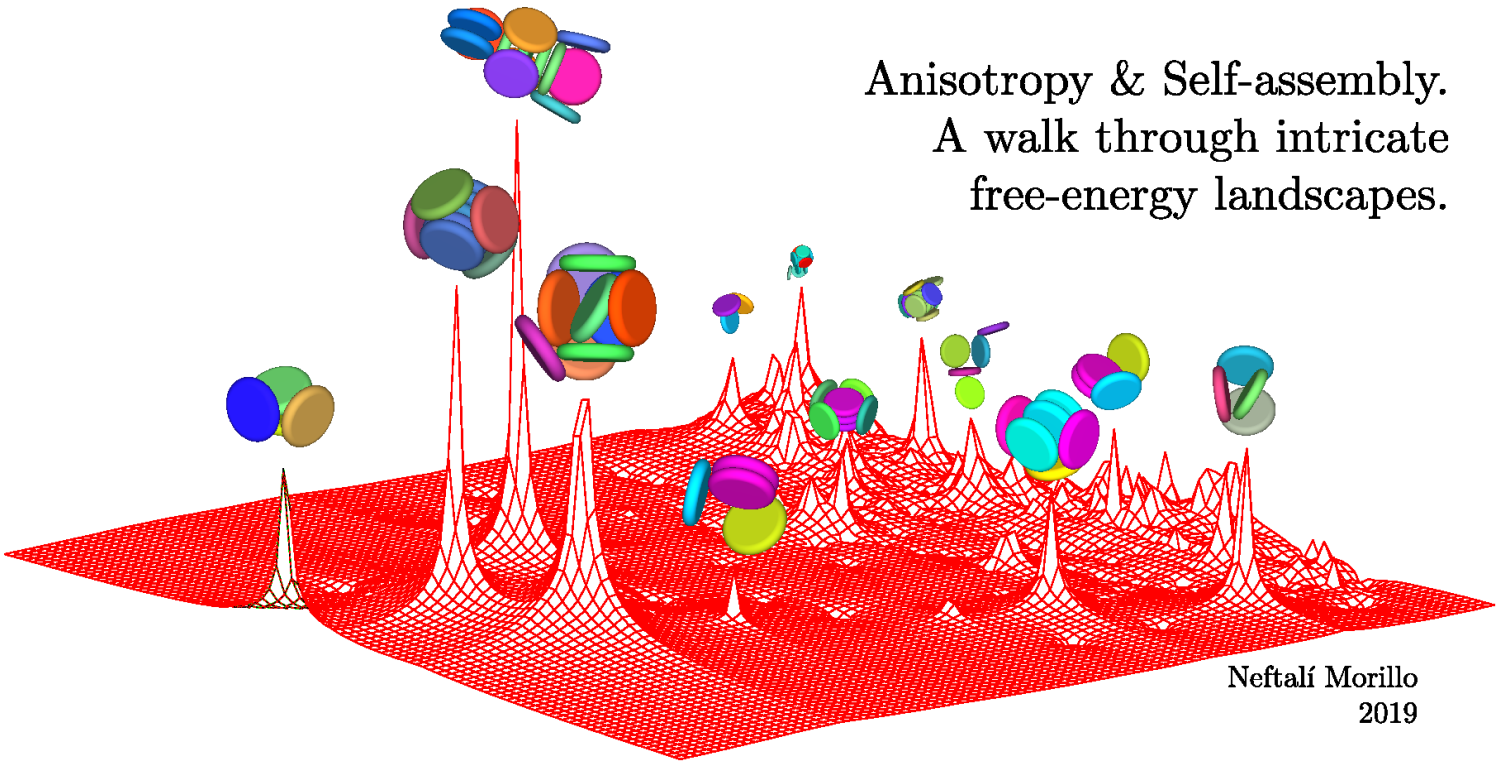

Neftalí Morillo
2019

Anisotropy & Self-assembly.
A walk through intricate free-energy landscapes.

Juan Neftalí Morillo García

May 13, 2019

Abstract

The selective aggregation of discotic molecules or colloids is the key factor behind the outstanding properties of many substances, of natural or synthetic origins, like clays used in cosmetics and other coatings or polycyclic aromatic hydrocarbons employed in optoelectronic devices. These are just a two examples from a plethora of substances where the interplay between shape anisotropy and interaction anisotropy is at hand in the constituents provoking the emergence of interesting macroscopic features. Keeping that perspective, this thesis is written with the firm belief that a better understanding of the aggregation and self-assembly processes will render in better technological applications. In that sense, the problem to be tackled is very broad in terms of number of variables implied. Since we are investigating the reach of specific properties of individual particles into the behaviour of the substance they compose. Being the specific aim of this thesis to characterize the importance of anisotropy in shape and interactions in the self-assembly processes. To accomplish this, computer simulation of discotic particles modeled using coarse grain models were run on model systems. A reasonable strategy to perform them was to fix as many variables as possible for each study, as it was done in the first half of this thesis. Firstly a system of soft particles is used to gain some insight into the effect of shape anisotropy on the diffusion in structured fluids, comparing the diffusion of equivalent pro-

late and oblate particles. Then with a fixed oblate shape anisotropy, it is pointed out the decisive role played by the anisotropy in the interaction potential for the internal structure of aggregates and the location of the phase transitions. This knowledge is then applied in the second half of the thesis, where the dynamics of particles are studied with different interactions potentials during aggregation. Finally, to exploit every thing learned, it is proposed and simulated a clay model.

Resumen

La agregación selectiva de moléculas o coloides discoticos es el factor clave detrás de las propiedades sobresalientes de muchas sustancias, de origen natural o sintético, como las arcillas utilizadas en cosméticos y otros recubrimientos o hidrocarburos aromáticos policíclicos empleados en dispositivos optoelectrónicos. Estos son solo dos ejemplos de una gran cantidad de sustancias en las que la interacción entre la anisotropía de forma y la anisotropía de interacción van de la mano en los constituyentes provocando el surgimiento de de características macroscópicas interesantes. Manteniendo esa perspectiva, esta tesis está escrita con la firme convicción de que una mejor comprensión de la agregación y los procesos de autoensamblado se traducirán en mejores aplicaciones tecnológicas. En ese sentido, el problema a ser abordado es muy amplio en términos del número de variables implícadas. Ya que estamos investigando el alcance de las propiedades específicas de las partículas individuales en el comportamiento de la sustancia que componen. Siendo el objetivo específico de esta tesis caracterizar la importancia de la anisotropía en su forma e interacciones en los procesos de autoensamblaje. Para lograr esto, la simulación por computadora de partículas discóticas modeladas usando modelos de grano grueso se ejecutó en sistemas modelo. Una estrategia razonable para realizarlas fue fijar tantas variables como fuera posible para cada estudio, como se hizo en la primera mi-

tad de esta tesis. En primer lugar, se utiliza un sistema de partículas blandas para obtener una idea del efecto de la anisotropía de la forma en la difusión en fluidos estructurados, comparando la difusión de partículas de prolato y de oblato equivalentes. Luego, con una anisotropía de forma oblata fija, se señala el papel decisivo desempeñado por la anisotropía en el potencial de interacción para la estructura interna de los agregados y la ubicación de las transiciones de fase. Este conocimiento se aplica luego en la segunda mitad de la tesis, donde se estudia la dinámica de las partículas con diferentes potenciales de interacción durante la agregación. Finalmente, para explotar todo lo aprendido, se propone y se simula un modelo de arcilla.

Contents

Chapter 1

Introduction

This chapter aims to serve as a brief contextualization of the work, as well as a compendium of short descriptions of techniques and concepts which might be unfamiliar for the reader.

The topics covered in this thesis can be classified in the field that today is called soft-matter, term that since Pierre-Gilles de Gennes spoke of it [1], is used to frame systems whose individual constituents scale from $\sim 1nm$ to $\sim 1\mu m$ and manifest a change in their behaviour when forces in the magnitude of thermal fluctuations are applied. This scale ranges from small organic molecules to viruses, bacteria and cells. Therefore, involves many interesting phenomenons of chemistry and biology, which surround us in our daily lives. Most of the time this involves complex interactions to scaffold bigger structures, a process usually referred to as self-assembly. Even without fully understanding the processes behind initially, humans have exploited these properties throughout history, from clay constructions or simple culinary preparations, such as whipped cream, or mayonnaise, to present optoelectronic devices. This thesis is written with the very ambitious purpose of increasing fundamental knowledge of some

topics of key relevance in the understanding of processes ruling many systems in soft matter, as well as provide the tools to link microscopic features to the final self-assembled structures. Thus help to improve or discover new applications of these materials.

Substances whose constituents are in the mentioned size range experience very interesting phase transitions and coexistences. When the attributes of these materials are in the midway of crystalline solids and liquids, those are coherently named liquid crystals (LCs). Forming in many cases what is called mesophases, because they arrange spontaneously with partial degree of orientational or positional ordering of their constituents, generally called mesogens.

Present technology has taken a bottom up approach to fine-tune their specific macroscopic properties [2], making them decisive in the fabrication of many devices. LCs are well known to be used in displays, but with the plethora of possible compositions yet to be explored, the number of applications keeps increasing every day. Many of them are still optical, like photonic crystals [3, 4], but they can also have interesting charge transport properties [5] making them suitable for solar cells, organic light-emitting diodes, field-effect transistors, thermometers, lasers, and nanowires [6–10].

Most of these applications make use of molecular LCs, namely LCs whose mesogens are molecules. But to study LCs scientists usually resort to bigger particles named colloids (from the Greek word $\kappa\omega\lambda\lambda\alpha$, which means glue), since Graham coined the term in 1861 [11], when he observed how some gluey substances could not diffuse through a membrane. Colloidal LCs, consist of colloidal particles in suspension and are of key relevance to understanding a number of processes at the molecular scales that are usually too fast to be studied by conventional microscopy. In other words, colloidal LCs are excellent model systems to unveil the behaviour of molecular LCs. However, we should

always bear in mind that time scales will change accordingly when we compare the evolution of any magnitude e.g. relaxation times [12], having a significant impact on experiment design.

The dynamics of colloidal systems were first reported by Robert Brown In 1827, the Scottish botanist, on his study about pollen grains suspended in water and moving as persistently perturbed by random forces of uncertain nature [13]. Almost eighty years later, Einstein realized that this intriguing movement, was due to the thermal energy that colloidal particles dissipate as a result of their collisions with the surrounding solvent molecules [14]. Einstein's theoretical intuitions, together with the work by Smoluchowski [15] and Langevin [16], were corroborated experimentally by Perrin in 1909 [17]. At that time the only possibility to test a model was to perform an experiment, but thanks to the development of computer technology, simulations have gained momentum. Now they play a decisive role in scientific research, because they provide information often unreachable for technical reasons and allows us to avoid dangerous experiments or reduce costs. In particular, all the studies of this thesis were performed with techniques of molecular simulation, which we discuss further below, given that the rest of this introductory chapter is dedicated to brief descriptions of the tools and methods used trough out this thesis.

1.1 Thermodynamics and Statistical Mechanics

Thermodynamics was born as an experimental discipline and retain most if this character to date. If we now take a thermodynamic approach to describe a system we will be omitting any a microscopic description of it to understand its macroscopic behaviour. Meanwhile, statistical mechanics will help us to fill this gap, linking microscopic features of the system to macroscopic variables easily measurable in a laboratory.

A thermodynamic state is controlled by a few variables. In the absence of an external field, for a multicomponent system the first principle of thermodynamics can be expressed like:

$$dU = TdS - pdV + \sum_i \mu_i dN_i \tag{1.1}$$

This equation shows the change in energy dU is controlled by a change in entropy dS, a change in volume dV and another one in the number of particle of each specie dN_i (all the extensive variables). Just holding their associated intensive variables (temperature T, pressure p and chemical potential of each specie μ_i). Starting from here the equilibrium conditions of the system can be derived [18], maximum entropy or minimum energy. Likewise, applying the Legendre transformation we can derive the rest of the thermodynamic potentials, allowing us to present the same thermodynamic state through the most suitable variables to our purposes, yielding:

Enthalpy

$$H = U + pV \tag{1.2}$$

Helmholtz free-energy

$$F = U - TS \tag{1.3}$$

and Gibbs free energy

$$G = U + pV - TS \tag{1.4}$$

Any of the potentials can be used as a fundamental equation of the system to determine its stability conditions as a function of the system variables. Starting from Helmholtz free-energy we can derive the entropy, pressure and chemical

potentials of the system like:

$$S = -\left(\frac{\partial F}{\partial T}\right)_{V,N_i} \tag{1.5}$$

$$p = -\left(\frac{\partial F}{\partial V}\right)_{T,N_i} \tag{1.6}$$

$$\mu_i = \left(\frac{\partial F}{\partial N_i}\right)_{T,V,N_{j\neq i}} \tag{1.7}$$

Controlling these variables is equivalent to control the fundamental equation of the system, nevertheless from now on we will refer to equation 1.6, as equation of state, as it relates pressure (an intensive variable) with the rest of independent variables of the system.

1.1.1 Thermodynamic stability and phase transitions

Any part of a system which shows homogeneity in al its points with an average composition and the same intensive variables can be considered as a phase [19]. For this phase to be in thermodynamic equilibrium, it need to be maximizing the entropy or minimizing any of the thermodynamic potentials. Therefore, given the fundamental equation as $S = S(U,V,N_i)$ this would be expressed like:

$$dS = 0 \tag{1.8}$$

$$d^2S \leq 0 \tag{1.9}$$

And given any thermodynamic potential as a function of its independent variables, $B = B(x_i)$, the stability condition would read:

$$dB = 0 \tag{1.10}$$

$$d^2B \geq 0 \tag{1.11}$$

This conditions of equilibrium can hold for several phases in the same system at the same time. But this phases must be at the same temperature to avoid heat transfer and at the same pressure to avoid mechanic works. In the case of multicomponent systems the chemical potential should also be the same to avoid diffusions, arriving to the conditions in the case of C components and f phases:

$$\begin{aligned}
p^\alpha &= p^\beta = p^\gamma = \cdots = p^f \\
T^\alpha &= T^\beta = T^\gamma = \cdots = T^f \\
\mu_1^\alpha &= \mu_1^\beta = \mu_1^\gamma = \cdots = \mu_1^f \\
\mu_2^\alpha &= \mu_2^\beta = \mu_2^\gamma = \cdots = \mu_2^f \\
&\vdots \\
\mu_C^\alpha &= \mu_C^\beta = \mu_C^\gamma = \cdots = \mu_C^f
\end{aligned} \tag{1.12}$$

Giving us C(f-1) equations and 2+f(C-1) unknown variables, therefore the number of possible solutions reads:

$$L = 2 + f(C-1) - C(f-1) = 2 + C - f \tag{1.13}$$

Equation known as Gibbs Phases Rule, which gives us the number of phases that can coexist. For a monocomponent system the equilibrium of two phases arise in a line ($L = 2 + 1 - 2 = 1$), known as binodal , and the equilibrium of three phases in a point $(L = 0)$ known as triple point [19,20]. Not being possible the coexistence of more than three phases.

1.1.2 Statistical mechanics

This discipline is capable to relate the microscopic degrees of freedom of a system with its thermodynamic properties. A macroscopic system holding an Avogadroś number (N_A) of particles with r degrees of freedom each, leave us with a number of equations in the order of N_A, precisely describing the system, but in the end unsolvable in practice.

The physical state of a system with $r \cdot N_A$ degrees of freedom in the context of classical physics in a given instant will be characterized by its generalize coordinates q_i and their correspondent generalize momenta p_i. The mathematical space constituted by $\{q_i, p_i\}$ is called phase space. Thermodynamic variables like temperature or entropy explicitly do not depend on coordinates in this space, but thanks to the work of Maxwell, Gibbs and Boltzmann we will be able to relate both of them.

The state of a system can be represented as a point in the phase space and as we will see, averaging over a number of them we will find the thermodynamic magnitudes we are looking for. The set of points in the phase space corresponding to a macroscopic state are named Ensemble. If our system has a fixed volume, temperature and number of particles it is called Canonic Ensemble. In it we can define the classical partition function as [21–23]:

$$Q_N(V,T) = \frac{1}{N!}\Lambda^{-3N} Z_{N,rot} Z_N(V,T) \tag{1.14}$$

where $\Lambda = h(2\pi m \kappa_B T)^{-1/2}$ is the thermal De Broglie wave length,

$Z_{N,rot}$ the orientational partition function [23, 24] and $Z_N(V,T)$ the configuration integral:

$$Z_N(V,T) = \int exp\left[-\beta V_N(\mathbf{1},\ldots,\mathbf{N})\right] d\mathbf{1}\ldots d\mathbf{N} \tag{1.15}$$

where $V_N(\mathbf{1},\ldots,N)$ is the potential energy of the system depending on the position and orientation of al particles $d\mathbf{i} = d\mathbf{r}_i d\Omega_i$ with $\mathbf{r}_i$ the position vector of the i_{th} particle and Ω_i the set of angles defining their orientation

From the partition function we can calculate the Helmholtz free energy like:

$$F = -\kappa_B T \ln\left(\frac{\Lambda^{-3N}}{N!} Z_{N,rot} V^N\right) - \kappa_B T \ln \frac{Z_N(V,T)}{V^N} \tag{1.16}$$

Now this equation together with eqs. 1.5 to 1.7 allows us to finally calculate the pressure, entropy and chemical potentials.

To exploit this powerful machinery we rely on the ergodicity principle, telling us that for a system to be ergodic it is necessary that its evolution in time allows it to access any point of the phase space compatible with the macroscopic system in a finite time [25]. This could only be proven for hard spheres [22]. Nevertheless, in simulation this hypothesis is assumed unless proven the contrary.

In an ergodic system the time average over any thermodynamic magnitude is equivalent to the average over the ensemble compatible with the macroscopic state. During this time the system will describe a trajectory over the phase space responsible for the value of this magnitude $f = f(q_i, p_i)$ then the macroscopic observable measured will be [26]:

$$f_{obs} = \lim_{t_{obs}\to\infty} \langle f(q_i,p_i)\rangle_t = \lim_{t_{obs}\to\infty} \frac{1}{t_{obs}} \int_0^{t_{obs}} f(q_i,p_i)\, dt \tag{1.17}$$

In an ergodic system this limit would be the same as the average over the set of microscopic configurations

$$\lim_{t\to\infty}\langle f\rangle_t = \lim_{m\to\infty}\langle f\rangle_m \tag{1.18}$$

Where m is the number of points in the phase space compatible with the macroscopic system. This equation provides two paths for computer simulations to arrive to thermodynamic variables. On one hand simulate the time evolution of the system as the techniques of Molecular Dynamics (MD) do, and on the other hand, to reproduce compatible points of the phase space as the techniques of Monte Carlo type do (MC).

1.2 Simulation methods

Between the variety of simulation techniques available from the two main different approaches. Molecular Dynamics (MD) and its variants where particles trajectories are determined by numerically solving Newton's equations of motion, or Monte Carlo (MC) variants where the system explores the phase space randomly. The most suitable for our purposes among them were chosen and adjusted to meet the needs of each study. When it was needed to compute dynamic magnitudes over time, it was used a special type of MD known where the degrees of freedom of the solvent are not explicitly considered, Brownian Dynamics to reproduce the moves of colloids in suspension. In cases where the interest relied on equilibrium states, to achieve them Monte Carlo techniques were employed for faster exploring the phase space, in each case under the necessary ensemble for the variables involved. These techniques and some other computations are described below.

1.2.1 Spherocylinders as a model

To reduce computation time in molecular simulation a possible choice is to simplify the model employed. This is to fixate some degrees of freedom of our system, in a way that impacts as minimum as possible the observables we are trying to compute. When we assume a level of simplification that allows us to group several atoms into an indivisible particle of our model we refer to this as a coarse grain model. Currently many simulations use a conglomerate of beads to model different shapes of particles with interactions, in this thesis a coarse grain model [27] is used to simulate flat and elongated shapes with only one body per particle. The advantage of it is that instead of computing the interaction with every bead pertaining to every particle interaction, there is just need to compute the minimum distance between particles. The improvement of the calculations is increased as the aspect ratio becomes more extreme.

If we decide to model a system of particles without homogeneous shape, hence not using spheres, the next most simple models have $D_{\infty,h}$ symmetry, therefore are uniaxial objects. To obtain a spherocylinder rotating a two dimensional shape we need to use the geometric place at a distance $\sigma/2$ from a segment of length L (See figure 1.1). Using the direction of the segment as revolution axis we would obtain a prolate spherocylinder. However, using as revolution axis an imaginary coplanar line perpendicular to the segment placed in its centre we would obtain a oblate one. This shape is visually similar to the space occupied by electronic clouds, or at least fits it better (specially on the edges) than the commonly employed ellipsoids that appear in the Gay-Berne potential [28].

We decided to employ spherocylinders throughout the whole thesis for the reasons exposed above, with different prolate ($a_p > 1$) and oblate anisotropies ($a_o < 1$) as depicted in figure 1.1, where for the same aspect ratio $a_p = a_o^{-1}$,

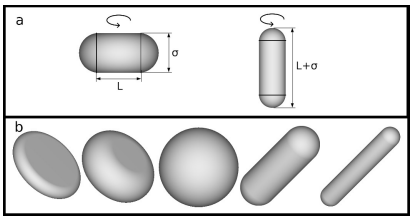

Figure 1.1: a) Schematic representation of an oblate (left) and prolate (right) solid of revolution. b) Examples of spherocylinders with anisotropies (from left to right) equal to 0.1, 0.5, 1, 5, and 10.

when defined as follows:

$$a_p = (L+\sigma)/\sigma \qquad ; \qquad a_o = \sigma/(L+\sigma) \tag{1.19}$$

Efficient algorithms are able to provide the minimum distance between two segments [29] or two disks [30], for the cases of prolate and oblate spherocylinders respectively, necessary to compute the potential energy for the different interaction models. This shapes allow to express the packing fraction as $\eta = \rho^* V_{sc}$ where, V_{sc} is the volume of the spherocylinder, and $\rho^* = N/(L+\sigma)^3$, being N the number of particles.

1.2.2 Monte Carlo

The Monte Carlo methods makes use of random number generator to generate system configurations compatible with the evolution of the system under study following a Markov chain. Trough this method our system will not follow a real route in the phase space, exploring it more efficiently, to later average the properties of interest from the explored configurations. This implies in fact an easier implementation than molecular dynamics, also allowing the use of hard

potentials inaccessible to MD. But it is neither suitable to study systems out of equilibrium (it would not satisfy equation 1.18), nor to calculate transport properties or other dynamical properties. Unless very novel techniques are applied in its implementation [31–33].

In essence, the MC method is based on the calculation of averages of thermodynamical properties over a set of points of the phase space, in the canonical ensemble this can be written as:

$$\langle f \rangle_m = \frac{\int f(\mathbf{1},\ldots,\mathbf{N})\, exp\,[-\beta V_N(\mathbf{1},\ldots,\mathbf{N})]\, d\mathbf{1}\ldots d\mathbf{N}}{\int exp\,[-\beta V_N(\mathbf{1},\ldots,\mathbf{N})]\, d\mathbf{1}\ldots d\mathbf{N}} \tag{1.20}$$

Where the denominator is the configurational partition functionZ_N (eq 1.15). We could randomly generate a big number of configurations but, nevertheless finite and substitute the integrals by sums [34]:

$$\langle f \rangle_m \simeq \frac{\sum_m f(m)\, exp\,[-\beta V_N(m)]}{\sum_m exp\,[-\beta V_N(m)]} \tag{1.21}$$

Where m goes from 1 to the total number of configurations N_c. This calculation would generate a very small Boltzmann factor, meaning that even when possible these configurations would be rather improbable and with little influence in the averages.

To perform this calculation efficiently the Monte Carlo method usually recurs to the Markov chain proposed by Metropolis *et al.* [35]. Assuming the probability to find the system in a point of the phase space with coordinates $(\mathbf{1},\mathbf{2},\cdots,\mathbf{N})$, in the canonical ensemble is given by the Boltzmann factor and the configurational partition function as:

$$P(\mathbf{1},\mathbf{2},\cdots,\mathbf{N}) = \frac{exp[-\beta V_N(\mathbf{1},\mathbf{2},\cdots,\mathbf{N})]}{Z_N} \tag{1.22}$$

If we generate random points of the phase space following this probability distribution function, the average of points generated in a differential volume

centred in $(\mathbf{1},\mathbf{2},\cdots,\mathbf{N})$. This will be $n_i = P(\mathbf{1},\mathbf{2},\cdots,\mathbf{N})\cdot N_c$ where N_c is the total number of generated points [36]. Now equation 1.21 derives into:

$$\langle f \rangle_m \simeq \frac{1}{N_c}\sum_{m=1}^{N_c} f(m)P(m) \tag{1.23}$$

To be able to follow the probability distribution, this method employs a Markov chain. Starting from a initial configuration, we build some other close to it in the phase space evaluating the probability to transition from one to other, defined in such a way that this probability distribution converges to the canonical probability distribution (equation 1.22). To achieve this it is necessary to fulfil the microscopic reversibility condition, which can be expressed mathematically like [36]:

$$P(i)\Pi_{i\to j} = P(j)\Pi_{j\to i} \tag{1.24}$$

Where $\Pi_{i\to j}$ is the probability to transition from i to j ans $P(i)$ is the probability to find the system in point i. This ecuation can be satisfied in many forms of the probability matrix $\Pi_{i\to j}$. The choice of Metropolis was:

$$\Pi_{i\to j} = \quad \frac{P(j)}{P(i)} = \exp\left[-\beta\left(V_N(j) - V_N(i)\right)\right] \quad if \quad P(j) \leq P(i)$$

$$\Pi_{i\to j} = \quad 1 \quad if \quad P(j) \geq P(i)$$

To make the system follow this Markov chain we pick a random particle from an initial configuration(i)and displace it moving the system into configuration(j). Then we evaluate $\Pi_{i\to j} = \exp\left(-\beta\Delta V_N\right)$ which is compared with a random number in the interval $[0,1]$. When this number is less than $\Pi_{i\to j}$ the configuration change is accepted and rejected in other case. This process is then repeated

wherever configuration the system is now on. In this way the system explores regions of the phase space which are compatible with the macroscopic state.

The implementation of this method extended from the NVT ensemble to the Isotension-Isothermal ensemble is presented in section 1.2.3.

1.2.3 Isotension-Isothermal ensemble

To be able to equilibrate states of solid phases it is mandatory that our simulation box adapts to the system to be sure that our equilibrium structure is not produced by applied stress. Or we might want to investigate the effect of some specific stress on the structure. The first to put this into practice were Parrinello and Rahman [37, 38], and apparently after their work, several authors independently developed similar Monte Carlo techniques to implement the Isotension-Isothermal ensemble. With the first publication usually atributed to Najafabadi [39]. In the latter approach it is only needed a transformation of the space of coordinates that allows to change the shape of the simulation box, using an adequate acceptance rule for the volume moves [36]. The transformation can be operated as follows:

$$\mathbf{r}_i = \mathbf{s}_i H \tag{1.25}$$

where H is a 3×3 matrix whose columns are the three vectors that define the edges of the simulation box, $\mathbf{r}_i$ are the coordinates in the real space and $\mathbf{s}_i$ are the coordinates in a cubic box of $1 \times 1 \times 1$. Therefore, the real volume of the system is the determinant of this matrix ($V = \det H$), and can be readily introduced in the acceptance rule, this observable has to be $\det H > 0$, otherwise we might fall into the absurd of a negative volume or into irreversible transformations ($\det H = 0$). During each volume move a random element of the matrix H is modified to efficiently explore the phase space of the system. To compute the acceptance

probability we use the function W defined as follows [40]:

$$W = \Delta U + P\Delta V - N\kappa_B T\Delta(\log V) \tag{1.26}$$

where U is the energy from the sum of the pair potentials, V the volume, N the number of particles, κ_B the Boltzmann constant and T the temperature. Then the volume move is accepted with probability P:

$$P = \quad 1 \quad if \quad W \leq 0$$

$$P = \quad \exp(-W/\kappa_B T) \quad if \quad W > 0$$

and rejected with probability $(1-P)$. In order to implement these transformations into a simulation code, we need to understand how every part of the code is related to the relative positions of the particles to avoid artefacts in our results specially when working with anisotropic particles. Any algorithm relying on the adjacency of particles, like the ones dealing with periodic boundary conditions or cell lists should use s_i to address particles meanwhile any other relying on real distances, like the computation of the minimum distance between particles should use r_i. In this implementation, the orientations of anisotropic particles are not affected by the deformation of the simulation box and will behave well controlled energy of the pair interactions as usual.

The classical Isobaric-Isothermal ensemble (NPT) implementation does not care about the shape of the simulation box and can be understood as a simplification of the isotension-isothermal ensemble, where only the diagonal elements of H matrix are varied. If we start the simulations in a orthogonal box we will keep its shape, and the elements H_{11}, H_{22} and H_{33} will be representing the sides of the box. Therefore, this shape transformation wont be needed any more and it would be enough to rescale the coordinates (for more details on this see reference [36]).

1.2.4 Brownian Dynamics of anisotropic particles

Brownian Dynamics (BD) simulation technique is employed to mimic the behaviour of suspensions of colloidal particles, whose size is significantly larger than that of the solvent molecules. Hence, the presence of the solvent is effectively incorporated by imposing a random drifting of the particles, whose trajectories are obtained by integrating the Langevin equation [41]. In BD simulations of non-spherical particles, the position, $\mathbf{r}_j$, and orientation, $\hat{\mathbf{u}}_j$, of a particle j over time t are calculated by the following set of equations [42]:

$$\begin{aligned}\mathbf{r}_j^{\parallel}(t+\Delta t) = \mathbf{r}_j^{\parallel}(t) + \frac{D_{s,\parallel}}{\kappa_B T}\mathbf{F}_j^{\parallel}(t)\Delta t + \\ +(2D_{s,\parallel}\Delta t)^{1/2} R^{\parallel}\hat{\mathbf{u}}(t)\end{aligned} \tag{1.27}$$

$$\begin{aligned}\mathbf{r}_j^{\perp}(t+\Delta t) = \mathbf{r}_j^{\perp}(t) + \frac{D_{s,\perp}}{\kappa_B T}\mathbf{F}_j^{\perp}(t)\Delta t + \\ +(2D_{s,\perp}\Delta t)^{1/2}(R_1^{\perp}\hat{\mathbf{v}}_{j,1}(t) + R_2^{\perp}\hat{\mathbf{v}}_{j,2}(t))\end{aligned} \tag{1.28}$$

$$\begin{aligned}\hat{\mathbf{u}}_j(t+\Delta t) = \hat{\mathbf{u}}_j(t) + \frac{D_{s,\vartheta}}{\kappa_B T}\mathbf{T}(t)\times\hat{\mathbf{u}}(t)\Delta t + \\ +(2D_{s,\vartheta}\Delta t)^{1/2}(R_1^{\vartheta}\hat{\mathbf{v}}_{j,1}(t) + R_2^{\vartheta}\hat{\mathbf{v}}_{j,2}(t))\end{aligned} \tag{1.29}$$

where $\mathbf{r}_j^{\parallel}$ and $\mathbf{r}_j^{\perp}$ are the projections of the position vector $\mathbf{r}_j$ on the direction parallel and perpendicular to $\hat{\mathbf{u}}_j$, respectively; $\mathbf{T}_j$ is the total torque acting over particle j [43]; $\mathbf{F}_j^{\parallel}$ and $\mathbf{F}_j^{\perp}$ are the components of the force parallel and perpendicular, respectively, to $\hat{\mathrm{u}}_j$; $R^{\parallel}$, $R_1^{\perp}$, $R_2^{\perp}$, R_1^{ϑ} and R_2^{ϑ} are independent Gaussian random numbers of variance 1 and zero mean; $\hat{\mathbf{v}}_{j,1}$ and $\hat{\mathbf{v}}_{j,2}$ are two random perpendicular unit vectors, being also perpendicular to vector $\hat{\mathbf{u}}_j$. The short time diffusion coefficients in the direction parallel and perpendicular to the molecular axis, and rotational difusion coefficient, $D_{s,\parallel}$, $D_{s,\perp}$ and $D_{s,\vartheta}$, have been

calculated for both prolate and oblate particles with the analytical expressions proposed by Shimizu for spheroids [44]:

$$
\begin{aligned}
D_{s,\perp} &= D_0 \frac{(2a^2-3b^2)S+2a}{16\pi(a^2-b^2)}b, \\
D_{s,\parallel} &= D_0 \frac{(2a^2-b^2)S-2a}{8\pi(a^2-b^2)}b, \\
D_{s,\vartheta} &= 3D_0 \frac{(2a^2-b^2)S-2a}{16\pi(a^4-b^4)}b,
\end{aligned}
\tag{1.30}
$$

In the above equations, $D_0 = \kappa_B T/\mu_s\sigma$, where k_B is the Boltzmann constant, T the absolute temperature, and μ_s the viscosity of the medium. S is a geometric parameter that for prolate particles reads [44]

$$
\begin{aligned}
\text{with} \quad S &= \frac{2}{(a^2-b^2)^{1/2}} \log \frac{a+(a^2-b^2)^{1/2}}{b}, \\
&(a=(L+\sigma)/2,\ b=\sigma/2)
\end{aligned}
\tag{1.31}
$$

and for oblate particles reads

$$
\begin{aligned}
\text{with} \quad S &= \frac{2}{(b^2-a^2)^{1/2}} \arctan \frac{(b^2-a^2)^{1/2}}{a}, \\
&(a=\sigma/2,\ b=L/2)
\end{aligned}
\tag{1.32}
$$

1.2.5 Cluster move

Simulations in the NPT ensemble can suffer from long equilibration times during compressions due to particle overlaps [45]. To overcome this and inspired by the work of Ashton and collaborators [46], their cluster move algorithm (see pseudo-code in alg. 1) has been implemented to explore low density regions of the phase diagrams presented in this thesis.

There are systems where aggregates can not compress internally, therefore during a volume move the simulation box can not shrink unless every cluster moves as a whole. But instead of rescaling coordinates, in this move a point reflection about a random pivot point is performed, to better sample the phase space. In order to easily obey detailed balance, any move producing a change in energy is considered an overlap obtaining a rejection free move. Even so every system investigated at densities below 1 particle per unit volume (given a length unit equal to the biggest dimension of the particles involved) experienced a faster equilibration. At higher densities this algorithm becomes useless when overlaps drives it to mirror the configuration of every particle of the system what is pointless under periodic boundary conditions.

Algorithm 1: Pivot point cluster move

```
1: Select random particle p_i and pivot point
2: Label p_i and its cluster as "To move"
3: while "To move" stack is not empty do
4:     Remove first particle p_i from the "To move" stack
5:     Label it as "Moved" and point reflect it
6:     if p_i overlaps with UNLABELED particles then
7:         Label those overlapped particles and their clusters as "To move"
8:     end if
9: end while
```

1.3 Distribution Functions and order parameters

The relative position and orientation of the constituents of a substance are key parameters to characterize its state. In this thesis, all studies are performed over monocomponent systems, this denies us the possibility to define these magnitudes from the relative positions and orientations of the particles of different

components, what would be very useful given the case. Although thermodynamic variables such as density, entropy or enthalpy undergo abrupt changes in phase transitions, the internal order is characteristic of each mesophase. Therefore, the ability to quantify it makes order parameters and distribution functions indispensable tools in this field.

Since we are dealing with anisotropic particles and forcefields, it will be useful to track structural properties. We start by defining the Nematic Order Parameter S_2 as:

$$S_2 = \langle \frac{1}{N} \sum_{1}^{N} P_2(\hat{\mathbf{u}}_i \cdot \hat{\mathbf{n}}) \rangle \tag{1.33}$$

Where P_2 is the second order Legendre polynomial, N the number of particles, $\langle \cdots \rangle$ denotes the statistical average over configurations and $\hat{\mathbf{u}}_i$ and $\hat{\mathbf{n}}$ are the unitary vectors of the orientations of the particles and the nematic director respectively. The nematic director is usually dominated by an external field but can also arise from an orientational symmetry break during a phase transition. In those cases the vector is unknown beforehand and it is usually calculated from the Order Parameter Tensor $\mathbf{Q}$:

$$Q_{\alpha\beta} = \frac{1}{2N} \langle \sum_{1}^{N} (3\hat{\mathbf{u}}_{i\alpha} \cdot \hat{\mathbf{u}}_{i\beta} - \delta_{\alpha\beta}) \rangle \tag{1.34}$$

Where $\delta_{\alpha\beta}$ is the Kronecker delta and α y β indicate the vector components. This tensor can be diagonalized being S_2 its biggest eigenvalue and $\hat{\mathbf{n}}$ the correspondent eigenvector. S_2 Can vary from values close to 0 in a isotropic situation to values close to 1 when all particles are almost parallel oriented.

However, to investigate structural properties, the distribution functions are a more powerful tool, since with it we also obtain detailed information about the orientational order or any other parameter which can be computed as a function

of the distance between particles. We will use a set of them starting from the radial distribution function $g(r)$, which can give us the average amount of particles between r and $r+dr$ as, $4\pi r^2 \rho g(r) dr$. To define other distributions of interest we have to particularize it depending on the region of the space where we are interested to know the probability of finding a particle. A common feature of these functions is its asymptotic tendency to one at long distances (in the thermodynamic limit). To our purpose we can summarize the distributions of interest with the formula:

$$g_\zeta(r_\zeta) = \frac{N_H(\zeta)}{\rho N N_c V(\zeta)} \tag{1.35}$$

This function when multiplied by the density, remains being the average over particles and configurations found in the volume $V(\zeta)$ surrounding position r_ζ, from a particle located at the coordinates' origin. Where N_H is the total number of particles inside the volume $V(\zeta)$, N the total number of particles and N_c the number of sampled configurations and ρ the density of the system. In table 1.1 are indicated the definitions of $V(\zeta)$ and r_ζ correspondent to each particular example of distribution function used in this thesis, being each row a specific choice on how to implement equation 1.35, among many possibilities.

Each one of these functions can be used to measure a different level of partial order or the system structure. The radial distribution functions can easily tell us if we are leaving the isotropic phase starting to display any sort of peaks, when we find them at small values of r/σ it is a sign some level of order in the first neighbours. In the cases where we are studying a system with layers the maximums of the parallel distribution function $g_\parallel(r_\parallel)$ mark their location. If we are interested in the average order of the layers we can use the perpendicular distribution function $g_\perp(r_\perp)$, but if we want to focus on the inner order of the layer where the origin of coordinates is located, we should use the ground

	r_ζ	$V(\zeta)$
$g(r)$	$r = \|\mathbf{r}\|$	$\frac{4\pi}{3}\left((r+\Delta r/2)^3-(r-\Delta r/2)\right)$
$g_\parallel(r_\parallel)$	$r_\parallel = \mathbf{r}\cdot\mathbf{n}$	$\pi\left(R^2\Delta r_\parallel - 1/3((r_\parallel+\Delta r_\parallel/2)^3-(r_\parallel-\Delta r_\parallel/2)^3)\right)$
$g_\perp(r_\perp)$	$r_\perp = \|\mathbf{r}-(\mathbf{r}\cdot\mathbf{n})\mathbf{n}\|$	$4\pi/3\left((R^2-(r_\perp+\Delta r_\perp)^2)^{\frac{3}{2}}-(R^2-r_\perp^2)^{\frac{3}{2}}\right)$
$g_\perp^0(r_\perp^0)$	$r_\perp = \|\mathbf{r}-(\mathbf{r}\cdot\mathbf{n})\mathbf{n}\|$ being $\|\mathbf{r}\cdot\mathbf{n}\| < L$	$\pi((r_\perp+\Delta r_\perp)^2 - r_\perp^3)L$

Table 1.1: Terms employed to calculate each distribution function. Where R is half the length of the simulation box and L is the thickness of the layer. Δr_ζ is the width of the volume element V_ζ surrounding position r_ζ.

perpendicular distribution function $g_\perp^0(r_\perp^0)$

For our purpose is useful to define one more distribution function $g_2(r)$, which averages the value of the second Legendre polynomial obtained for particles at each distance, formulated as follows:

$$g_2(r) = \langle P_2(\mathbf{u}_i \cdot \mathbf{u}_j)\rangle \tag{1.36}$$

This coincides with the spherical harmonic Y_{20}, frequently employed for the study of polyatomic fluids.

1.4 Dynamic observables

1.4.1 Mean Squared Displacement

The Mean Squared Displacement (MSD) computes, as its name indicates the displacement of particles from an initial position over time. Therefore, quantifies

particle diffusions at different times and is calculated as follows:

$$\left\langle \Delta r^2(t) \right\rangle = \left\langle \frac{1}{N} \sum_{j=1}^{N} (\mathbf{r}_j(t) - \mathbf{r}_j(0))^2 \right\rangle, \tag{1.37}$$

where the brackets $\langle ... \rangle$ denote ensemble average. We have also computed the MSD parallel, $\langle \Delta r_{\parallel}^2(t) \rangle$, and perpendicular, $\langle \Delta r_{\perp}^2(t) \rangle$, to the nematic director $\hat{\mathbf{n}}$. This vector has been calculated diagonalizing a symmetric traceless tensor incorporating the orientation vectors of all the particles [47]. The MSDs at long time scales are used to estimate the long time diffusion coefficients as follows for the perpendicular, parallel and total respectively:

$$\begin{aligned} D_{l,\perp} &= \lim_{t\to\infty} \frac{\langle \Delta r_{\perp}^2(t) \rangle}{4t}, \\ D_{l,\parallel} &= \lim_{t\to\infty} \frac{\langle \Delta r_{\parallel}^2(t) \rangle}{2t}, \\ D_l &= \lim_{t\to\infty} \frac{\langle \Delta r^2(t) \rangle}{6t}, \end{aligned} \tag{1.38}$$

We stress that these diffusion coefficients are different from those calculated in Eq. 1.30, which only take into account the effect of the solvent, but disregard the interaction with other colloidal particles.

We have also estimated the rotational diffusivity in the isotropic and nematic phases. To this end, we have calculated the orientational time-correlation functions [48]

$$C_1(t) = < P_1[u_i(t) \cdot u_i(0)] > \tag{1.39}$$

The typical decay time, τ_1, of this function could be estimated as

$$\tau_1 = \int_0^{\infty} C_1(t) dt \tag{1.40}$$

From this decay time, it is possible to define a rotational diffusion coefficient as $D_{rot} = 1/2\tau_1$ [48].

1.4.2 Self-intermediate scattering function

The Self-intermediate scattering function (s-ISF) gives a measure of the structural relaxation decay of density fluctuations and reads:

$$F_s(\mathbf{q},t) = \frac{1}{N}\left\langle \sum_{j=1}^{N} \exp[i\mathbf{q}\cdot(\mathbf{r}_j(t+t_0) - \mathbf{r}_j(t_0))] \right\rangle, \tag{1.41}$$

where $\mathbf{q}$ is the wave vector calculated at relevant peaks of the static structure factor and $\mathbf{r}_j(t)$ is the particle position at time t.

1.4.3 Four-point susceptibility function

To explore the occurrence of collective motion, we can compute the four-point susceptibility function, $\chi_4(q,t)$, which measures the fluctuations of the s-ISF and provides information on the size and time evolution of the transient clusters formed in the fluid [49–51]. This function determines the eventual occurrence of collective motion by mapping the dynamics in two different spatial domains at two different times, hence its four-point nature. It is calculated as:

$$\chi_4(q,t) = N\left[\left\langle f_s^2(\mathbf{q},t)\right\rangle - F_s^2(\mathbf{q},t)\right] \tag{1.42}$$

where $f_s(\mathbf{q},t) = 1/N\sum_{j=1}^{N}\cos(\mathbf{q}[(\mathbf{r}_j(t+t_0) - \mathbf{r}_j(t_0))]$ is the real part of the instantaneous value of the s-ISF.

Chapter 2

Dynamics of particles with *opposite* geometries

The thermodynamics of anisotropic particles have been extensively studied in the past. Phase diagrams and equilibrium structures obtained in systems of prolate [52,53] and oblate [54,55] purely repulsive particles have been well characterized and also a number of potentials, such as the Gay-Berne [28], Kihara [56] or the more recent Gay-Berne-Kihara potential [57,58] have been investigated. In this chapter a specific framework is set to compare, in a meaningful way, oblate and prolate geometries in the context of ordered fluids.

As described in section 1, this thesis is focused on systems with a significant degree of orientational and/or positional order, like liquid crystals (LCs). In this kind of systems structural properties are the key to the plethora of applications and molecular simulation has been crucial to understand and characterize liquid crystalline materials [59,60], but not so many studies have been dedicated to the study of their dynamical properties, especially for oblate particles.

Dynamical properties are equally important and contribute to determine the performance of a material. Laschat *et al.* showed that discotic mesogens are not useful as switching units in LC displays due to the fact that their LCs typically have larger viscosity than that measured in LCs of rod-like mesogens [61]. This gives us a hint on the impact of particle anisotropy on the transport properties and on the consequent design of devices for the above-mentioned applications.

If we keep up the comparison of particles with opposite geometries we could vary the aspect ratios of each to obtain the same values in terms of anisotropy, volume, or diffusion coefficients. The scope of the work in this chapter is to compare the relative ability of prolate and oblate particles of diffusing in their nematic phases. To this end, we impose the same values of the infinite-dilution translational or rotational diffusion coefficients for both prolate and oblate particles (See equation 1.30). This choice represents an important change with respect to past studies that assumed the same particle volume or aspect ratio [62, 63].

Very early theoretical studies predicted an anisotropy in the diffusion of the particles in nematic fluids [62, 63], later corroborated by simulations [64, 65]. Specifically, it was concluded that, in the nematic phase of prolate particles the diffusion is faster in the direction parallel to the nematic director. In particular, the long-time diffusion coefficient parallel to the nematic director, $D_{\parallel}$, is larger than the diffusion coefficient perpendicular to the nematic director, $D_{\perp}$. The opposite tendency is observed in nematic phases of oblate particles. Nevertheless, in positionally order smectic and columnar LCs, the layer-to-layer and column-to-column diffusion results to be significantly reduced and becomes slower than the in-layer or in-column diffusion [66–71].

For this system we expect that the particle mean-square displacement (MSD) is a linear function of the time t, whereas the particle displacements are Gaus-

sian distributed. The linear behaviour of the MSD with time is generally referred to as Fickian diffusion, after Adolf Fick, who derived the laws of diffusion in 1855 [72]. To perform this study we used Brownian Dynamics (BD) simulations (See section 1.2.4), with them we study the dynamics of nematic colloidal LCs of disk-like and rod-like particles and show that a typical Fickean diffusion is observed at short and long time scales, meanwhile at medium time scales this appears to be yet Fickean but not Gaussian (FNG). This feature is very attractive to investigate in nematic LCs where at different time scales, this can be addressed over two independent directions at distinctive particles anisotropies, what will occupay the first part of this study. In Nematic systems it is observed that they can induce non-Fickian subdiffusion or superdiffusion of host particles, generally referred to as anomalous diffusion [73]. In addition, the relatively moderate packing fractions of nematics, as compared to smectic or columnar LC phases, allow to more easily achieve the asymptotic limit of long time scales and distinguish it from the non-Gaussian signature of the caging effect at shorter times. Previous works observed non-Gaussian dynamics in smectic [67, 69, 71] and columnar [70, 74] LCs, where the diffusion perpendicular, respectively, to the layers and columns is especially slow and determining the onset of the long time diffusive regime not always straightforward.

The non-Gaussian diffusion observed in heterogeneous systems has been investigated by stochastic models assuming random diffusivities, such as the generalised grey Brownian motion [75, 76] and the diffusing diffusivities model [76–78]. The observation of FNG diffusion in very dilute colloidal suspensions of hard-sphere PMMA particles, which would be expected to follow a canonical Brownian dynamics, has been interpreted as a convincing argument supporting its ubiquitous nature [79]. However, the FNG signature in especially complex systems, such as colloidal liquid crystals (LCs), where an anisotropic diffusion

is observed, is still to be explored.

To close this study, three case scenarios are defined, to complete the comparison of this *opposite* geometries observing the differences and coincidences of the difusion in equivalent fluids of prolate and oblate spherocylinders. The cases of particles with (*i*) equal aspect ratio, (*ii*) equal infinite-dilution translational diffusion coefficients, and (*iii*) equal infinite-dilution rotational diffusion coefficients. This infinite-dilution diffusion coefficients, defined in section 1.4.1, are the same as those calculated in concentrated suspensions at very short time scales, when the particles are still rattling around their original position and have not yet interacted with their nearest neighbors.

2.1 Model and methodology

For this study as well as for the whole thesis we have used spherocylindrical particles as described in section 1.2.1 with the desired anisotropies. Since we are comparing the relative ability of oblate and prolate spherocylinders to diffuse in a nematic LC phase, one obvious choice would be to impose the same particle aspect ratio for the two geometries. Nevertheless, this choice, which allows one to consistently assess the phase behaviour of particles of different anisotropies, would not reproduce the same conditions of mobility at very short timescales or in extremely dilute suspensions. However, since the aim of the second part of this chapter is to have an insight into the effect of anisotropy on the long-time diffusion in structured fluids, we also equate the isotropic infinite-dilution translational, $D^s = (2D^s_\perp + D^s_\parallel)/3$, or rotational, D^s_ϑ, diffusion coefficients of oblate and prolate particles. To make this comparison we have chosen the anisotropies $a_p = 27$ and $a_o = 0.1$ for the case of translational equivalence, and $a_p = 15.6$ and $a_o = 0.1$ for the case of rotational equivalence. To fully clarify the effect of this choice, we have benchmarked our result with the case of identical shape

anisotropy, where $a_p = 1/a_o = 15.6$ employed in the first part of the study.

To describe the inter-particle interactions, we have used the Soft Repulsive Spherocylinder (SRS) potential, which is obtained by truncating and shifting the Kihara potential [56] and was used in the past to model prolate [80–82], and oblate mesogens [58]. The SRS potential reads

$$U_{SRS} = \begin{cases} 4\varepsilon \left[\left(\frac{\sigma}{d_m} \right)^{12} - \left(\frac{\sigma}{d_m} \right)^{6} + \frac{1}{4} \right] & \frac{\sigma}{d_m} \leq \sqrt[6]{2} \\ 0 & \frac{\sigma}{d_m} > \sqrt[6]{2} \end{cases} \tag{2.1}$$

In the above equation, ε is the unit of energy, while d_m is the minimum distance between the central cores of the particles, being a segment of length L for prolate particles, and a disk of diameter L for oblate particles. Efficient algorithms to calculate the minimum distance have been published for both particle geometries [43, 83]. As mentioned before, σ represents the diameter of prolate particles as well as the thickness of oblate particles.

Our system's length unit is σ, while the time unit is $\tau = \sigma^3 \mu_s / k_B T$, where μ_s is the solvent viscosity.

To simulate the Brownian motion of the particles, we have carried out Brownian Dynamics (BD) simulations as described in section 1.2.4. Using cubic boxes containing $N = 1344$ rods or 1500 disks. The time step has been set in the range $10^{-4} < t/\tau < 2 \cdot 10^{-3}$.

For each of these three possible scenarios, we have started from an initial configuration of N perfectly parallel particles randomly distributed in a cubic box, with $N = 1260 - 2232$ at the desired packing fraction $\eta = \rho v_m$, being ρ the numeric density of particles and v_m the volume of the particles [84]. To equilibrate the system, we have run BD simulations of about $t = 2000\tau$ for prolate and $t = 20000\tau$ for oblate particles, where $\tau = \sigma^2/D_0$ is the time unit. The time step was fixed to $\Delta t = 10^{-4}\tau$ for prolate and $10^{-5}\tau$ for oblate particles, while

the temperature is $T^* = k_B T/\varepsilon = 1.465$ for both geometries. At this temperature the phase behavior of soft spherocylinders resembles that of a fluid of hard spherocylinders [80,81]. The equilibration of the system has been monitored by checking the evolution of total energy and nematic order parameters. After equilibration, an additional BD simulation was carried out to compute a number of dynamical observables described in chapter 1: (*i*) the mean square displacement (MSD), (*ii*) the self part of the intermediate scattering function (s-ISF), and (*iii*) the four point susceptibility $\chi_4(q,t)$.

Besides the already mentioned, the most relevant observables in this work are the parallel, perpendicular and total self-van Hove functions, which are calculated, respectively, as

$$G_{s,1}(r_\parallel,t) = \frac{1}{N}\left\langle \sum_{j=1}^{N} \delta(r_\parallel - |\mathbf{r}_{\parallel,j}(t) - \mathbf{r}_{\parallel,j}(0)| \right\rangle \tag{2.2}$$

$$G_{s,2}(r_\perp,t) = \frac{1}{N}\left\langle \sum_{j=1}^{N} \delta(r_\perp - |\mathbf{r}_{\perp,j}(t) - \mathbf{r}_{\perp,j}(0)| \right\rangle \tag{2.3}$$

$$G_{s,3}(r,t) = \frac{1}{N}\left\langle \sum_{j=1}^{N} \delta(r - |\mathbf{r}_{j}(t) - \mathbf{r}_{j}(0)| \right\rangle \tag{2.4}$$

where the symbol δ is the Dirac delta, $r_{||}$ and $r_\perp$ are, respectively, the projections of the displacement parallel and perpendicular to the nematic director $\hat{\mathbf{n}}$, and the angular brackets denote ensemble average over all the particles and at least 100 independent phase space trajectories starting off at regular time intervals within the same simulation run. The director $\hat{\mathbf{n}}$ is calculated with the standard procedure of diagonalization of the traceless tensor incorporating the particles' orientation

vectors [47]. The functions in Eqs. 2.2, 2.3 and 2.4 should be normalised as follows: $\int_0^\infty G_{s,1} dr_\parallel = \int_0^\infty 2\pi r_\perp G_{s,2} dr_\perp = \int_0^\infty 4\pi r^2 G_{s,3} dr = 1$. Finally, to assess the Fickian diffusion at long time scales, we have calculated the MSD, including that in the direction parallel and perpendicular to $\hat{\mathbf{n}}$. Parallel, perpendicular and total MSDs are defined in section 1.4.1.

2.2 Fickean diffusion and its gaussianity in nematic liquid crystals

Before introducing the details of our theoretical and computer simulation results, it is useful to recall the three main time regimes of diffusion in a colloidal suspension. At short time scales, particles diffuse through the solvent and dissipate their thermal energy as a result of the collisions with the solvent molecules. This regime is diffusive (or Fickian) and the MSD is a linear function of time, or $\langle \Delta r^2 \rangle \propto t$. In particular, $\langle \Delta r^2 \rangle = 2dD_s t$, with d the dimensionality of the move and D_s the translational diffusion coefficient of an isolated particle in a medium. At intermediate time scales, the diffusion of individual particles is slowed down by a sort of temporary cage formed by other particles [66]. The duration of this caging effect is mainly determined by the system packing and inter-particle interactions. Finally, at long time scales, the diffusion is controlled by the inter-particle collisions and the Fickian regime is recovered. In this case, $\langle \Delta r^2 \rangle = 2dD_l t$, with D_l the long-time translational diffusion coefficient, being in general smaller than its infinite-dilution counterpart [85].

At each of this time scales, the distribution of the particle displacements can be measured by the self-part of the van Hove correlation function, $G_{s,d}(r,t) = 1/N \left\langle \sum_{i=1}^{N} \delta(r - |\mathbf{r}_i(t) - \mathbf{r}_i(0)|) \right\rangle$, where N is the total number of particles, δ the Dirac-delta, and $\langle ... \rangle$ denotes ensemble average over different trajectories. If the

displacements are Gaussian distributed, then $G_{s,d}(r,t)$ is a Gaussian function of r at all times:

$$G_{s,d}(r,t) = (4\pi D_t t)^{-d/2} \exp\left(-\frac{r^2}{4D_t t}\right), \tag{2.5}$$

where the subindex t indicates a generic dependence on time of the diffusion coefficient, such that $D_t = D_s$ and $D_t = D_l$ at short and long time scales, respectively. The space variable r refers to the longitudinal or radial direction in cylindrical coordinates if $d = 1$ or $d = 2$, respectively, whereas it refers to the radial coordinate in spherical coordinates if $d = 3$. The difficulty to determine the time regimes in which a Gaussian diffusion actually holds and perform measurements at very large length and long time scales, a limit where the non-Gaussian character of Fickian diffusion is especially challenging to be proven [86], has challenged the general applicability of Eq. 2.5 to complex fluids [87].

In Fig.2.1, we report the parallel and perpendicular components of the MSD for oblate and prolate particles with shape anisotropy $a_p = a_o^{-1} = 15.6$ in nematic LCs with packing fraction $\eta = 0.35$. In it we can distinguish the three mentioned timescales. At very short time scales, with $t/\tau < 0.5$, prolate particles diffuse faster in the direction perpendicular to $\hat{\mathbf{n}}$ and $\langle \Delta r_\perp^2(t) \rangle > \langle \Delta r_\parallel^2(t) \rangle$, which is coherent with the short time (or infinite-dilution) diffusion coefficients calculated from Eq. 1.30. At intermediate times, the perpendicular mobility becomes slower than the parallel mobility and an inversion in the trend observed at shorter times is observed. In particular, $\langle \Delta r_\perp^2(t) \rangle < \langle \Delta r_\parallel^2(t) \rangle$ at $t/\tau > 1$.

It is then possible to observe an intermediate regime where the slope of the perpendicular component of the MSD decreases significantly. Although $\langle \Delta r_\perp^2(t) \rangle$ does not reach a clear plateau as previously observed in glasses [88]

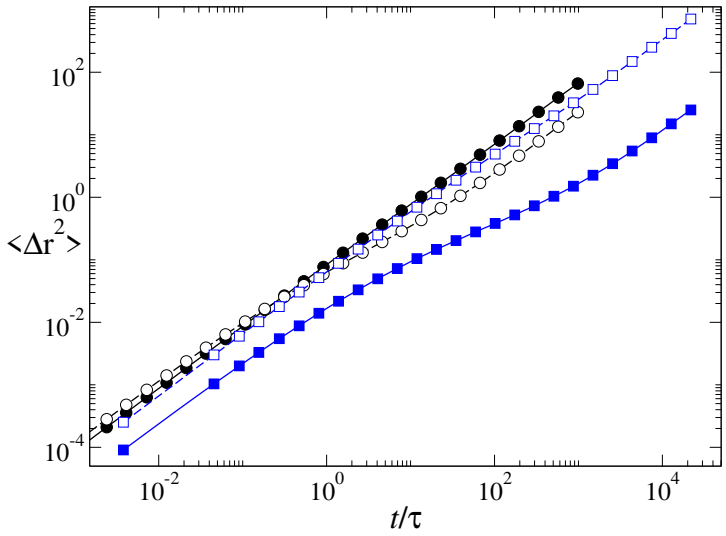

Figure 2.1: Parallel (solid lines and symbols) and perpendicular (dashed lines and open symbols) components of the MSD of prolate (black lines and circles) and oblate (blue lines and squares) particles with shape anisotropy $a_p = a_o^{-1} = 15.6$ in nematic liquid crystals with packing fraction $\eta = 0.35$.

or smectic phases [67–69], the transport of prolate particles in this direction shows a sub-diffusive regime, indicating the time and length scales over which particle start to collide with other particles in the direction perpendicular to $\hat{\mathbf{n}}$. At long times, this component shows a diffusive regime, characterised by the long-time diffusion coefficient obtained from the slope of $\langle \Delta r_\perp^2(t) \rangle$. By contrast, the parallel component of the MSD shows a smoother behavior, with an almost insignificant variation of the slope at intermediate times. Consequently, at long times the diffusion of prolate particles is mainly in the direction parallel to the nematic director, being the main contribution to the total MSD (not shown here). In summary, the diffusion of prolate particles in nematic LCs is clearly anisotropic with a fast and slow component in the direction, respectively,

parallel and perpendicular to $\hat{\mathbf{n}}$. The behavior of oblate particles with identical aspect ratio is characterised by opposite tendencies. Again, a clear anisotropy in the particle diffusion is observed. Nevertheless, the fast component is the one perpendicular to $\hat{\mathbf{n}}$, while the slow component, which exhibits a sub-diffusive regime at intermediate times, is parallel to it.

We detect a non-Fickian (sub-diffusive) regime at intermediate time scales. But our results agree very well with previous works [42, 64, 65] and confirm the Fickian character of the long-time isotropic diffusion, with D_l, and of the diffusion parallel and perpendicular to the nematic director $\hat{\mathbf{n}}$, with $D_{l,\parallel}$ and $D_{l,\perp}$, calculated as showed in equation (1.38).

In the light of these preliminary considerations, we now consider whether the particle displacements as well as their parallel and perpendicular projections to $\hat{\mathbf{n}}$ are Gaussian distributed. To this end, we calculate the parallel, $G_{s,1}(r_\parallel,t)$, perpendicular, $G_{s,2}(r_\perp,t)$, and total, $G_{s,3}(r,t)$, self-van Hove correlation functions, which are shown in Figs. 2.2 and 2.3) for rods and disks, respectively, at short (left frames), intermediate (middle frames), and long (right frames) time scales. In the same figures, we fit our simulation results with the Gaussian approximations calculated from Eq. 2.5, where D_t is a fitting parameter.

We observe that the Gaussian approximation to $G_{s,1}(r_\parallel,t)$ and $G_{s,2}(r_\perp,t)$ is very good at both short and long time scales, while, at intermediate times, where the diffusion is however not Fickian, moderate discrepancies are detected. We then conclude that, at least in the direction of $\hat{\mathbf{n}}$ and perpendicularly to it, prolate and oblate colloidal particles exhibit Fickian and Gaussian diffusion at short and long times. A more detailed analysis deserves the total self-van Hove function, $G_{s,3}(r,t)$, which clearly appears underestimated by the Gaussian fit at intermediate and long time scales, and less significantly also at short times (circles and black lines in Figs. 2.2 and 2.3). While at intermediate times the

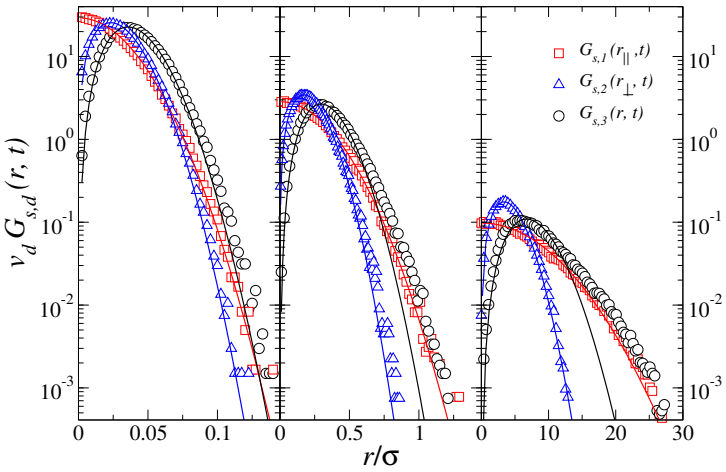

Figure 2.2: Parallel (□), perpendicular (△) and total (○) self-van Hove correlation functions for a nematic LC of prolate particles at times $t/\tau = 10^{-2}$ (left frame), $t/\tau = 1$ (middle frame) and $t/\tau = 10^3$ (right frame). Results are normalised by $v_d = 1$, $2\pi r_\perp$ or $4\pi r^2$ for $d = 1$, 2 or 3, respectively. Symbols are simulation results, while solid lines are Gaussian approximations as given in Eq. 2.5, with D_t fitting parameter.

diffusion is not Fickian and a non-Gaussian behaviour is not astounding, at short and long times one would conclude that prolate and oblate particles follow an FNG diffusion. Nevertheless, we notice that the Gaussian approximation in Eq. 2.5 results from the integration of the Langevin equation under the assumption of a spatial isotropy, where $D_{s,\parallel} = D_{s,\perp}$ and $D_{l,\parallel} = D_{l,\perp}$ [85]. This assumption does not hold in a nematic LC and, more generally, in any complex fluid with anisotropic morphology.

Therefore, we propose an ellipsoidal, rather than spherical, Gaussian approximation of $G_{s,3}(r,t)$, where the displacements in the direction parallel and perpendicular to $\hat{\mathbf{n}}$ are still assumed to be Gaussian distributed, but independent

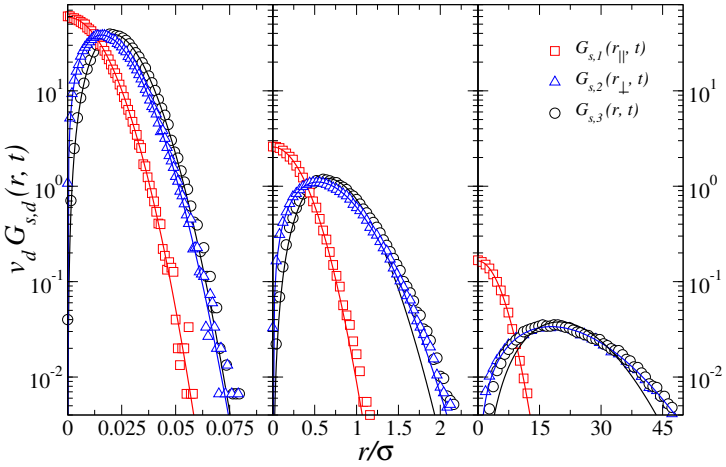

Figure 2.3: Parallel (□), perpendicular (△) and total (○) self-van Hove correlation functions for a nematic LC of oblate particles at times $t/\tau = 10^{-2}$ (left frame), $t/\tau = 10.8$ (middle frame) and $t/\tau = 2\times 10^4$ (right frame). Results are normalised by $v_d = 1$, $2\pi r_\perp$ or $4\pi r^2$ for $d = 1$, 2 or 3, respectively. Symbols are simulation results, while solid lines are Gaussian approximations as given in Eq. 2.5, with D_t fitting parameter.

of each other [89]. The new form of the total self-van Hove correlation function is determined by combining the displacements' distributions along the parallel and perpendicular directions to $\hat{\mathbf{n}}$ and reads

$$G_s(r_\parallel, r_\perp, t) = G_{s,1}(r_\parallel, t)\; G_{s,2}(r_\perp, t) = \frac{1}{\left((4\pi t)^3 D_{t,\perp}^2 D_{t,\parallel}\right)^{1/2}} \exp\left(-\frac{r_\parallel^2}{4D_{t,\parallel}t} - \frac{r_\perp^2}{4D_{t,\perp}t}\right) \tag{2.6}$$

where $G_{s,1}(r_\parallel, t)$ and $G_{s,2}(r_\perp, t)$ have been obtained by substituting, respectively,

$d = 1$ and $d = 2$ in Eq. 2.5. The probability to find a particle at distance $r = (r_\perp^2 + r_\parallel^2)^{1/2}$ from its original position at $t = 0$, is obtained by integrating Eq. 2.6 over a spherical surface Σ of radius r:

$$G'_{s,3}(r,t) = \frac{\int_\Sigma d\Sigma\, G_s(r_\parallel, r_\perp, t)}{\int_\Sigma d\Sigma}, \tag{2.7}$$

The solution of the above integral can either take the form

$$G'_{s,3}(r,t) = \frac{\Omega}{(4\pi t)^{3/2}} \exp\left(-\frac{r^2 t^{-1}}{4D_{t,\parallel}}\right) \frac{F(r\Delta_p^{1/2})}{r\Delta_p^{1/2}} \tag{2.8}$$

or equivalently

$$G'_{s,3}(r,t) = \frac{\Omega\sqrt{\pi}}{2(4\pi t)^{3/2}} \exp\left(-\frac{r^2 t^{-1}}{4D_{t,\perp}}\right) \frac{\mathrm{erf}(r\Delta_o^{1/2})}{r\Delta_o^{1/2}}, \tag{2.9}$$

where $F(...)$ is the Dawson's integral, erf(...) the error function, $\Omega = 1/(D_{t,\perp}^2 D_{t,\parallel})^{1/2}$, and $\Delta_p = -\Delta_o = 1/(4D_{t,\perp}t) - 1/(4D_{t,\parallel}t)$. Eqs. 2.8 and 2.9 are mathematically identical, being the former more suitable for prolate geometries, where $D_{t,\parallel} > D_{t,\perp}$, and the latter for oblate geometries, where $D_{t,\parallel} < D_{t,\perp}$.

The total self-van Hove functions calculated from Eqs. 2.8 and 2.9 are shown as solid lines in Fig.2.4, along with our simulation results. For comparison, we also show the Gaussian approximation of $G_{s,3}(r,t)$ as obtained from Eq. 2.5 (dashed lines). The agreement between simulations and theoretical predictions is

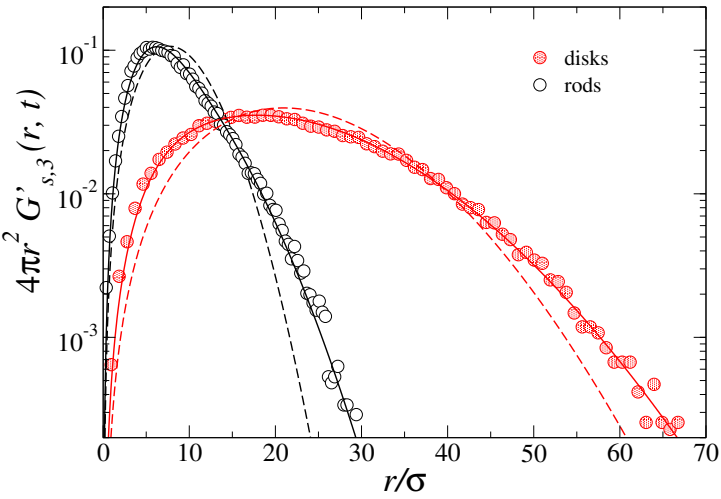

Figure 2.4: Total self-van Hove correlation functions for a nematic LC phase of rod-like and disk-like particles at $t/\tau = 10^3$ and 2×10^4, respectively. Symbols are simulation results, dashed lines are Gaussian distributions obtained from Eq. 2.5, and black solid lines are Gaussian distributions obtained with Eq. 2.8 (rods) and 2.9 (disks).

excellent, confirming the Gaussian nature of the Fickian diffusion at long times and thus discarding the occurrence of an FNG diffusion for the two particle geometries. We stress that the dashed and solid curves in Fig.2.4 are not fits, as the diffusion coefficients, $D_{l,\parallel}$ and $D_{l,\perp}$, at long times have been obtained from the corresponding MSDs. The theoretical predictions of $G'_{s,1}(r_\perp,t)$ and $G'_{s,2}(r_\parallel,t)$ obtained from Eq. 2.5 with the instantaneous values of $D_{l,\parallel}$ and $D_{l,\perp}$ from the MSDs, are also in excellent agreement with the simulation results and are shown in Figs. 2.5 and 2.6 for prolate and oblate spherocylinders, respectively.

The non-Gaussian character of $G_{s,d}(r,t)$ can also be assessed by expanding this function in a series of Hermite polynomials, whose first term incorporates

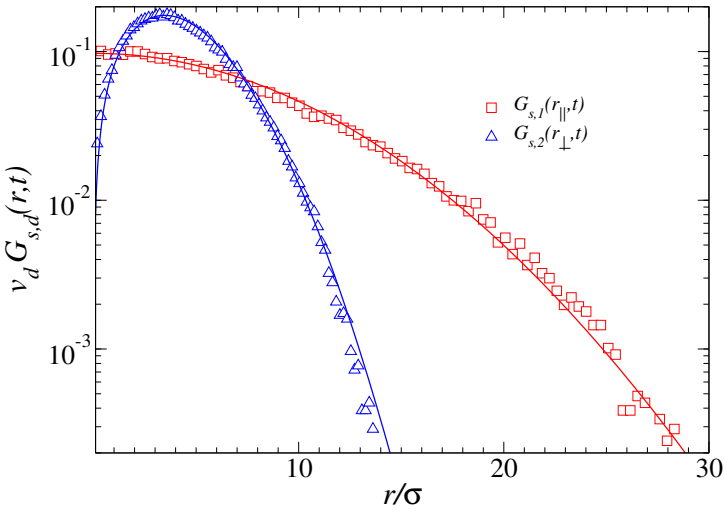

Figure 2.5: Parallel (□) and perpendicular (△) self-van Hove correlation functions for a nematic LC of prolate particles at $t/\tau = 10^3$. Results are normalised by $v_d = 1$ or $2\pi r_\perp$ for $d = 1$ or 2, respectively. Symbols are simulation results. Lines are Gaussian distributions obtained from Eq. 2.5.

most of the function's non-Gaussianity in the following coefficient [90]:

$$\alpha_{2,d}(t) = \frac{\langle \Delta r^4(t) \rangle}{(1+2/d)\langle \Delta r^2(t) \rangle^2} - 1. \tag{2.10}$$

In particular, $\alpha_{2,d}(t)$, which is usually referred to as non-Gaussian parameter (NGP), vanishes if no deviations from Gaussian behaviour are observed. Parallel ($d = 1$), perpendicular ($d = 2$), and total ($d = 3$) NGPs are plotted in Fig.2.7 for nematic phases of prolate particles. Very similar results are observed for oblate particles and are not shown here.

At short time scales, $\alpha_{2,1}$ and $\alpha_{2,2}$ are very close to zero, whereas $\alpha_{2,3}$ is

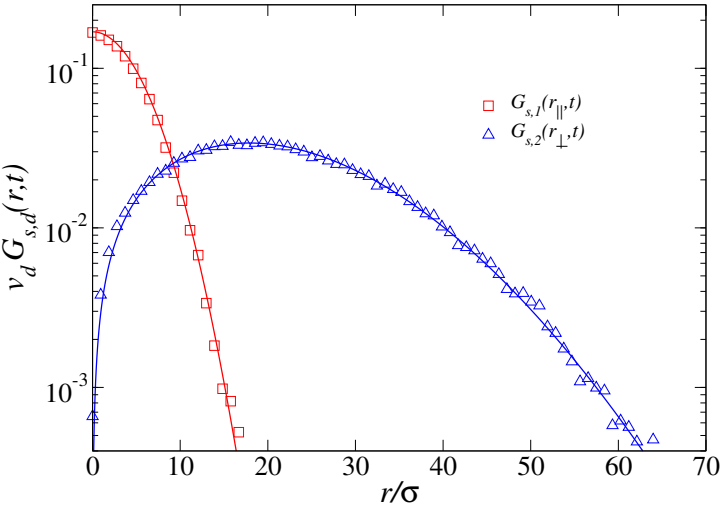

Figure 2.6: Parallel (□) and perpendicular (△) self-van Hove correlation functions for a nematic LC of oblates at $t/\tau = 2 \times 10^4$. Results are normalised by $v_d = 1$ or $2\pi r_\perp$ for $d = 1$ or 2, respectively. Symbols are simulation results. Lines are Gaussian distributions obtained from Eq. 2.5.

clearly positive even at very short times. At intermediate times, when the diffusion is not Fickian, both parallel and perpendicular NGPs are observed to increase, but this tendency is especially evident for the latter, whose maximum value is achieved at approximately $t/\tau = 12$. We notice that the total NGP predicted by Eq. 2.10, $\alpha_{2,3}$, significantly increases in this time regime. At long times, both the parallel and perpendicular NGPs start to decrease, reaching values very close to zero. Different is the tendency displayed by $\alpha_{2,3}$, which seems to reach a maximum at roughly $t/\tau = 10^2$ and then eventually decays over a time scale that goes beyond our simulation time. This result is however obtained by employing a Gaussian form of the self-van Hove function that is not able to describe the dynamics of anisotropic systems. Therefore, by following similar

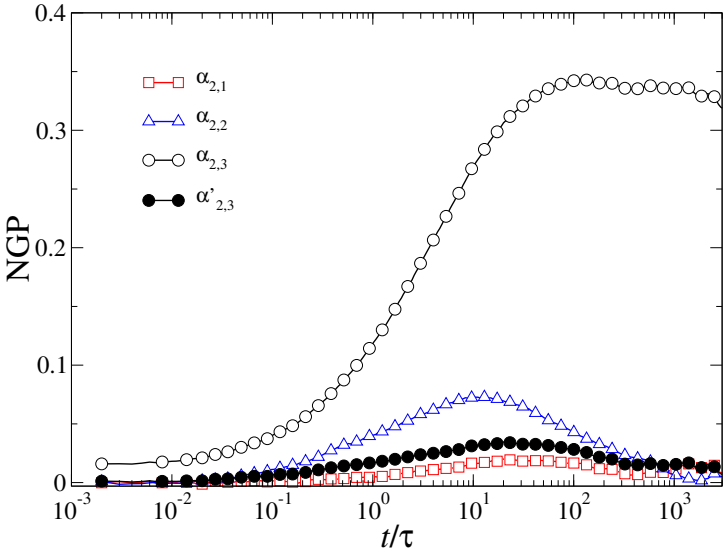

Figure 2.7: Parallel (□), perpendicular (△) and total (○) non-Gaussian parameter for a nematic LC of prolate spherocylinders as calculated from Eq. 2.10. The solid circles (●) indicate the total NGP calculated from Eq. 2.14. Symbols are simulation results and solid lines are guides for the eye.

arguments to those illustrated above, we employ Eqs. 2.8 and 2.9 to derive an expression for the total NGP that incorporates parallel and perpendicular diffusion coefficients. To this end, we first re-write the total NGP as

$$\alpha_{2,d}(t) = K\left[\langle \Delta r^4 \rangle / \langle \Delta r^2 \rangle^2\right]_{\text{sim}} - 1, \tag{2.11}$$

where $K \equiv \left[\langle \Delta r^2 \rangle^2 / \langle \Delta r^4 \rangle\right]_{\text{th}}$ and the functions in $[\cdots]_{\text{sim}}$ and $[\cdots]_{\text{th}}$ are calculated, respectively, by simulation and employing the theoretical distribution of the displacements. More specifically, if we make use of the Gaussian distribu-

tion given in Eq. 2.5, then K takes the values 1/3, 1/2 or 3/5, for d =1, 2 or 3, respectively, and the standard form of the NGP (Eq. 2.10) is recovered. Alternatively, if we incorporate the space anisotropy by using Eqs. 2.8 and 2.9, the theoretical values of $\langle \Delta r^2 \rangle$ and $\langle \Delta r^4 \rangle$ read

$$\langle \Delta r^2 \rangle = \int_0^\infty r^4 G_{s,3}(r,t)\, dr = \left(2D_{t,\parallel} + 4D_{t,\perp}\right) t \tag{2.12}$$

and

$$\begin{aligned} \langle \Delta r^4 \rangle = \int_0^\infty r^6 G_{s,3}(r,t)\, dr = \\ 4\left(3D_{t,\parallel}^2 + 8D_{t,\perp}^2 + 4D_{t,\parallel} D_{t,\perp}\right) t^2 \end{aligned} \tag{2.13}$$

We can now define an alternative form of the NGP, which reads

$$\alpha'_{2,3} = \frac{D_{t,\parallel}^2 + 4D_{t,\perp}^2 + 4D_{t,\parallel} D_{t,\perp}}{3D_{t,\parallel}^2 + 8D_{t,\perp}^2 + 4D_{t,\parallel} D_{t,\perp}} \frac{\langle \Delta r^4 \rangle}{\langle \Delta r^2 \rangle^2} - 1 \tag{2.14}$$

Similarly to the NGP given in Eq. 2.10, also $\alpha'_{2,3}$ can be applied to any particle geometry. The key difference is that $\alpha'_{2,3}$ depends on the instantaneous value of the diffusion coefficients parallel and perpendicular to $\hat{\mathbf{n}}$, as highlighted by the subindex t in the equations above. In particular, to calculate $\alpha'_{2,3}$ over time, the diffusivities $D_{t,\parallel}$ and $D_{t,\perp}$ have been estimated from the instantaneous values of the MSD as obtained by computer simulation. We plot $\alpha'_{2,3}$ in Fig.2.7, where it is

compared to the total NGP, $\alpha_{2,3}$, that has been derived neglecting the anisotropy of diffusion. As already found for $G'_{s,3}(r,t)$, the diffusion at short time scales appears to be Gaussian, with $\alpha'_{2,3} \approx 0$ for $t/\tau < 10^{-1}$. At intermediate times, $\alpha'_{2,3}$ becomes slightly larger than zero, revealing deviations from Gaussian behaviour, which are anyway significantly softer than those detected with $\alpha_{2,3}$ and consistent with those of $\alpha_{2,1}$ and $\alpha_{2,2}$. At $t/\tau > 10^2$, when the diffusion recovers its Fickian nature, $\alpha'_{2,3}$ reaches again values that are very close to zero.

2.3 Compared diffusion in nematic liquid crystals

In this section, we keep discussing the general characteristics of the diffusion in nematic fluids of prolate and oblate particles with (*i*) equal aspect ratio(C_1), (*ii*) equal infinite-dilution translational diffusion coefficients(C_2), and (*iii*) equal infinite-dilution rotational diffusion coefficients(C_3). First, to analyse the relative ability of oblate and prolate particles of identical aspect ratio to diffuse in nematics, we calculate the total long-time diffusion coefficients, $D_l^+ = (2D_{l,\perp}^+ + D_{l,\parallel}^+)/3$ and $D_l^- = (2D_{l,\perp}^- + D_{l,\parallel}^-)/3$, of prolate ($^+$) and oblate ($^-$) geometries, respectively. The resulting diffusivities show that the diffusion of prolate particles in the nematic phase is faster than that of oblate particles. This can be observed in Fig.2.8, where we compare the parallel, perpendicular and total long-time diffusion coefficients in the nematic phase. For the sake of comparison, we also add the diffusivities obtained in the isotropic phase. The dependence of the long time rotational diffusion coefficient (details on its calculation in section 1.2.4) with the packing fraction in the isotropic and nematic phases both for prolate and oblate particles is shown in the inset of figure 3. The qualitative behaviour of D_{rot} is very similar in the two phases. More specifically, in the isotropic and nematic phases and for both oblate and prolate spherocylidenders, D_{rot} decays

at increasing η. This inverse dependence on η is stronger in the isotropic than in the nematic phase. In general, D_{rot} is smaller for oblate than for prolate particles, further confirming that the dynamics of oblate particles is slower than that of prolates. The analysis of the rotational diffusion coefficients does not indicate the occurrence of the non-monotonic behaviour observed for the translational diffusion coefficients.

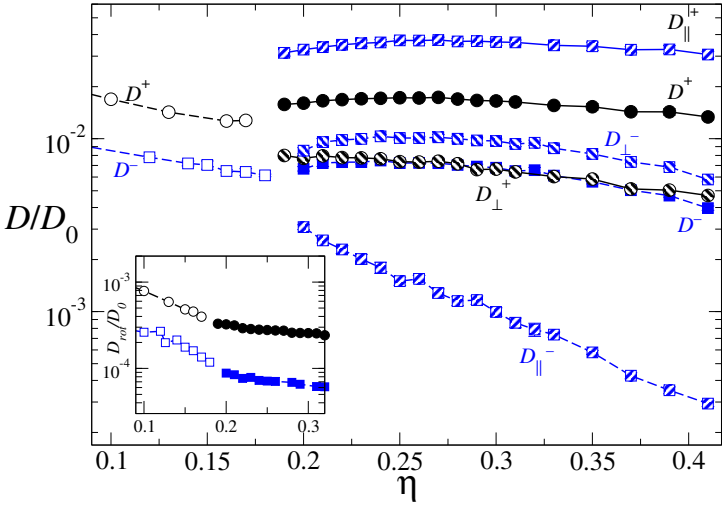

Figure 2.8: Parallel, perpendicular and total diffusion coefficients of prolate (circles) and oblate (squares) spherocylinders as a function of the packing fraction. In the same way, inset show the rotational diffusion coefficient. Shape anisotropy: $a_p = a_o^{-1} = 15.6$. Open symbols refer to the diffusion in the isotropic phase, whereas solid and striped symbols refer to the diffusion coefficients calculated in the nematic phase, as indicated by the labels.

As far as the nematic phase is concerned, the total diffusion coefficient of prolate particles is at least twice as large as that of oblate particles, depending on the packing of the phase. Of the same order of magnitude is the ratio between

the main diffusivities of the two geometries, that is $D^{+}_{l,\parallel} \approx 3D^{-}_{l,\perp}$. If one compares the minor contributions to the total particle diffusivity, prolate geometries are still faster, with $D^{+}_{l,\perp} > D^{-}_{l,\parallel}$, especially at particularly large packing fractions, where the diffusion of oblate spherocylinders along the director decreases dramatically.

The dependence of the diffusivities in the nematic phase on the packing fraction does not appear to be monotonic. In particular, the total diffusion coefficients gradually increase with the system density up to a maximum, beyond which an inverse correlation is found. This tendency is the result of a non-monotonic behavior of the main contributions, $D^{+}_{l,\parallel}$ and $D^{-}_{l,\perp}$, to the total diffusivity, while the minor contributions, $D^{+}_{l,\perp}$ and $D^{-}_{l,\parallel}$, only decrease with increasing η. This behavior, specially clear in the case of oblate particles, had been reported before by de Miguel and co-workers for prolate particles with smaller anisotropy than that studied here [64], and by Jabbari-Farouji for infinitely thin disks [65].

Between $\eta = 0.15$ and 0.2, a phase transformation of the isotropic to the prolate nematic (N^{+}) or oblate nematic (N^{-}) phase is observed. The isotropic to nematic phase transition produces an interesting increase of the diffusion coefficients, regardless the particle anisotropy. In Fig. 2.8, one can see that the diffusivity of prolate and oblate spherocylinders decreases in the isotropic phase with increasing packing fraction, but increases again when the phase transformation is produced. This abrupt change is most likely the consequence of the structural characteristics of the nematic phase. More specifically, the isotropic to N^{+} transition produces the formation of quasi unidimensional channels that act as preferential paths for particle diffusion. The effect is similar for oblate particles, although such preferential paths are found in planes perpendicular to $\hat{\mathbf{n}}$ and thus are quasi two-dimensional. By contrast, in the directions perpendicular

to these channels, the probability of collisions between particles is significantly higher. Although such preferential channels boost the diffusion of prolate and oblate particles in the parallel and perpendicular direction, respectively, to $\hat{\mathbf{n}}$, at increasing packing fractions, they become narrower and narrower and end up hampering, rather than promoting, particle diffusion. This produces the reduction of the diffusion coefficients observed in Fig. 2.8. We notice that the maximum in D is not observed in systems of infinitesimally thin disks [65], where the preferential channels of the N^- phase would never get thinner, at increasing packing fraction, than the particles themselves.

In the light of these results, we now explore the diffusion of prolate and oblate spherocylinders whose infinite-dilution translational diffusion coefficients are the same, namely $D_s^+ = D_s^-$ or, equivalently, $D_{s,\parallel}^+ + 2D_{s,\perp}^+ = D_{s,\parallel}^- + 2D_{s,\perp}^-$. This condition is satisfied by the prolate and oblate particle aspect ratios $a_p = 27$ and $a_o = 0.1$, respectively. Additionally, we have also investigated the case of oblate and prolate particles with identical infinite-dilution rotational diffusion coefficient, that is $D_{s,\vartheta}^+ = D_{s,\vartheta}^-$ (See equation 1.30). For the same oblate anisotropy, that is $a_o = 0.1$, this condition is met for $a_p = 15.6$. The common tendency observed in systems of oblate and prolate particles is that a more pronounced anisotropy (smaller a_o or larger a_p, respectively) determines a slower dynamics along $\hat{\mathbf{n}}$ and perpendicularly to it. This behavior was expected. What we want to understand here is whether or not the relative mobility of prolate and oblate particles changes when an equivalence of diffusivities, rather than a geometric equivalence, is imposed. To this end, in Fig.2.9, we report the ratio between the total MSD of prolate and oblate spherocylinders calculated for the three cases explored here. In particular, circles, triangles and squares show $R_{\mathrm{MSD}} \equiv \langle \Delta r^2 \rangle_{\mathrm{p}} / \langle \Delta r^2 \rangle_{\mathrm{o}}$ for the cases C_1, C_2, and C_3, respectively. The general trend unveils that R_{MSD} decreases at intermediate times, more or less signifi-

cantly for the three cases studied, and then increases again until a saturation plateau that is expected to be observed at long time scales, beyond our simulation time. Of particular relevance is the case scenario C_2, where $R_{MSD} < 1$ over almost three time decades, specifically between $t/\tau = 10^{-2}$ and 40. In this time window, the diffusion of oblate particles is slightly faster than that of prolate particles, a behavior that is not observed in C_1 and C_3, where $R_{MSD} > 1$ over the complete timeline explored. These two cases would indicate that prolate spherocylinders are constantly faster than oblate spherocylinders. However, this conclusion, as we show here, strongly depends on the assumptions made and does not hold if the infinite-dilution translational diffusivities of oblate and prolate spherocylinders are the same.

These considerations are confirmed by the analysis of the self-intermediate scattering function, $F_s(q,t)$, which quantifies the structural relaxation of the system over time. The s-ISFs of oblate and prolate spherocylinders for the cases C_1, C_2, and C_3 are displayed in Fig.2.10, being all calculated at $|\mathbf{q}| = 2\pi/\sigma$, corresponding to the position of the nearest neighboring particles. The complete set of s-ISFs shows a typical fluid-like behavior, with a single decay that is well fitted by a slightly stretched exponential function of the form $\exp[-(t/\tau)^{\alpha}]$, with $\alpha \approx 0.80$ and 0.88 for prolate and oblate spherocylinders, respectively. Left and right frames, which refer to the cases C_1 and C_3, suggest a faster relaxation dynamics of prolate particles as compared to oblate particles. This is especially evident for C_1 (left frame), while for C_3 (right frame) the relaxation of both oblate and prolate particles is very similar, although slightly faster for the latter. An opposite trend is detected for C_2, where the F_s decay of oblate particles slightly anticipates that of prolate particles.

The stretched exponential decay of the self-ISFs would suggest a heterogenous signature of the long-time relaxation dynamics, with single particles trapped

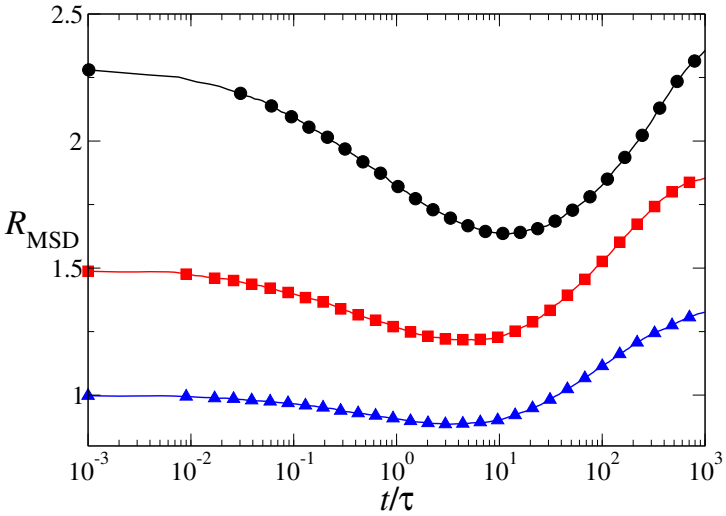

Figure 2.9: Ratio between the MSD of prolate and oblate spherocylinders with identical infinite-dilution translational (blue triangles) and rotational (red squares) diffusion coefficients. For comparison, we also show R_{MSD} for the case of identical aspect ratios (black circles). The packing fraction is $\eta = 0.35$ in all systems.

in transient cages formed by their neighbors. Two possible scenarios might explain such a non-exponential relaxation behavior: a heterogeneous scenario in which the particles relax exponentially at different relaxation rates, and a homogeneous scenario with the particles relaxing in a non-exponential manner at nearly identical rates [91, 92]. In the latter case, a decreasing α would imply an increasing cooperativity, namely a collective motion of particles contributing to the relaxation of the system.

Although the fitting coefficient α is not significantly lower than 1, we addressed the possible occurrence of a collective dynamical behavior by calculating the four-point susceptibility function, $\chi_4(q,t)$, which quantifies the mag-

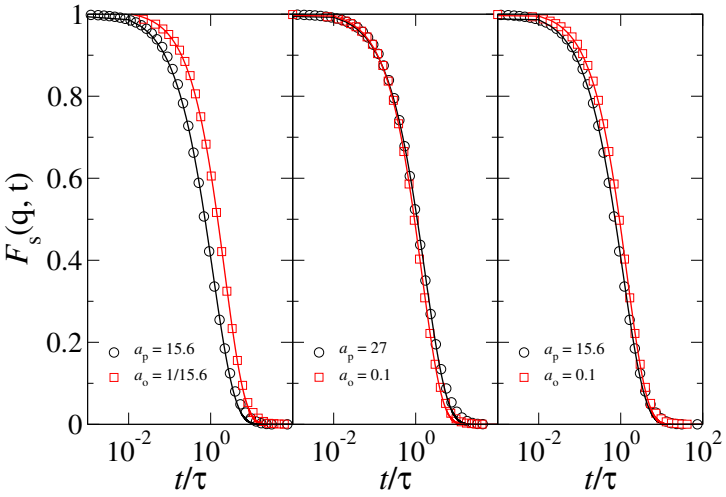

Figure 2.10: (Color online). Total self-intermediate scattering function $F_s(q,t)$ for prolate (black circles and lines) and oblate (red squares and lines) particles for the cases C_1 (left frame), C_2 (middle), and C_3 (right) in nematic liquid crystals with packing fraction $\eta = 0.35$. The solid lines are exponential fits.

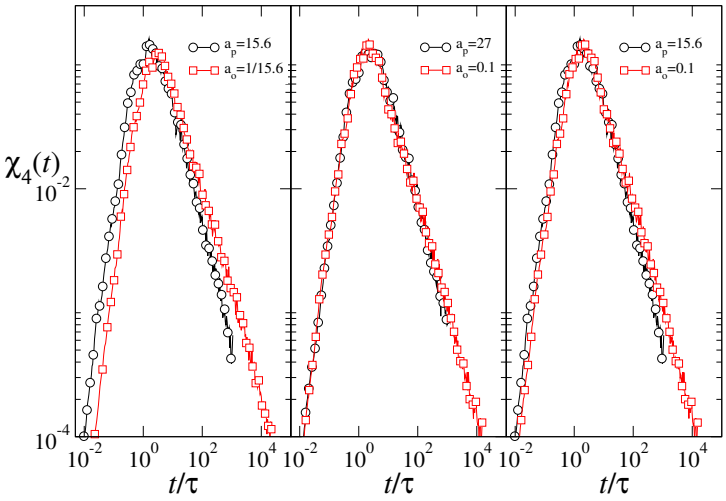

Figure 2.11: (Color online). $\chi_4(q,t)$ at $q = 2\pi/\sigma$ for prolate (black circles and lines) and oblate (red squares and lines) particles for the cases C_1 (left frame), C_2 (middle), and C_3 (right) in nematic liquid crystals with packing fraction $\eta = 0.35$.

nitude of spontaneous fluctuations of the system dynamics as specified in Eq. 1.38 [49–51]. The resulting four-point susceptibilities calculated for oblate and prolate spherocylinders at $|\mathbf{q}| = 2\pi/\sigma$, in each compared case are shown in Fig.2.11. Since $\chi_4(q,t)$ represents the average number of particles that are spatially correlated over time, its very small magnitude over the six decades explored clearly indicates that the dynamics is not cooperative, regardless the anisotropy and diffusion coefficients of the particles. In other words, the relaxation dynamics of nematic LCs relies entirely on the ability of individual particles to diffuse through their neighbors, with no sign a cooperative behavior as previously observed in smectic LCs [67,68].

2.4 Conclusions

In summary, we have investigated the dynamics in nematic liquid crystal phases of anisotropic particles, here modeled as oblate and prolate spherocylinders that confirm previous results [64,65] and enrich the global picture of transport of particles in the nematic phase. In particular, our comparative study unveils that the generally accepted ability of prolate particles to diffuse faster than their oblate counterparts strongly depends on how this comparison is practically operated. The structural features of this phase have a strong impact on the diffusion of particles, which abruptly increases across the isotropic-to-nematic transition. Despite the stretched exponential decay of the s-ISFs, which might imply the presence of a collective motion, the analysis of the four-point susceptibility function, $\chi_4(q,t)$, does not reveal any tangible signature of spatial correlations and thus excludes the occurrence of cooperative dynamics.

To have further insight we compared prolate and oblate spherocylinders with identical infinite-dilution translational diffusion coefficients, finding that the dynamics of oblate particles is faster in a significant time window as the MSD

indicates. Additionally, under these conditions, the decay of the corresponding s-ISFs suggests a faster relaxation of systems of oblate particles. The diffusion in the nematic phase, regardless the particle geometry, displays a strong directional character, with a fast and slow component. It is remarkable that the relative relevance of the diffusion in the direction parallel and perpendicular to the nematic director is interchanged between prolate and oblate particles, being faster the diffusion parallel to the director in calamitic nematic fluids, while this role is taken by the perpendicular diffusion in discotic particles.

This system also gave us a good opportunity tu study the impact of space anisotropy in the fickean difussion and its gausianity. Cloncluding that FNG diffusion is not ubiquitous in soft matter. More explicitly, we found that colloidal particles in nematic LCs display a Fickian and Gaussian dynamics at short and sufficiently long time scales, while at intermediate times, when the particles experience a caging effect imposed by their neighbours, the diffusion is sub-diffusive and non-Gaussian. We have shown that the Fickian and Gaussian dynamics of colloidal nematic LCs cannot be appreciated by a distribution function of particle displacements that assumes space symmetry and calculated via the standard self-van Hove correlation function. To overcome this limitation, we propose an ellipsoidal Gaussian distribution that takes into account the diffusion coefficients parallel and perpendicular to the nematic director. This new distribution function is able to reproduce our simulation results with remarkable precision and is crucial to understand the nature of the diffusion in colloidal LCs, which does not show evidence of an FNG signature. The new form of the self-van Hove functions is applied to formulate a non-Gaussian parameter that incorporates the instantaneous value of the diffusion coefficients and is able to quantify deviations from Gaussian behaviour more precisely.

Chapter 3

The OGBK model. Possibilities, limitations and new phases

Digging in the history of the study of intermolecular forces, we find one of the first attempts to understand them in the capillarity forces studied by Clairault (1743), then he found uncanny that forces between particles appeared only between water and glass and only in their interfacial annulus. His attempt to solve this problem and the ones by other great scientists put a gravitational origin in the interaction between the constituents of matter. And it wasn't until the quantum theory of long range forces and the London formulas (1930), when the true nature of intermolecular forces began to be understood [93].

But often, the problems we would like to solve are too big to be solved by means of quantum mechanics. So we are forced to simplify electrons interactions up to the level of the Born-Oppenheimer approximation, this means we

can use empirical force fields were atomic bonds are treated as springs which stretch,bend or twist, keeping a surprisingly good performance and employing much less computing time. In this same spirit we can keep up this approximation and omit bonded interactions of atoms and focus now on the non-bonded ones. All these simplifications will lead us to the coarse grain force fields, where we can address electrostatic or van der Waals forces separately.

On one side, electronegativity of atoms present in a molecule can cause a anisotropic distribution of charge. This is usually modelled with point charges whose amount and position are controlled by parameters that fit the overall electrostatic interaction as a sum of pairs of charges interacting by Coulomb's law. But in cases where we find a non-zero electric moment, a central multipole expansion can be more convenient, using dipoles, quadrupoles, octopoles, etc.

Whereas on the other side, the van der Waals forces are often understood as a balance between long range attractive forces and short range repulsive ones. On one hand the dispersive forces sometimes called London forces, are due to the formation of instantaneous dipoles cause by fluctuations. For them, Drude proposed a model predicting a dispersion interaction proportional to $1/r^6$ for the dipole-dipole case, that can be extended to quadrupoles or higher orders with a series expansion. On the other hand the repulsive contributions can be attributed to the Pauli principle, producing overlap forces in electrons with the same spin. One of the most used functions to take care of both interactions is the Lennard-Jones function, which in its more general form can be written as:

$$U(r) = k\varepsilon\left[(\sigma/r)^n - (\sigma/r)^m\right]; \quad k = \frac{n}{n-m}\left(\frac{n}{m}\right)^{m/(n-m)} \tag{3.1}$$

Being m and n two natural numbers, σ the collision parameter and ε the well depth. While choosing m=6 has the afore mentioned theoretical motivation, choosing n=12 has non particular one, but it gives nice results for rare gases, meanwhile it would be too steep for more complex systems where an exponen-

tial decay as $exp(-2r/a_0)$, being a_0 the Bohr radius, is predicted by quantum mechanics [94]. Many modifications of it end in good empirical force fields where the term with the $(1/r)^{12}$ dependence is substituted by something more suitable, like the Buckingham Potential, but even a simple 12-10 Lennard-Jones can be used to model hydrogen bonding, like the YETI force field [95]. Often the understanding of the evolution and previous uses of a function can help us to foresee further applications of it. So in order to assess the applicability of the forcefield employed in this study, the OGBK (Oblate-Gay-Berne-Kihara) model [27], we will focus on the components exposing them chronologically.

We should start more than sixty years ago when Taro Kihara proposed a core potential of intermolecular forces of non-polar polyatomic molecules [96]. There he introduced a parameter modifying the usual Lennard-Jones potential to express the minimum distance (d_m) between impenetrable molecular cores, what is a fair coarsed-grain approximation using convex cores.

$$U_K(d_m) = 4\varepsilon \left[(\sigma/d_m)^{12} - (\sigma/d_m)^6 \right] \tag{3.2}$$

Later on, Berne and Pechukas spoke of Kihara's potential as a model with a geometric interpretation and introduced a more analytical perspective formulating a potential using the overlap of gaussians associated to ellipsoids of revolution representative of the space filled by molecules [97]. That model to the contrary of many to date, was differentiable and used analytical (not numerical) parameters for the pairwise interactions readily for varying degrees of anisotropy. If we take the main axis of the objects $\mathbf{u_i}$, $\mathbf{u_j}$ and their relative positions $\mathbf{r}$, as the vectors depicted in figure 3.1, it can be written like this:

$$U_{GO}(\hat{u}_i, \hat{u}_j, r) = \varepsilon_0 \varepsilon_{GO}(\hat{u}_i, \hat{u}_j)\, exp\left[-R^2/\sigma^2(\hat{u}_i, \hat{u}_j, \hat{r}) \right] \tag{3.3}$$

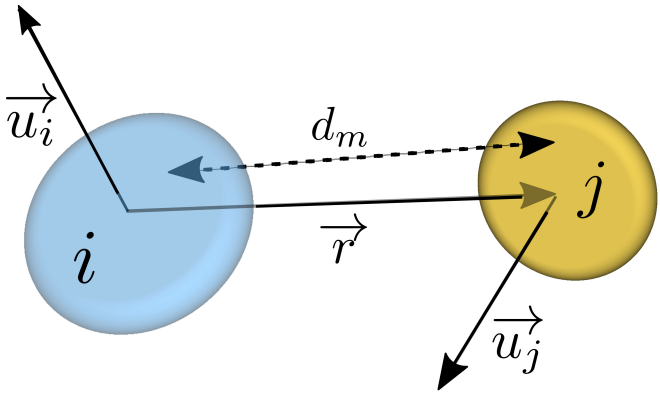

Figure 3.1: Molecules i and j with their respective unitary vectors $\mathbf{u_i}$ and $\mathbf{u_j}$ pointing along their revolution axis, and vector r joining their centres.

where ε_0 is a constant and $\varepsilon_{GO}(\hat{u_i}, \hat{u_j})$ is the strength parameter expressed as follows:

$$\varepsilon(\hat{u_i}, \hat{u_j}) = \left[1 - \chi^2 (\hat{u_i} \cdot \hat{u_j})^2\right]^{-1/2} \tag{3.4}$$

and $\sigma(\hat{u_i}, \hat{u_j}, \hat{r})$ the range parameter isε_0:

$$\sigma(\hat{u_i}, \hat{u_j}, \hat{r}) = \sigma_0 \left(1 - \frac{1}{2}\chi\{\frac{(\hat{r} \cdot \hat{u_i} + \hat{r} \cdot \hat{u_j})^2}{[1 + \chi(\hat{u_i} \cdot \hat{u_j})]} + \frac{(\hat{r} \cdot \hat{u_i} - \hat{r} \cdot \hat{u_j})^2}{[1 - \chi(\hat{u_i} \cdot \hat{u_j})]}\}\right)^{-1/2} \tag{3.5}$$

where χ is the anisotropy parameter defined trough the aspect ratio $\kappa = L/\sigma + 1$ as:

$$\chi = (\kappa^2 - 1)/(\kappa^2 + 1) \tag{3.6}$$

and σ_0 usually $\sqrt{2}$ times the perpendicular semi-axis:

Taking this Gaussian overlap potential Gay and Berne offered a modification of it to mimic a linear four site-site potential overcoming some unphysical features [98], through two changes. First introducing the range parameter inside the

Lennard-Jones to displace the wells instead of dilate them. And second defining a new strength parameter $\varepsilon_{GB}(\hat{u}_i, \hat{u}_j, \hat{r})$ which is now a function of $\hat{r}$ as well. Respectively formulated as follows:

$$U(\hat{u}_i, \hat{u}_j, \hat{r}) = \varepsilon_0 \varepsilon_{GB}(\hat{u}_i, \hat{u}_j, \hat{r}) \left[\left(\frac{1}{r - \sigma(\hat{u}_i, \hat{u}_j, \hat{r}) + 1} \right)^{12} - \left(\frac{1}{r - \sigma(\hat{u}_i, \hat{u}_j, \hat{r}) + 1} \right)^{6} \right] \tag{3.7}$$

$$\varepsilon_{GB}(\hat{u}_i, \hat{u}_j, \hat{r}) = \varepsilon_{GO}^{\nu}(\hat{u}_i, \hat{u}_j) \, \varepsilon'^{\mu}(\hat{u}_i, \hat{u}_j, \hat{r}) \tag{3.8}$$

This new strength parameter is just the old one multiplied by $\varepsilon'(\hat{u}_i, \hat{u}_j, \hat{r})$, what is in fact $1/\sigma^2$ where χ was substituted by χ':

$$\varepsilon'(\hat{u}_i, \hat{u}_j, \hat{r}) = 1 - \frac{1}{2}\chi' \left[\frac{(\hat{r} \cdot \hat{u}_i + \hat{r} \cdot \hat{u}_j)^2}{1 + \chi'(\hat{u}_i \cdot \hat{u}_j)} + \frac{(\hat{r} \cdot \hat{u}_i - \hat{r} \cdot \hat{u}_j)^2}{1 - \chi'(\hat{u}_i \cdot \hat{u}_j)} \right] \tag{3.9}$$

Being χ' formulated from the strength proposed for the edge to edge configuration ε_e and the side to side configuration ε_s as follows :

$$\chi' = (\varepsilon_s^{1/\mu} - \varepsilon_e^{1/\mu}) / (\varepsilon_s^{1/\mu} + \varepsilon_e^{1/\mu}) \tag{3.10}$$

Even though the Gay-Berne potential has been extensively used for both prolate and oblate geometries, we cite here just a few applications among the most representative for this work. As could be the example of coronene [99] or other to discotic molecules [100].

The described model uses ellipsoids of revolution, what still seems inaccurate to describe de electronic clouds of molecules, this model was improved later on by Martinez-Haya and Cuetos [27], applying Kihara's perspective to it. The

Lennard-Jones like part of the potential is now a function of the minimum distance between two segments for the case of a prolate, and can be extended for the case of oblates using the minimum distance between two disks. Representing now these molecular shapes as spherocylinders. (see figure 3.2).

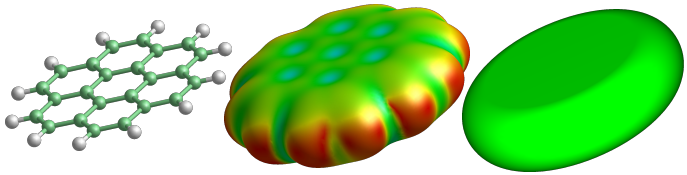

Figure 3.2: From left ro right. Molecular model of coronene [101], isosurface [101] of the molecule and spherocylinder of $a_o = 0.3$

The final expression for the potential combining equations (3.2) and (3.8) is:

$$U(\hat{u_i}, \hat{u_j}, \hat{r}) = \varepsilon_{GB}(\hat{u_i}, \hat{u_j}, \hat{r}) U_K(dm) \tag{3.11}$$

Summarizing, this simple modification we can now represent the electronic cloud of molecular discogens with very different aspect ratios or even a colloid of discotic shape. So given κ (particle's aspect ratio) if we define now the parameter $\kappa' = \varepsilon_s/\varepsilon_e$ we can characterize the interaction anisotropy with only three parameters (κ', ν, and μ). That would yield an attractive energy well of a parallel pair of molecules in the edge to edge configuration being κ' times, $(1-\chi^2)^{-\nu/2}$ times and $(1-\chi^2)^{-\nu/2}(1-\chi')^{-\mu}$ times deeper than for the face to face, crossed and T-shaped configurations respectively(see figure3.3). The GBK has been previously used for prolate [27] and oblate [102, 103] particles, but only in a reduced number of parameters' sets. Here we focus on oblate ones and explore the different usable sets in order to find further potentialities of the model.

3.1 Classification, Possibilities and Limitations

The $D_{\infty,h}$ symmetry of oblate particles yields four canonical relative orientations that can be understood as the building blocks of any ordered structure composed with them. These orientations are depicted in figure 3.3 with the following nomenclature according to the position of the principal axes of the particles, referencing from the one which coincides with the revolution axis (RA) that would transform the two-dimensional curve in a three-dimensional oblate shape:

- "F" when they share RAs.
- "E" when their RAs are parallel and share another principal axis.
- "C" when their RAs are perpendicular and a different principal axis is shared.
- "T" when RAs are perpendicular, being one of them shared by another principal axis of the other.

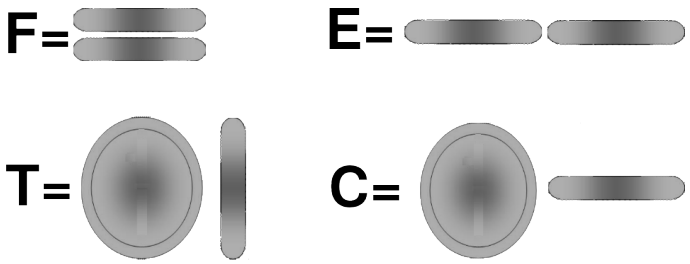

Figure 3.3: The four canonical relative orientations possible for oblates particles. F(face to face),E(edge to edge),T("T" shape) and C(cross shape)

Picking carefully the parameters in the OGBK potential we can favour any of the canonical orientations over the others, setting it as the more intense interaction. Feature that was chosen to stablish a first approach towards the classification of

parameters' sets, therefore we will the nomenclature U_F, U_E, U_T or U_C if the configurations F, E, T or C are favoured over the others respectively, or combination of letters if two of them have the same depth and the others are shallower. This ability to control the anisotropy of the potential turns it in a powerful tool, since it allows to model very different systems like cells, colloids or even polycyclic aromatic hydrocarbons. And at the same time, it represents an opportunity for theoretical studies, because it allows to tune the orientational dependence of particles within a wide range of anisotropies with only three parameters. Therefore, it is easily applicable to many systems or even as a test environment to key-lock models.

The proposed classification can be better understood looking at the plots of energy as a function of the centre of mass separation in units of $(r* = r/(L+\sigma))$ (see fig. 1.1) keeping the relative angles formed by $\mathbf{u_i}$, $\mathbf{u_j}$ and $\mathbf{r}$. There are presented each set of parameters separately with a curve for each of the four canonical orientations (figs. 3.4, 3.5, 3.6 and 3.7). In that sense we are fixing the angles due to their practical importance, but we should always bear in mind that we are dealing with a continuous potential as a function of the minimum distance between two disks and three angles (the RAs relative angle and the two angles that those form between each of them and the straight line passing through both centres), therefore two different sets of parameters may have wells with the same minimal values, having a different angular dependence.

The complex equation used to compute potential energy has some limitations regarding usable parameters, because in some cases we might incur into unphysical situations or mathematical singularities, as it happens with $k' < 0$. Being also problematic many cases between $-1 < \nu < 1$, and $-1 < \mu < 1$, where even if we compute the necessary exponentiations as $x^y = e^{y\ln(x)}$, we could find complex numbers as a result.

With the application of the "Inverse function theorem" [104, 105] we would find the domains and images of the OGBK potential but any information obtained would be difficult to visualize or understand due to the high number of variables (the three parameters for the angular dependence, the aspect ratio, minimum distance and three angles). To overcome this in a more practical way, we focused on the wells minima for the canonical orientations and performed an exploration of the input parameters to filter the ranges of interest of them. The oblate anisotropy a_o (as defined in section 1.2.1) was evaluated from 0.1 to 1.0 at 0.1 steps. k' was evaluated from 0.1 to 1.0 at 0.1 steps. ν and μ were evaluated from -10 to 10 at 0.1 steps. From that we omitted wells deeper than 50 ε since those would be highly unlikely to appear in a real system.

The filtering of data from the exploration yielded some necessary but no sufficient rules to obtain a desired interaction potential showed in table 3.1, this mostly implies that even following those rules sometimes the result is a potential with all wells of the same depth within a difference of 0.01ε (examples in sets 11 and 12 of table 3.2), any U_T type (set 3) proves that rule for U_F is not warranty of it and sets 11, 12 and 13 proves the insufficiency of the rules for U_C, U_T and U_E respectively. It is also worth mentioning that this rules and the examples of table 3.2 arise from the described exploration, therefore a thorough investigation of the parameters may unveil more detailed results, what is out of the scope of this study.

From the exploration performed, some sets of parameters are showed in table 3.2 as extreme examples of the possibilities found ranking the well minima among the canonical orientations. From a pragmatical point of view, some obtained potentials may result in very interesting systems to study theoretically but unfeasible in practice. The first four rows of the table show examples where the deepest well is at least 8 times deeper than any of the others, in the following we

U_E	$\kappa' < 1$	$\nu > 0$	-
U_F	$\kappa' > 1$	-	-
U_T	$\kappa' > 1$	$\nu < 0$	$a_o < 0.9$
U_C	$\kappa' < 1$	$\nu < 0$	-

Table 3.1: Necessary but no sufficient rules to obtain a dominant orientation OGBK potential, according to aspect ratio and parameters k' and ν

can observe special cases where at least two wells are equally deep. This is easy to understand observing the effect certain parameters have on the final expression of the potential. For example all sets where $\kappa' = 1$ will result in wells of E and F configurations being equally deep (sets 7 and 9), $\nu = 0$ will make wells of E and C configurations equally deep (set 6),$\mu = 0$ will make wells of T and C configurations equally deep (sets 8,11-13). Sets 5 and 7 are examples of this hybrid types U_{EC} and U_{TC} obtained without $\nu = 0$ or $\mu = 0$. Finally, sets 14 to 17 are the worked examples in this study. Is important to remark that this values for the wells are rounded up to 0.1ε and also, to keep in mind that even if we find different sets which result in wells of the same depth, these are canonical configurations and the rest of values for other orientations might differ.

3.1.1 Structures and Self-Assembly

There is a vast amount of possible combinations of parameters so in order to show the effects of the application of this potential we limited the simulations to four characteristic sets running NPT-MC simulations along three isotherms for four sets of parameters each favouring one of the canonical orientations in a rather realistic way instead of being extreme examples. With the same spirit all simulations were performed at $a_o = 0.1$. But is important to take into account

Set #	κ'	ν	μ	a_o	E	F	T	C	Type
1	0.1	1.5	-10.0	0.1	-11.3	-1.1	-0.3	-1.0	U_E
2	10.0	0.1	0.2	0.1	-1.2	-11.7	-1.1	-1.0	U_F
3	10.0	-4.2	-0.2	0.1	-0.001	-0.01	-8.7	-1.0	U_T
4	0.1	-2.7	0.2	0.1	-0.01	-0.001	-0.1	-1.0	U_C
5	0.1	-0.1	0.2	0.7	-1.0	-0.1	-0.1	-1.0	U_{EC}
6	0.1	0.0	0.3	0.1	-1.0	-0.1	-0.1	-1.0	U_{EC}
7	1.0	-1.6	-0.1	0.1	-0.1	-0.1	-1.0	-1.0	U_{TC}
8	0.1	-1.6	0.0	0.1	-0.1	-0.1	-1.0	-1.0	U_{TC}
9	1.0	1.5	-10.0	0.1	-11.3	-11.3	-1.0	-1.0	U_{EF}
10	10.0	-0.6	-0.2	0.5	-0.9	-8.7	-8.7	-1.0	U_{FT}
11	0.1	-0.1	0.0	0.7	-1.0	-1.0	-1.0	-1.0	U_{EFTC}
12	1.1	-1.7	0.0	0.9	-1.0	-1.0	-1.0	-1.0	U_{EFTC}
13	0.1	-9.8	0.0	1.0	-1.0	-8.7	-8.7	-1.0	U_{FT}
14	0.1	1.0	1.0	0.1	-5.0	-0.5	-0.2	-1.0	U_E
15	2.0	0.2	2.0	0.1	-1.4	-2.7	-1.4	-1.0	U_F
16	1.9	-0.4	-0.1	0.1	-0.5	-1.0	-1.8	-1.0	U_T
17	0.1	-1.3	0.3	0.1	-0.1	-0.01	-0.1	-1.0	U_C

Table 3.2: This table shows in columns; the set number (1), the potential parameters (2-4), the anisotropy (5), the minimum energy in each configuration in reduced units (U/ε) (6-9) and the correspondent clasification (10). And stores in rows, some extreme (1-4), special example sets (5-10), sets evidencing the insufficiency of the provided rules (11-13) in table 3.1 from the ranges of parameters studied and the worked examples of this study (14-17). A combination where all well minima are -1.0 can be found for many sets of parameters

that the width of the wells in the OGBK model is controlled by the aspect ratio used, parameter which also affects the excluded volume. These two features have a mayor impact on the aggregation process, resulting in different structures formed for the same potential along a range of the aspect ratio.

First we ran several trials starting from the same isotropic configuration at very low density for several parameters' sets of each type (E,F,T and C). Starting from a simulation box in length units of $D = (L + \sigma)$, filled with $N = 1260$ particles at $\rho^* = 0.002N/D^3$ and pressure $P^* = 0.0001(PD^3/\varepsilon)$ NPT-MC simulations were performed along isotherms at temperatures of $T* = 0.1(-U_{min})$ where U_{min} is the deepest well in each case in $\kappa_B T$ units. To observe the formation of aggregates in each set. The cluster move described in section 1.2.5 was useful to equilibrate densities up to around 0.1 particles per volume unit (σ^3), what for $a_o = 0.1$ usually means that all particles are in the same cluster. From that point on, the equilibration process can become unreachable due to the loss of ergodicity. This motivated a different approach to investigate phases of higher packing fraction.

With this procedure we always found that the aggregates formed clearly manifest in their structure when the intensity of the attraction in one of the canonical orientations overcomes the others. Here we only show one example cluster for each potential type inserted in the representations of the energy for each canonical orientation (F, T, E and C) as a function of the distance of particles' centres $r* = (r/D)$. For the U_F type (Fig. 3.4) we can observe particles attach to each other forming columns, which in turn are stuck because the E configuration also minimizes the energy of the system to a lesser extent. For the U_E type (Fig. 3.5) we can observe that particles form sheets in clusters of few layers.

In the U_T type case (Fig.3.6) we can observe intricate patterns of the struc-

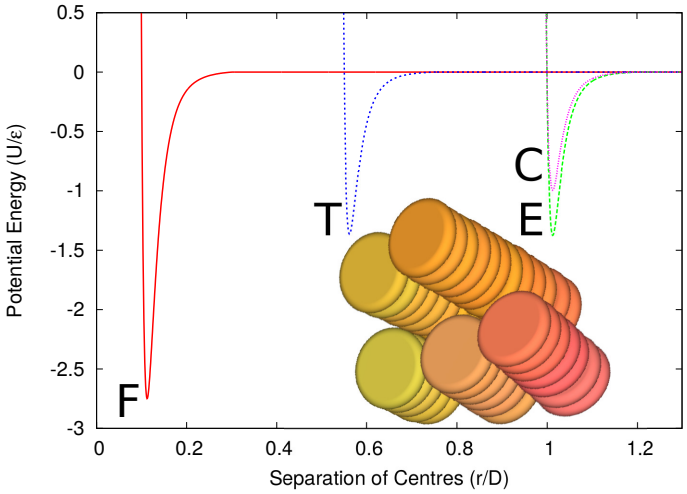

Figure 3.4: Interaction Energy in each of the four canonical configurations for the U_F type potential with parameters, $\kappa = 0.10$, $\kappa' = 2.00$,$\nu = 0.20$ and $\mu = 2.00$ with typical aggregate inserted showing the effect of having the F configuration as an energy minimum, with each curve marked with the letter of the orientation that produces it.

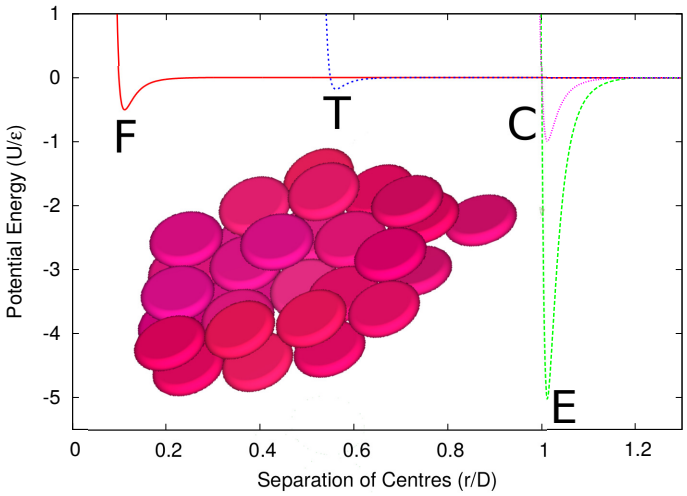

Figure 3.5: Interaction Energy in each of the four canonical configurations for the U_E type potential with parameters, $\kappa = 0.10$, $\kappa' = 0.10$, $\nu = 1.00$ and $\mu = 1.00$ with typical aggregate inserted showing the effect of having the E configuration as an energy minimum, with each curve marked with the letter of the orientation that produces it.

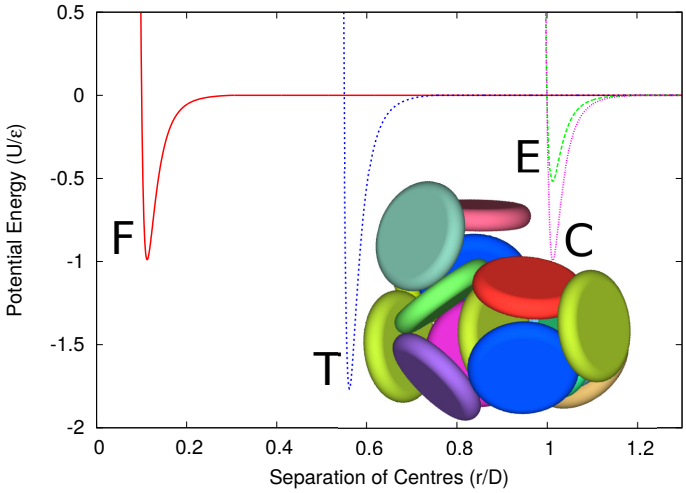

Figure 3.6: Interaction Energy in each of the four canonical configurations for the U_T type potential with parameters, $\kappa = 0.10$, $\kappa' = 1.90$,$\nu = -0.40$ and $\mu = -0.10$ with typical aggregate inserted showing the effect of having the T configuration as an energy minimum, with each curve marked with the letter of the orientation that produces it.

ture commonly named house of cards, to describe the networks formed in clays [106, 107], in reference to this porous aggregates. In this case is important to remark that to the contrary from previous simulation studies, here the distribution of charges of opposite signs is not modelled yet, it just happens for the T configuration to minimize the energy, as if it was a key-lock model.

Finally, for the U_C type (Fig.3.7) we can observe structures where particles tend to be surrounded by others in C configuration, resembling entangled accordions, of which we could not find previous reference in the literature

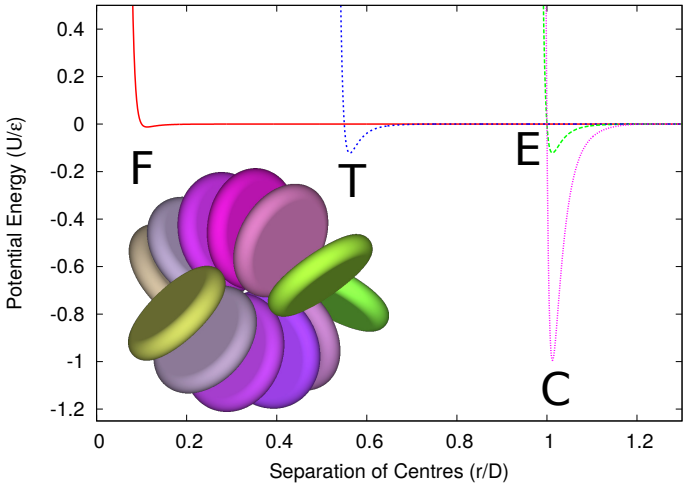

Figure 3.7: Interaction Energy in each of the four canonical configurations for the U_C type potential with parameters, $\kappa = 0.10$, $\kappa' = 0.10$,$\nu = -1.30$ and $\mu = 0.30$ with typical aggregate inserted showing the effect of having the C configuration as an energy minimum, with each curve marked with the letter of the orientation that produces it.

3.2 Phases and State Diagrams of characteristic potentials

In a previous study of Marechal *et al.* the phase diagram of hard oblate spherocylinders was determined for different aspect ratios and packing fractions [108]. There we find four possible phases according to particles ordering, the isotropic phase with particles randomly oriented as it happens in liquids and gases, the nematic phase with particles roughly parallelly oriented as it is the case for liquid crystal systems, and two types of solid phases, the columnar, where particles are arranged in parallel columns, but to the contrary from the tilted phase, our other solid phase, particles are not necessarily parallel within the column. We can observe an example of each one of this four phases in figure 3.8. Looking at the bibliography we can find examples of these phases obtained also when the Gay-Berne potential is applied [100] to discotic molecules. There have been also studies of the tilted phase, trying to model crystals of coronene with it [109]. But our approach tries to be less specific and give a broader perspective in terms of orientations of the interactions and their repercussion.

For this study we foresaw a conceptual phase diagram (see figure 3.9) where for a high temperature, defined as $T^* >> -U_{min}$ being U_{min} the deepest well of the chosen potential. The phases found should be qualitatively the same as for the study of Marechal *et al.*, since particles would be freed from their attractions. Therefore, at these temperatures we should only observe small differences in the phase diagram, because our particles behave effectively as soft oblate spherocylinders. But as the temperature decreases, a plethora of new metastable phases can appear between the highly packed tilted phase at high pressures (where the entropic term governs the free energy) and the isotropic phase at very low pressures. Under already mentioned conditions of tempera-

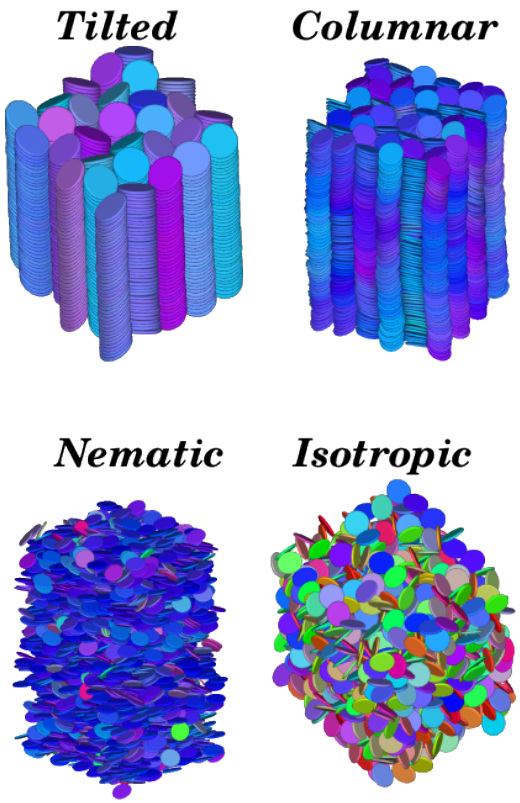

Figure 3.8: Snapshots of phases obtained at high temperatures for oblate spherocylinders under GBK interactions. These phases are also found for hard oblates of the same anisotropy $a_o = 0.1$ (colours depicting particles orientations)

ture and pressure for metastable phases, particles are trapped into regions of the phase space during an unpredictable amount time, resulting in a loss of ergodicity, provoking a huge hysteresis in the simulations.

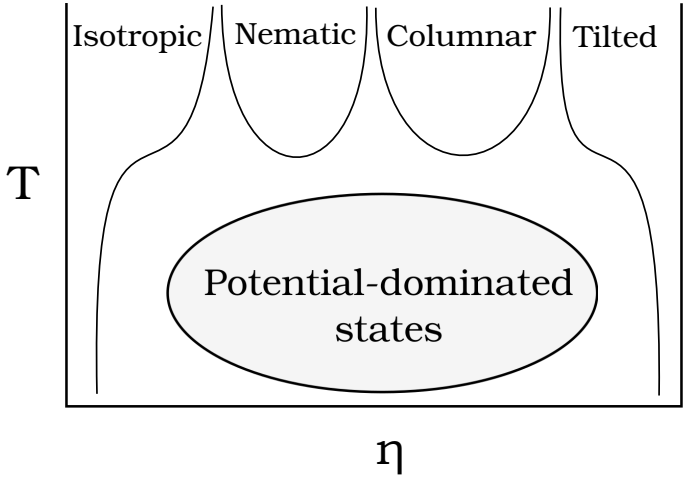

Figure 3.9: Conceptual phase diagram predicted for oblate spherocylinders of $a_o = 0.1$ subjected to the GBK potential (for any set of parameters κ',ν and μ).

3.3 Simulations Details

According to the predicted phase diagram we decided to run MC simulations in the NPT ensemble along three isotherms for every chosen set of parameters. One at a temperature $T^* = -2U_{min}$, one at $T^* = 1U_{min}$ and one at $T^* = 0.5U_{min}$, where U_{min} is again the deepest well of each set (see table 3.2). To have a common framework all temperatures displayed are scaled with ε (see equation 3.1) as $T^* = \kappa_B T/\varepsilon$ After the observation of hysteresis in the system during previous test, we chose to perform MC simulations in the Isotension-Isotermal ensemble for every desired pressure with a constant number of particles $N = 1260$, pick-

ing a highly packed tilted phase as the starting point of every one and allowing changes in shape and volume as described in section 1.2.3 until equilibration. As a test we checked that starting from a columnar configuration we can arrive to the same phases under the same conditions of pressure and temperature, with the caveat that the tilted phase takes much longer to be equilibrated under this initial configuration.

3.4 Results

The results of our simulations are aligned with our prediction of the phase diagrams. For isotherms at high temperatures we could only find the same phases hard oblate spherocylinders have in their phase diagram at an anisotropy of $a_o = 0.1$ in the four cases (see figures 3.10, 3.11, 3.14 and 3.16). For the isotherms at medium and low temperature every type of potential deserves a separate discussion.

At medium or low temperatures we found structures that were stable for more than 10^6 MC cycles at intermediate pressures. This means different types of ordering favoured by the minimization of energy, this entails the metastability of the columnar phase at lower pressures than expected for it in the F type potentials. Meanwhile, for the T, C and E types, it meant the appearing of the Uniaxial(Fig.3.15), Cubatic(Fig.3.17) and Discotic-Smectic (Fig.3.12) phases respectively. This last two has been previously reported by several authors for different particles like [110–112]. And the type of aggregation found in T type potentials is present in many systems, from cells [113] to asphaltenes [114] or simpler polycyclic aromatic hydrocarbons [115] but our model offers the possibility to engineer their self-assembly simply by choosing the set of parameters wisely.

Though at intermediate pressures these systems are hard to equilibrate, the

U_F potential type does not offer any metastable phase at the temperatures investigated after 10^6 cycles. The isotherms of this potential have a common feature with the others, having a stable isotropic phase with increasing temperature at low packing fractions, corroborating the assumption of our conceptual phase diagram. The region of the isotherms occupied by metastable phases for other types of potential is filled here with the columnar phase. This was to be expected since this configuration minimizes the energy of the system, this fact also pushes the tilted phase to higher pressures (see fig.3.10).

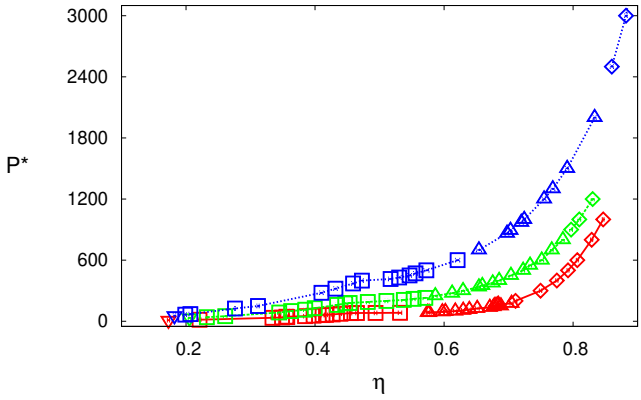

Figure 3.10: Isotherms of the U_F type potential with parameters, $\kappa = 0.10$, $\kappa' = 2.00$,$\nu = 0.20$ and $\mu = 2.00$, showing pressure P^* in reduced units as a function of packing fraction η at temperatures $T^* = 1.38$, $T^* = 2.75$ and $T^* = 5.50$ in solid (red), dashed (green) and dotted (blue) lines respectively. (Error bars within the points size). Where symbols show different phases as, □ for nematic, ▽ for isotropic, △ for columnar, ◇ for tilted and ● for Discotic-Smectic phase.

The low temperature simulations of the U_E potential allowed us to find the Discotic-Smectic phase (see fig.3.12) for oblate particles at lower aspect ratios than obtained in previous studies [112], because in our case this phase does

not arise from entropic reasons as it happens for hard particles of higher aspect ratios. The Discotic-Smectic phase in fluids of discotic particles have been reported very few times in both experimental [116–118], and simulation studies of parallel particles or oblate particles with non-discotic shape [119, 120]. This is a proof of the versatility of the OGBK potential to model different kind of fluids. At this temperature we can also observe the persistence of the nematic phase over a wider range of pressure.

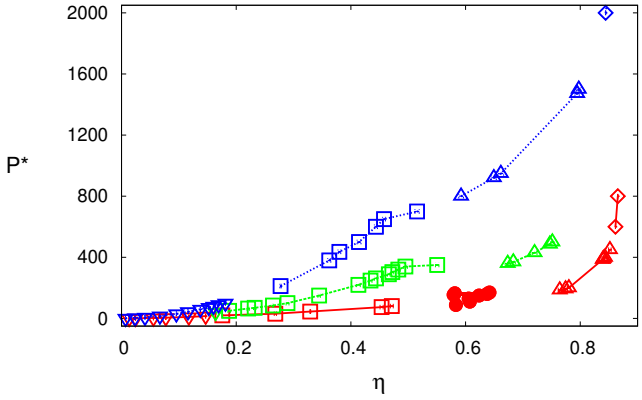

Figure 3.11: Isotherms of the U_E type potential with parameters, $\kappa = 0.10$, $\kappa' = 0.10$, $\nu = 1.00$ and $\mu = 1.00$, showing pressure P^* in reduced units as a function of packing fraction η at temperatures T=2.50, T=5.00 and T=10.00 in solid (red), dashed (green) and dotted (blue) lines respectively. (error bars within the points size). Where symbols show different phases as, □ for nematic, ▽ for isotropic, △ for columnar, ◇ for tilted and ● for Discotic-Smectic phase.

We were able to characterize this phase using parallel and perpendicular distribution functions, showing the layering of the system as can be observed in figure, with a periodicity similar to the thickness of the particles. Meanwhile, there is no evidence of columns (see fig.3.13).

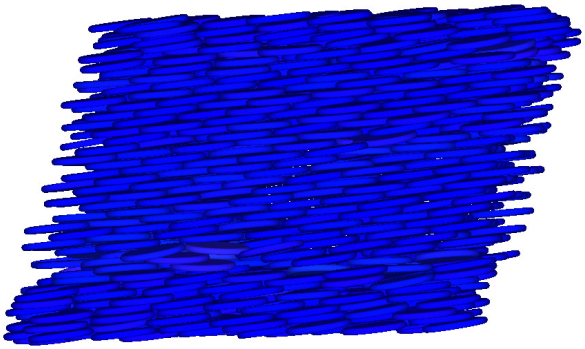

Figure 3.12: Snapshot of a discotic Discotic-Smectic configuration obtained under the chosen potential U_E at $T = 2.5$ and $P = 88$, where we can observe the layers disposition of oblate spherocylinders (colours depicting particles orientations).

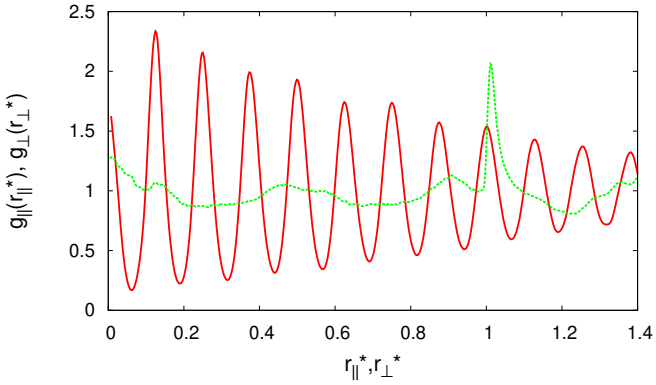

Figure 3.13: Parallel and perpendicular distribution functions of the system for the chosen potential U_E at $T = 2.5$ and $P = 88$. Displayed in red solid and green dashed lines respectively.

The effect of the U_T type potential at medium temperatures was the absence of the columnar phase. This shocking feature is shared with isotherm simulated at medium temperature for the U_C type potential. In both cases it seems that columns break in order to minimize the energy adopting the more convenient orientation according to each type of potential. For the case of U_T at lower temperatures this means the formation of the Uniaxial phase, where persistent chunks of columns are stably trapped by the surrounding particles in a T orientation. This yields a population of particles sharing a common orientation and another one which takes any of he perpendicular ones(see fig.3.15).

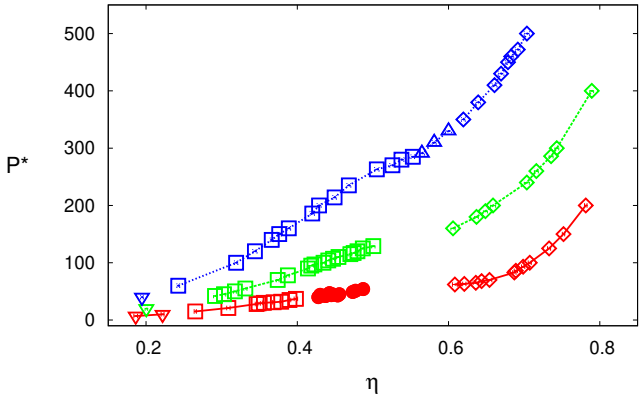

Figure 3.14: Isotherms of the U_T type potential with parameters, $\kappa = 0.10$, $\kappa' = 1.90$,$\nu = -0.40$ and $\mu = -0.10$, showing pressure P^* in reduced units as a function of packing fraction η at temperatures T=0.875, T=1.75 and T=3.50 in solid (red), dashed (green) and dotted (blue) lines respectively. (error bars within the points size). Where symbols show different phases as, □ for nematic, ▽ for isotropic, △ for columnar, ◇ for tilted and ● for Uniaxial phase.

In the case of the U_C type potential, particles in the tilted phase are close to the C canonical orientation. This is responsible for the unexpected low packings

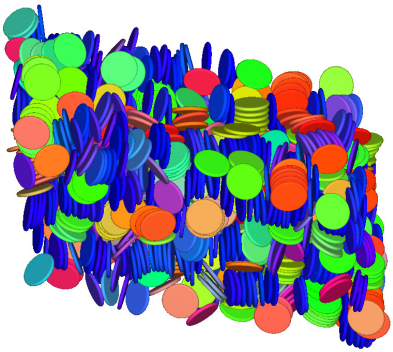

Figure 3.15: Snapshot of a Uniaxial configuration obtained under the chosen potential U_T at $T = 0.875$ and $P = 43$, where we can observe how some columnar clusters are trapped oriented in the same direction while others lay in any possible disposition favouring T canonical orientation around them (colours depicting particles orientations).

and high temperatures to which it remains stable and also for the afore mentioned lacking of columnar phase at medium temperatures. At low temperatures this drives to the formation of the Cubatic phase, where column chunks of almost cubic proportions are reoriented to minimize the energy of the system (see fig.3.17).

We were able to characterize the Uniaxial and Cubatic phases through the analysis of the orientational distribution function ($g_2(r)$) between the centres of particles. This is plotted in figure 3.18 where we can observe that distinctive features of the parameter appear at distance of 1 diameter in the Cubatic phase and at distance of 0.6 for the Uniaxial phase. For the sets of parameters studied, the Cubatic phase has a density of around 6.9+- particles per volume unit, meanwhile the Uniaxial has 6.0+-. This difference in density provides some clues about the behaviour of $g_2(r^*)$ from $r^* = 0.5$ to $r^* = r_c^*$ (cut-off distance of the

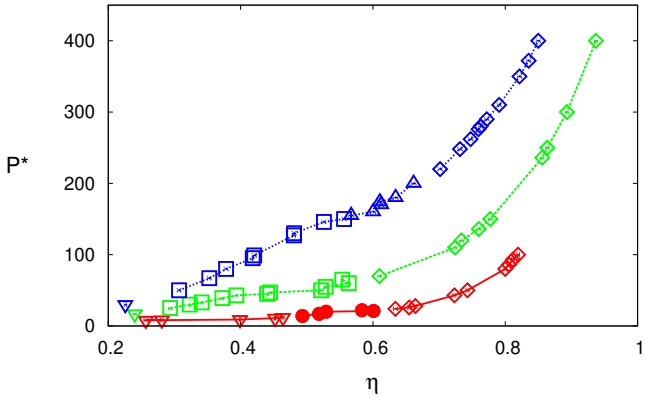

Figure 3.16: Isotherms of the U_C type potential with parameters, $\kappa = 0.10$, $\kappa' = 0.10$,$\nu = -1.30$ and $\mu = 0.30$, showing pressure P^* in reduced units as a function of packing fraction η at temperatures T=0.50, T=1.00 and T=2.00 in solid (red), dashed (green) and dotted (blue) lines respectively. (error bars within the points size). Where symbols show different phases as, □ for nematic, ▽ for isotropic, △ for columnar, ◇ for tilted and ● for Cubatic phase.

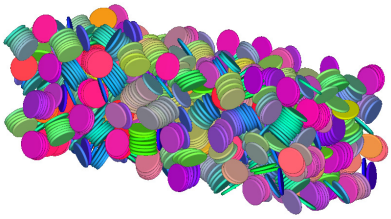

Figure 3.17: Snapshot of a Cubatic configuration obtained under the chosen potential U_C at $T = 0.5$ and $P = 17$, where we can observe how columnar clusters of roughly cubic proportions tend to be at positions which maximize the number of particles in C canonical orientation (colours depicting particles orientations).

potential$r_c^* = 1 + 3a_o$), because it means bigger columnar chunks and/or better packaged for the Cubatic phase case. Causing the $g_2(r)$ to become negative at $r^* = 1$ due to the big population of particles perpendicularly oriented. One may wonder why the nematic parameter behaves differently in the Uniaxial phase, until we understand that their columnar chunks are smaller and/or loosely packaged, causing the average population of particles from $r^* = 0.6$ and further to be randomly oriented. Another reason that supports this is purely geometric since one oblate particle can be at potential reach of more particles in C than in T configuration.

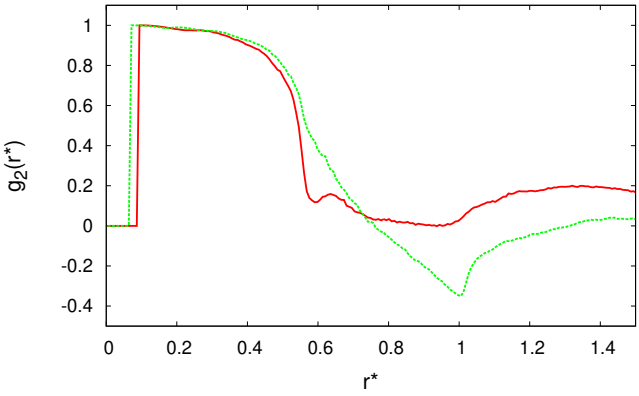

Figure 3.18: Orientational distribution function $g_2(r*)$, represented by a green dashed line for the Cubatic phase and red solid line for the Uniaxial phase.In the chosen potentials U_C at $T = 0.5$ and $P = 17$ and U_T at $T = 0.875$ and $P = 43$ respectively.

3.5 Conclusions

After a thorough exploration of the space of parameters applicable to the OGBK model a classification of the main possible outcomes is proposed, regarding the expected self-assembled structures that may arise from the F, E, T and C potential types (obviating some intermediate situations). After that, some simulations were performed to test the hypothesized favoured ordering. Finding that, at high temperatures the phases of hard spherocylinders [121] for the shape anysotropy simulated $a_o = 0.1$ were found (in increasing packing fraction order; isotropic, nematic, columnar and tilted phase). However, at low temperatures, as soon as the pressure is low enough the minimization of energy takes over reorienting particles into the most stable configurations.

An Discotic-Smectic phase was stabilized for oblates under the E type potential at packing fractions between the columnar phase and the nematic phase. A Cubatic phase was found to be stable under the C type potential between the isotropic and tilted phases, substituting the columnar and nematic ones. And finally a Uniaxial phase was stabilized for the T type potential substituting in this case the columnar phase.

All in all, this results allows us to think that anisotropic interactions in oblate particles can be used to tailor the appearance of new phases with interesting structural features under specific thermodynamic conditions. Likewise, supports the usage of the OGBK potentials to be used as a model for many different types of systems.

Chapter 4

Clusters formation with directional pair interactions

When a colloidal suspension is cooled, particles can easily be attached to each other by Coulombic or Van der Waals forces. As we will see, depending on how this cooling is performed and some intrinsic characteristics of the system, the attachment can happen on early collisions or delay some time, resulting in different type of aggregates and subsequent structures. This often means a fall into a glass phase The glassy behavior in soft matter has been studied for many decades through theory and experiments, but it is far to be completely understood. Despite the effort of many researchers during this time some phenomena are still elusive to our understanding. This is usually due to the time scales and non-ergodicity of the systems [122, 123]. A lot of effort has been put to ponder the influence of thermodynamic and kinetic factors into the gelation phenomena analysing different scenarios such as, phase separation [124–126], dynamical arrest [127] percolation [122, 125] or even jamming [128]. All this gets even

more complex if we try to analyse the interplay of shape, flexibility and interactions of its constituents. These features are easily tunable by present colloidal science opening new and interesting opportunities to research and technological development, attracting more interest every day.

Glasses even when made of purely passive elements are in a non-equilibrium state, and the transition of a liquid into a glassy state is a fall into a non-ergodic situation, this fact plays an important part in the evolution followed when a liquid is quenched into a glassy state. Usually referred to as ”aging”, this process may have many causes and outcomes depending on the system under research [123]. This is mostly due to the different regions of the energy landscapes accessible to every system according to its temperature and previous history. In figure 4.1 we can observe an intuitive representation of that idea, with two-dimensional representations of the energy and packing fraction of an imaginary system as functions of the configuration coordinates. Seeing this we can picture how a system can be trapped into a metastable state depending on the thermodynamic paths available to it, regarding its temperature and initial structure.

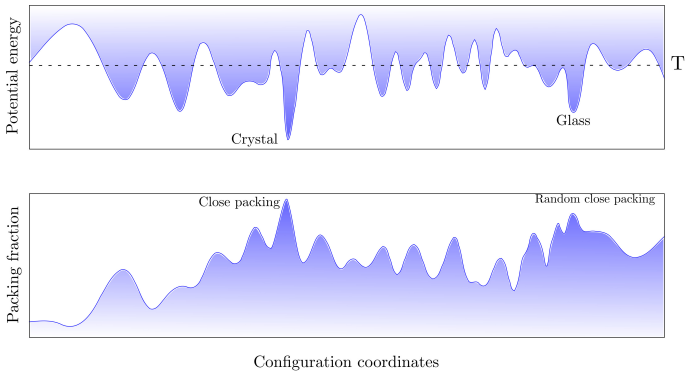

Figure 4.1: Two dimensional projection of an imaginary landscape of configurations.

This study aims to shed some light on the phenomena of aggregation and subsequent aging. Therefore, to track the time evolution of some observables, this project will be carried out making use of Brownian Dynamics, performing an exploration in density and temperature observing its influence on the different paths and outcomes for several systems.

4.1 Methods and tools

This chapter tries to reveal how the directional anisotropy of the interaction potential affects the aggregation dynamics using oblate spherocylinders with the same anisotropy, $a_o = 0.2$ as defined in section 1.2.1. With this purpose we employ the OGBK potential thoroughly described in chapter 3 with three different sets of parameters. Following the same the notation , one would be F type ($\kappa = 5$, $\nu = 1$, $\mu = 1$), another E type ($\kappa = 0.1$, $\nu = 1$, $\mu = 1$) and the last of Kihara type ($\kappa = 1$, $\nu = 0$, $\mu = 0$) where the Gay-Berne factor is reduced to 1, leaving the potential homogeneous. We will refer to them as F, E and K along this chapter for convenience. The dependence of this potential with the minimum distance in the four canonical configurations used as reference in chapter 2 are plotted for the three potentials in figure 4.2. The reduced units in this study are the same of chapter 2 (See section 2.1).

A tool of choice to simulate colloidal particles is usually Brownian Dynamics (see section1.2.4). This technique allows applying very simple models and very good characterization techniques, this work is particularly dedicated to investigate, low density states for three model potentials (F, E and K). To this end, long BD simulations in the NVT ensemble were performed in a density range from 0.01 to 0.5 ρ^* for each potential, at specific temperatures quenching from temperatures of last fluid state found, we refer to it as T_f^*. To speed up the search of the last fluid point was made monitoring the energy of the systems in

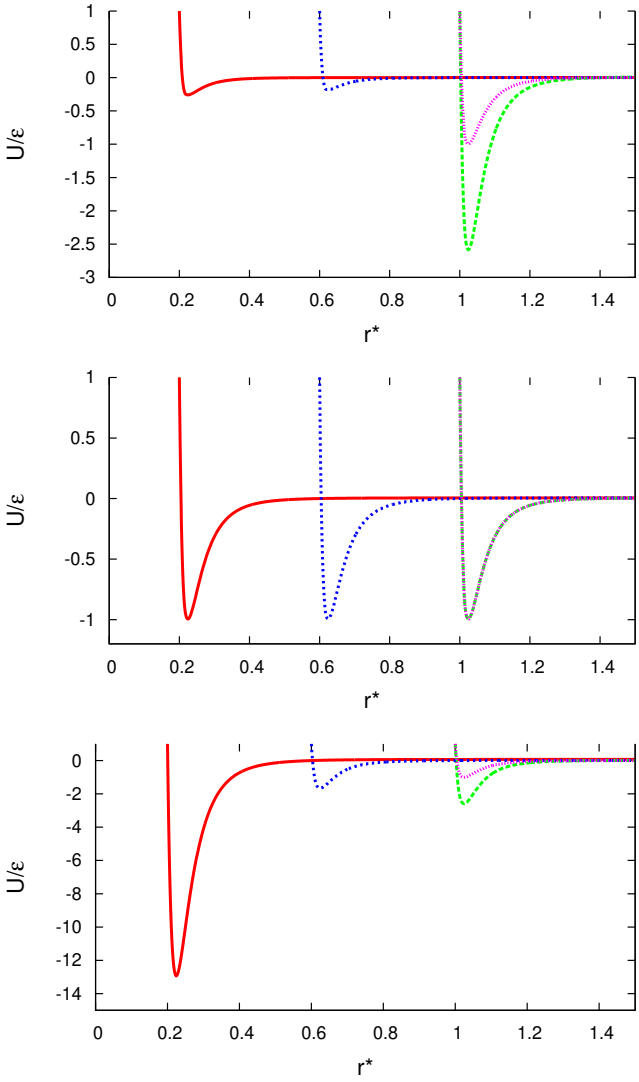

Figure 4.2: Interaction Energy in each of the four canonical configurations for the E, K and F potentials from top to bottom panels respectively. Where configurations F, E, T, C in red solid, green long dashed, blue short dashed and pink doted lines respectively.

MC simulations of constant number of particles $N = 1260$ and volume, since in this way the phase space is better sampled. After this first temperature where the system in not exclusively composed of monomers and dimers (T_c^*) is located by chenking the cluster distribution. This distribution is constructed accounting for a connection when two particles are closer than $d_m = 0.3\sigma$ what coincides with the potential cut-off. Then, the study of dynamic observables was performed at 1.0, 0.95, 0.8 0.5 0.1 times T_c^* for each density under study. BD simulations were performed quenching from T_f^*, starting from an equilibrated isotropic configuration of $N = 1260$ particles. At each temperature structural observables were computed using time intervals in a rather logarithmic scale in $t^* = t/\tau$, where $\tau = \sigma^3\mu_s/k_BT$, where μ_s is the solvent viscosity and σ is the system's length unit. The time step has been set in the range $10^{-4} < t/\tau < 2\cdot 10^{-3}$. In the following, unless said differently, when two features are showed together, they are compared at the least common maximum $t^* = 815$ in the case of dynamical observables, averaged over 100 independent time origins. Meanwhile, last configurations obtained in each case are displayed the individual maximum t^* achieved after 6 months of CPU time.

4.1.1 Aggregation model

To understand the aggregation process a very simplified model was applied using the above defined connection criterion. In it every cluster, dimer or monomer count as a single individual, for which the same average aggregation k_i and dissociation k_{-i} rate are associated. Therefore, the time evolution of the number of individuals N_i can be expressed as:

$$\frac{dN_i}{dt} = -k_i N_i^2 + k_{-i} N_i \tag{4.1}$$

At low enough temperatures it is assumed that $k_i >> k_{-i}$, hence given an initial number of particles N_0, the evolution of the number of individuals over

time is approximately described by the following equation:

$$\frac{N_0}{N_i} = N_0 k_i t \tag{4.2}$$

During the simulations, the cluster formation was monitored with the observable Θ, to analyse the aggregation dynamics of the studied states, it was needed an easy to understand or easy to compute magnitude able to indicate the collapse of the system. In their work of 2013 Mognetti et al. [129], find correlation between intrinsic magnitudes of the systems in his study and the following definition of the degree of clusterization:

$$\Theta = 1 - \frac{\langle N_{clusters} \rangle}{N_{particles}} \tag{4.3}$$

Where $\langle N_{clusters} \rangle$ is the average number of clusters and $N_{particles}$ the total number of particles in the system. Thus, when the system is in the dilute gas phase where $\Theta = 0$ and when all particles belong to the same cluster $\Theta = 1$.

The value of Θ can be fitted over time with the previous equation taking $k = N_0 * k_i$ as:

$$\frac{1}{1-\Theta} = \frac{N_0}{N_i} = kt \tag{4.4}$$

As an example in figure 4.6 are the values of $1/1-\Theta$ as a function of time, and its fits for the temperatures studied at $\rho = 2$ for the K potential.This can in turn be adjusted in an Arrhenius model like:

$$k = A \cdot \exp(\frac{E_a}{\kappa_B T}) \tag{4.5}$$

Where T is the temperature, E_a the activation energy in this model and A is a constant related to the frequency of collisions in the correct orientation, what

in our case would mean for the cases of OGBK model, in E or F configurations for E and F potentials respectively.

4.2 State diagrams

Applying the model described in section 4.1.1, checking the differences in E_a, we have been able to discern two different regimes of aggregation with similar features for every potential studied. These regions are outlined in state diagrams displayed in figures 4.3, 4.4 and 4.5 for potentials E, F and K respectively. From those we have to stress that those are not phase diagrams, but rather out-equilibrium maps. In them we can observe at the densities studied the last temperature where the system remains fluid and below it the first with persistent clusters. Right below this point we find the slow aggregation region (R_s) where the nucleation events are rather uncommon and the size of clusters appears to be bigger. And finally, below it, the fast aggregation region (R_f) with opposite features to R_s quickly forming small aggregates that depending on the density of the system can either diffuse, bond or arrest forming a meta-structure. The existence of this two regimes for attractive colloids is known from long ago [130, 131] traditionally referred to as diffusion limited aggregation (DLA) and reaction limited aggregation (RLA) [126]. The details on the dynamics of the particles and the structures formed under each potential depict an interesting map of different non-equilibrium states, where we can find a unique or multiple clusters either being the only phase present or in coexistence with monomers, or the very interesting case of a unique meta structure. In every case with differential characteristics for each potential. When temperatures are close to the fluid region (R_s) the collision rates are higher and the size of the clusters formed increases with density. But at low temperatures (R_f) the collisions are less frequent but the E_a increases abruptly, feeding the formation of a bigger number of

smaller clusters. The collision rates are also bigger if the system is denser, as the evolution of the constant A at low temperatures suggest (See fig.4.6). This, in turn results in the formation of different long range structures depending on the potential applied as we will see in section 4.4.

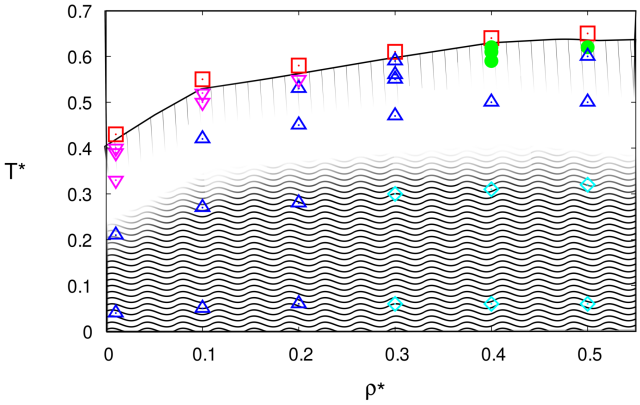

Figure 4.3: Non-equilibrium diagram of the E potential, where, different aggregation regimes are shown with straight (R_s) or wavy (R_f) lines background. And symbols show different states as,□ Fluid, ● unique cluster, △ multiple clusters, ▽ monomers and clusters coexistence , ◇ unique meta structure. More detail in text.

The different states found are in concordance with the ones found in experiments of attractive glasses and gels [123, 132], as will be later discussed, leaving aside the peculiarities of the potential implemented. One small caveat worth to mention is that these simulations have no gravity field applied, and this may explain why we do have coexistence instead of phase separation of colloids and aggregates [125].

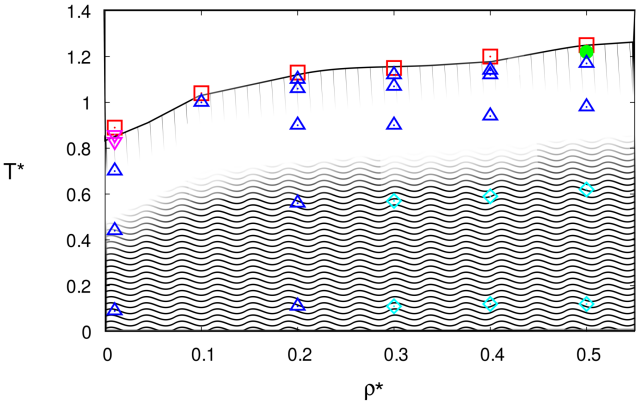

Figure 4.4: Non-equilibrium diagram of the F potential, where, different aggregation regimes are shown with straight (R_s) or wavy(R_f) lines background. And symbols show different states as,□ Fluid, ● unique cluster, △ multiple clusters, ▽ monomers and clusters coexistence , ◇ unique meta structure. More detail in text.

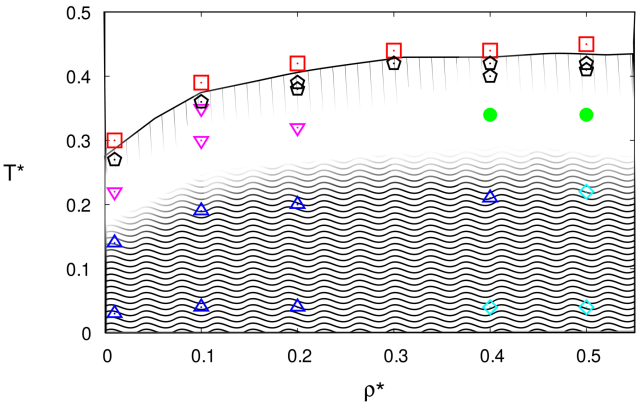

Figure 4.5: Non-equilibrium diagram of the E potential, where, different aggregation regimes are shown with straight (R_s) or wavy(R_f) lines background. And symbols show different states as,□ Fluid, ● unique cluster, △ multiple clusters, ▽ monomers and clusters coexistence , ⬠transient clusters, ◇ unique meta structure. More detail in text.

4.3 The aggregation model at work

The fitting of k at temperatures close to the fluid region can be misleading due to its steepness in the early stages of the cluster formation, as can be seen in figure 4.6 where for each temperature the evolution of the number of clusters is fitted to k as defined in section 4.1.1. This leads to big uncertainties displayed in some points with big error bars in figure 4.7 where the k fitted for each point is plotted using $\ln(k)$ as a function of $1/T^*$, to obtain the E_a in each range of temperatures. However, in general, this simplified aggregation model seems good enough to obtain very relevant information from the systems.

In figure 4.7 can be observed two different aggregation regimes for every studied density of the K potential, characterized by an abrupt change in E_a. This featured is observed in the same fashion for the cases of potentials E and F, but given the small number of sampled temperatures in each case, neither the E_a nor the exact temperature for the regime transition could be precisely determined. Nevertheless, in figures 4.3, 4.4, 4.5, this two regions of the state diagrams are marked using different backgrounds. In the case of the E_a it is to be remarked a difference of roughly two orders of magnitude between the value it takes in each regime.

Meanwhile at low temperature figure 4.7 is enough to argument that collisions in correct orientation increases at higher densities since the constant A does the same (See eq. (4.5)) . The behaviour of the aggregation rates at different densities can be clarified at temperatures close to fluid region. With this purpose, we track in time, the evolution of populations of monomers, dimers and bigger clusters separately. In figure 4.8 we can observe precisely this for each potential comparing $\rho^* = 0.1$ and $\rho^* = 0.5$ at the temperatures studied just below the fluid region. If particles find each other at distances shorter than the cut-off of the potential, their interaction may result in aggregation with high

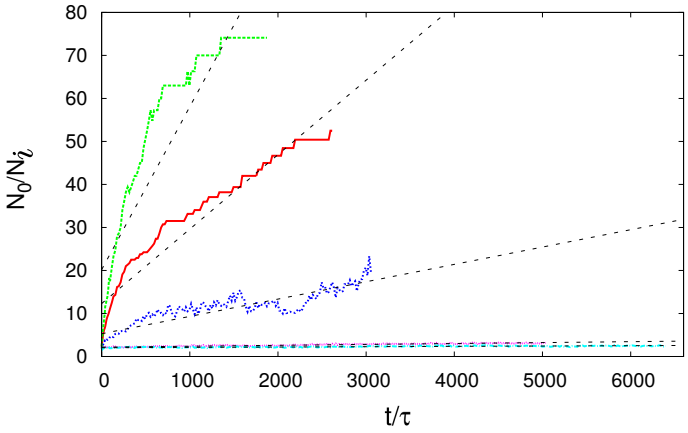

Figure 4.6: Fitting of the aggregation rate constant k at density $\rho^* = 0.2$ for the K potential at temperatures $T^*/T_c^* = 0.1$, 0.6, 0.8, 0.95 and 1.0, in red solid, green long dashed, blue short dashed, pink doted and cyan dashed doted lines respectively. With the nearest black long dashed spaced line near to them being their fitted line.

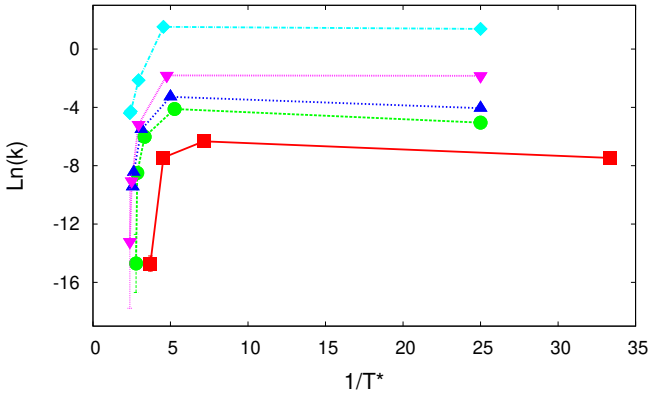

Figure 4.7: Plot of $\ln(k)$ vs $(1/T^*)$ for the K potential at densities $\rho* = 0.01$, 0.1, 0.2, 0.4 and 0.5 in red solid, green long dashed, blue short dashed, pink doted and cyan dashed doted lines respectively. Where symbol are simulated temperatures and any plausible straight line drawn would have E_a as slope and A as cut with the Y-axis.

probability if they find each other in a convenient orientation. Oblate particles they have more probability to collide with rather parallel revolution axis, since these covers more solid angle. To these conditions we should add that depletion interactions [133–135] would favour the F orientation even if the potential is homogeneous in all orientations as the K is. This feature can be either promoted if we are modelling particles with the F potential as we saw in chapter 3, or in the case of the E potential weakened.

The described behaviour have profound repercussions from the early stages of the quenching applied, even with this little change in temperature. As we can see in figure 4.8, almost instantly nearly 20% of the system form dimers at low densities and stays rather stable but at low densities rapidly decrease in favor of bigger clusters, except in the case of the E potential where that seems to take longer. At density $\rho^* = 0.5$ cluster fraction quickly overcomes dimers and monomers for the three potentials. As we will se in section 4.4 the configuration obtained at maximum simulated time, both E and T potential arrive to a single cluster with very defined short range structure meanwhile the K potential keeps a population of dimers and monomers. We can assume as a rule of thumb, that the F potential will always accelerate the formation of clusters meanwhile the E potential slows it down respect to the K potential. One may conclude that the K potential form clusters which loose and gain particles at high rates, so it is rather a fluid of transient clusters [123]

The dynamical information obtained at time $t^* = 815$ showed in section 4.3.1 would be incomplete not knowing where does the states come from, to this end was computed the value of Θ along the simulations to easily show the cluster proportion of the system. Observing figure 4.9 we can see that at high density $\rho^* = 0.4$ when Θ is first computed at $t = 1$ it shows values over 0.5 in all cases indicating an abrupt aggregation between the closest neighbours since the be-

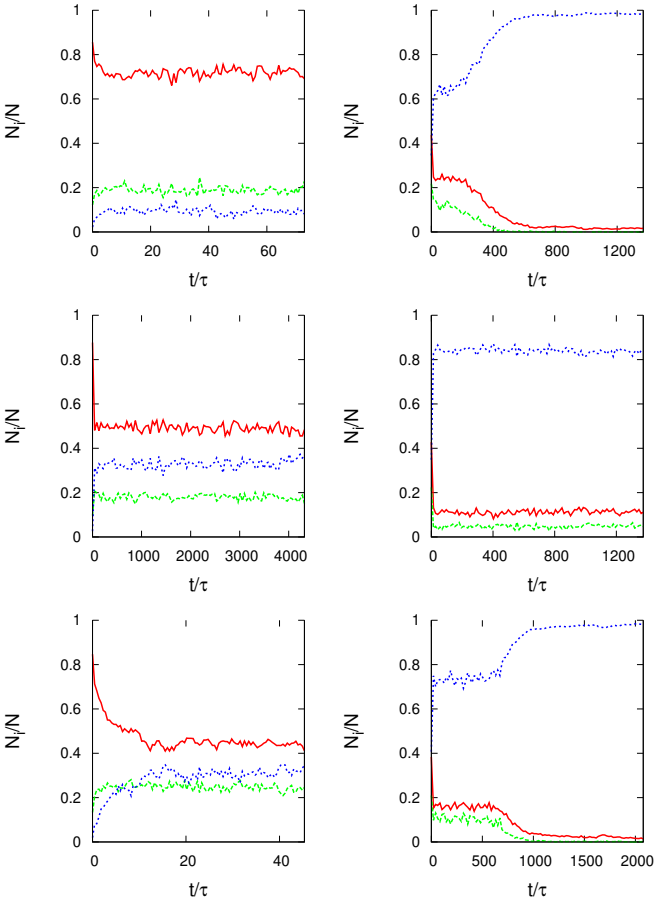

Figure 4.8: Fractions of the total number of particles which are monomers (red solid line), dimers (green long dashed line) and clusters of three or more particles (blue short dashed line) in the early stages of aggregation. Showed at $\rho* = 0.1$ and $\rho* = 0.5$ on left and right panels respectively for potentials E, K and F from top to bottom panels respectively at temperatures just below the fluid region (see figures 4.3, 4.5 and 4.4).

ginning. This behaviour becomes less significant at lower densities where the closest neighbours are further.

To compare the evolution of Θ in the different regimes, figure 4.9 shows it at temperatures $T^*/T_c^* = 0.1$ and 0.95 . If we focus on the low temperature (R_f) the number of clusters is quickly reduced, a feature which is fuelled at high densities by clusters closeness. In this sense, as we will see, the compactness of the clusters depends on the potential under study (increasing in order $E \to K \to F$ in our case). What is coherent with the delayed aggregation of the formed clusters. If we now pay attention the evolution of Θ which for the high temperature (R_s), displays faster aggregation in the also in increasing order $E \to K \to F$ as was supposed during the application of the aggregation model. The behaviour of Θ under the K potential in R_s is also coherent other results, that as we will see indicate a stable state where particles easily go in and out of big clusters.

4.3.1 Dynamics

The observables showed in this section were computed as averages over all particles, so we should take into account that the number and size of clusters and the particles that do not belong to any cluster can influence these calculations. Even if we are studying non-equilibrium systems, we expect to have a very stable situation after this long simulations, indeed there is no sign of abrupt transition in any case at $t^* = 815$. The most relevant result from the observations of the dynamics is that at temperatures just below T_f, the K potential still resembles a fluid when even the majority of the particles of the system form a cluster meanwhile in the E and F potentials, particles shows a subdiffusion typical of a gel [136], as can be seen in figure 4.10. This distinctive state is marked on figure 4.5 with black pentagons.

For the K potential at $\rho^* = 0.4$, and in the same range of temperatures, the

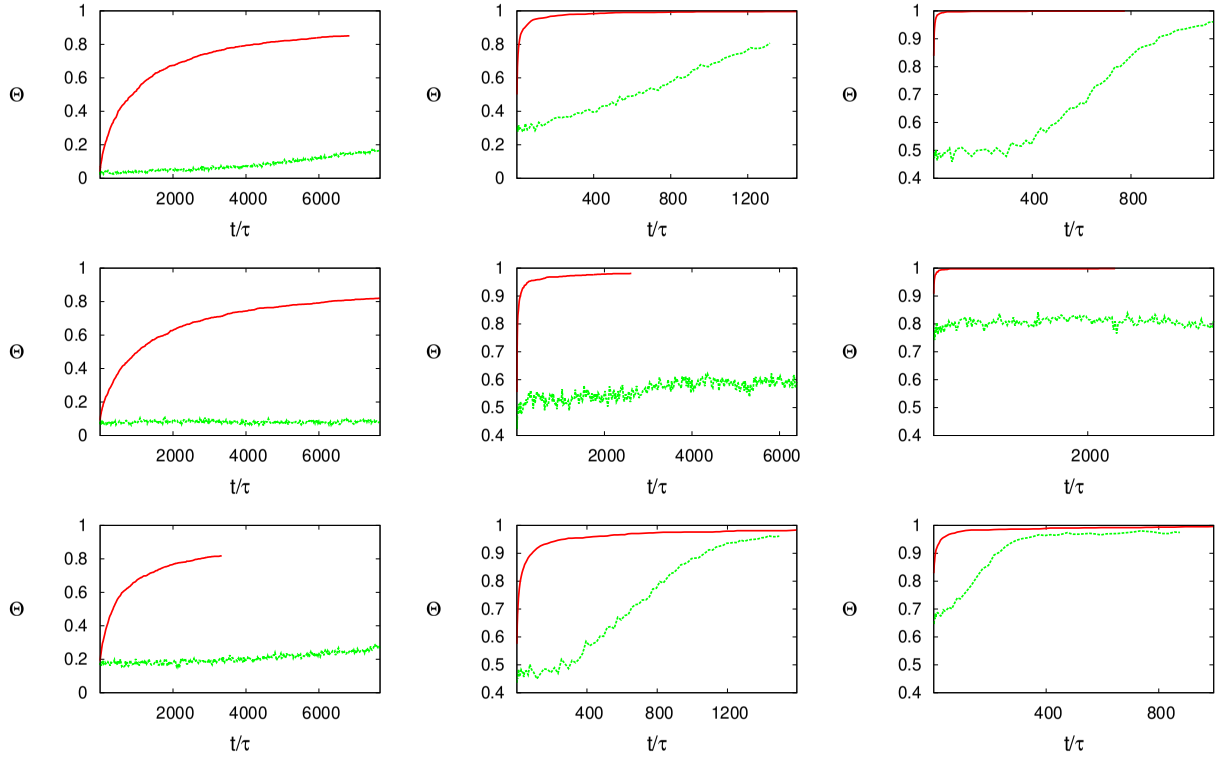

Figure 4.9: Θ of the systems over time,at densities $\rho* = 0.01$, 0.2 and 0.4 from left to right panels for potentials E,K and F from top to bottom panels respectively. At temperatures of $T^*/T_c^* = 0.1$ and 0.95 in red solid and green long dashed lines respectively

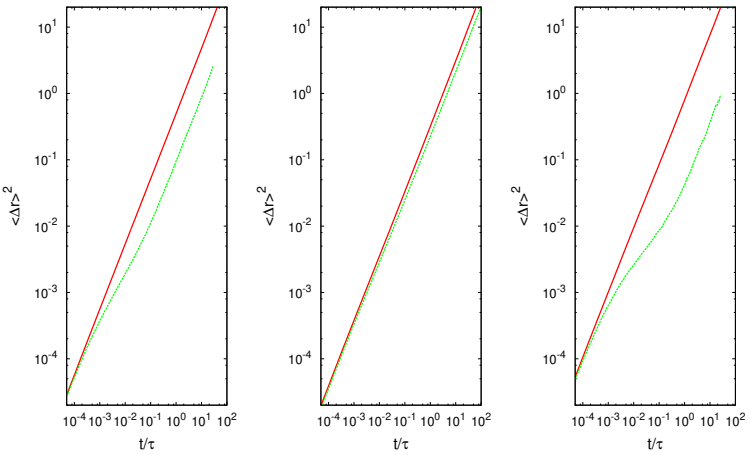

Figure 4.10: Mean squared displacement at $\rho^* = 0.4$ at T_f and the first below it, in red solid and green long dashed lines respectively, for potentials E, K and F from left to right panels respectively.

information obtained from the mean squared displacements (fig. 4.12) and from the self scattering function (ISF) in figure 4.11, are the two sides of the same coin which corroborates the differences between the two regimes. This to figures serve as an example of the common behaviour of the three potentials, featured by the existence of two different relaxation times, and a transition from a fluid to a very subdiffusive regime as the temperature is reduced. The $\chi_4(t)$ was also used to try to disentangle how the aggregates of each potential are reflected on the collective behaviours of the system, but unluckily this task seems to need more extensive simulations to decorrelate the effect of thermal history and the different orientations of the potentials, and the $\chi_4(t)$ is not showed here.

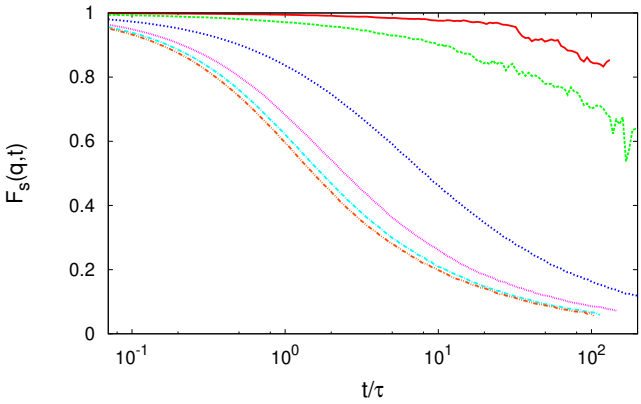

Figure 4.11: The self part of the intermediate scattering function (s-ISF) in the K potential at $\rho^* = 0.4$ and temperatures $T^*/T_c^* = 0.1$, 0.5, 0.8, 0.95 and T_f in red solid, green long dashed, blue short dashed, pink doted, cyan dashed doted and orange long dashed double doted lines respectively.

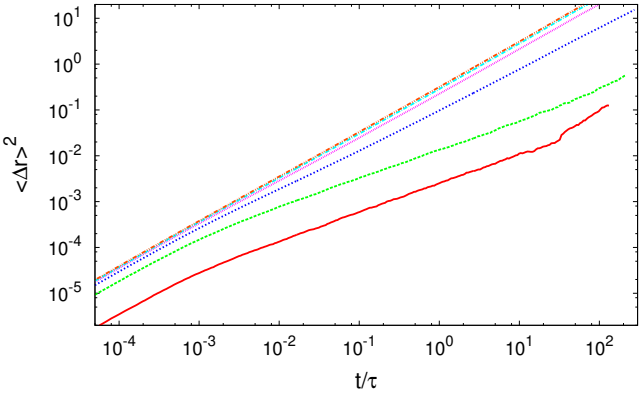

Figure 4.12: Mean squared displacements in the K potential at $\rho^* = 0.4$ and temperatures $T^*/T_c^* = 0.1$, 0.5, 0.8, 0.95 and T_f in red solid, green long dashed, blue short dashed, pink doted, cyan dashed doted and orange long dashed double doted lines respectively.

4.3.2 Structural Information

From chapter 3 we know that E and F potentials tend to form specific structures at low enough temperatures. To investigate the possible manifestations of this in the final states the radial distribution function is used inspect the clusters in the search for this kind of internal ordering, because this should leave a characteristic signature in it. To show, this $g(r)$ are plotted at different temperatures for an intermediate density of $\rho* = 0.2$ in figure 4.13, for the E, F and F potentials.

The E and the F potential both show many peaks at distances bigger than $r^* = 0.1$, in the case of the E potential the peaks ar signalling a layered structure meanwhile the peaks of the F seem to be signalling a columnar structure. In both cases the structures at distances bigger than $r^* = 0.1$ obtains preponderance as the temperature increases, what indicates bigger clusters. Is also remarkable how the peak at $r^* = 0.1$ for the F and the peak at $r^* = 0.1$ for E potentials are present with similar intensities at all temperatures indicating that even a heavy quench is not able to trap particles in rather random orientations.

For the Kihara potential we find a peak at low temperatures around 0.2 indicating that particles are attached in a F configuration and another peak at $r^* = 1.0$ indicating an E configuration. As the temperature increases this two peaks disappear indicating more randomly oriented configurations in more open structures.

In general if we observe the evolution of the structures with temperatures they seem coherent with a transition from DLCA to RLCA due to the range of the structures formed [137, 138].

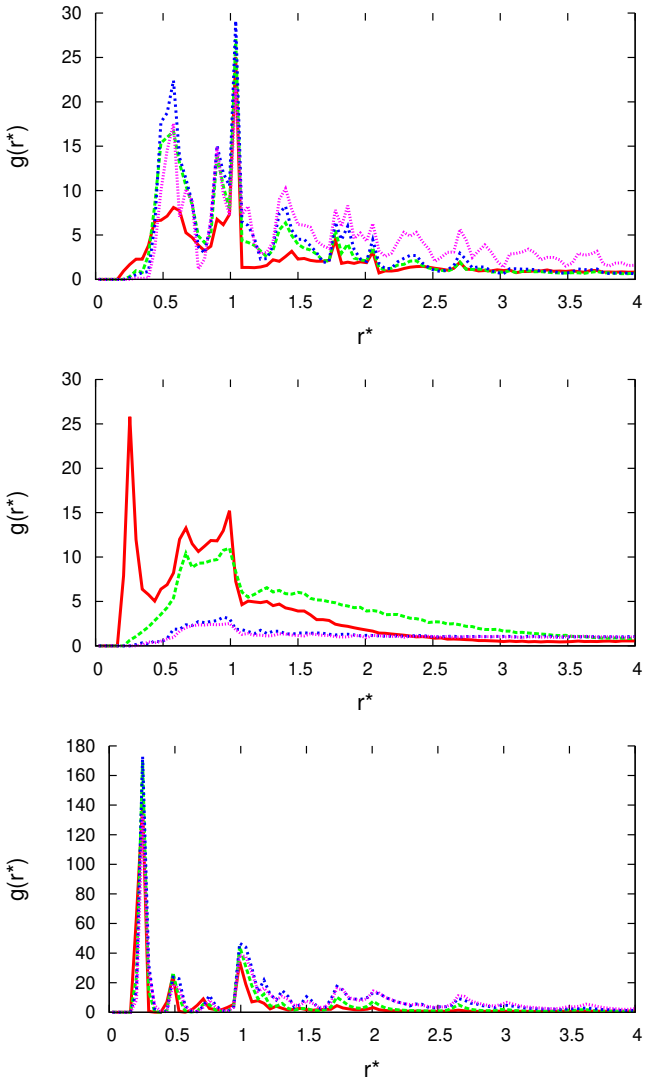

Figure 4.13: Radial distribution functions at $\rho* = 0.2$ for the E, K and F potentials from top to bottom panels respectively. Displaying temperatures of T^*/T_c^* = 1, 0.95, 0.5, 0.1 in red solid, green long dashed, blue short dashed and pink doted lines respectively.

4.4 Configurations

In figures 4.14, 4.15 and 4.16 we can observe snapshots of the last states achieved at the points marked with symbols in the state diagrams of potentials E,F and K (Figs, 4.3, 4.5, 4.4 respectively). In them, we can visually inspect the final structures after long aggregation processes and check that configurations observed are coherent with the obtained results. Even if the shape and internal ordering of the aggregates is different, the states with similar features are named the same. However, we can observe that the F potential tends to form highly compact clusters since, as we can see they are composed of columns. The E potential form lenticular clusters due to its tendency to align particles facing edges. And in the case of the K potential, the clusters lack of any internal producing rather spheric clusters.

It would be interesting to perform a more detailed study on the differences between the transitions from DLCA to RLCA [139] for the different potentials and densities since we observe that at very low densities $\rho* = 0.01$ there is a transition between similar states (coexistence of monomers and clusters and an apparent fluid of clusters) for the three potentials, but in denser systems the interactions start to play their part shaping clusters and meta-structures.

Snapshots from the states at the two higher temperatures from density $\rho* = 0.1$ upwards, for the K potential, displayed a state that to our analysis is indistinguishable from vapor-liquid coexistence [140, 141]. However, for equivalent temperatures in the E and F potentials it is showed a few clusters, without coexistence with monomers. These snapshots can be compared with asymptotic evolution of Θ for this temperatures in figure 4.9 and make us assume that any monomer displayed in the pictures in the cases of E and F potentials will become part of a cluster rather than coexist with them.

The multiple clusters regions showed in the snapshots for the three potentials

manifest different dynamic, structural and kinetic features, but even if they may look like a fluid of clusters, further investigation would be necessary to label them as it [142].

At temperatures $T^*/T_c^* = 0.80$ and below in all systems clusters seem to either aggregate or become arrested, therefore its size and shape plays a decisive role in the structures found. It seems that the compactness of the columnar clusters formed in the F potential help to form more open structures, meanwhile flat clusters of the F potential tend to align more reducing the space between them.

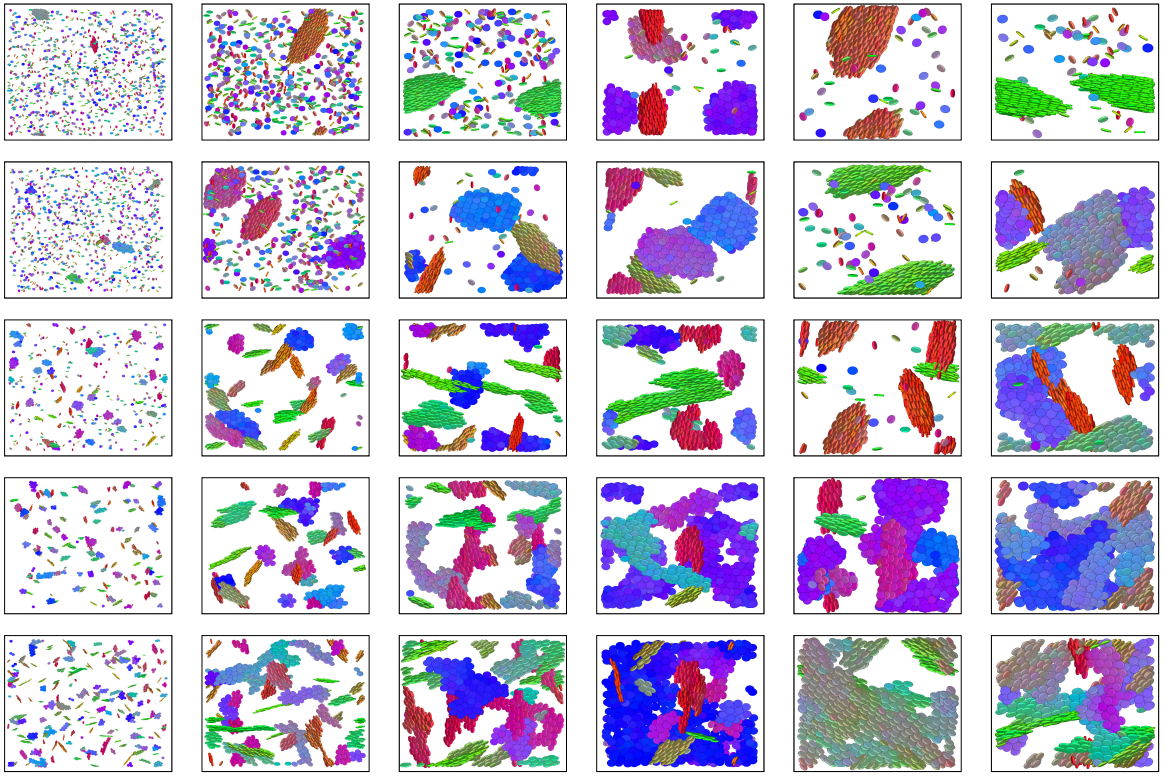

Figure 4.14: Snapshots of the final configurations obtained for the E potential at relevant states. From left to right, densities $\rho* = 0.01$, 0.1, 0.2, 0.4 and 0.5 from top to bottom temperatures $T^*/T_c^* = 1$, 0.95, 0.8, 0.5,0.1 (directions referenced from text orientation, and (colours depicting particles orientations)

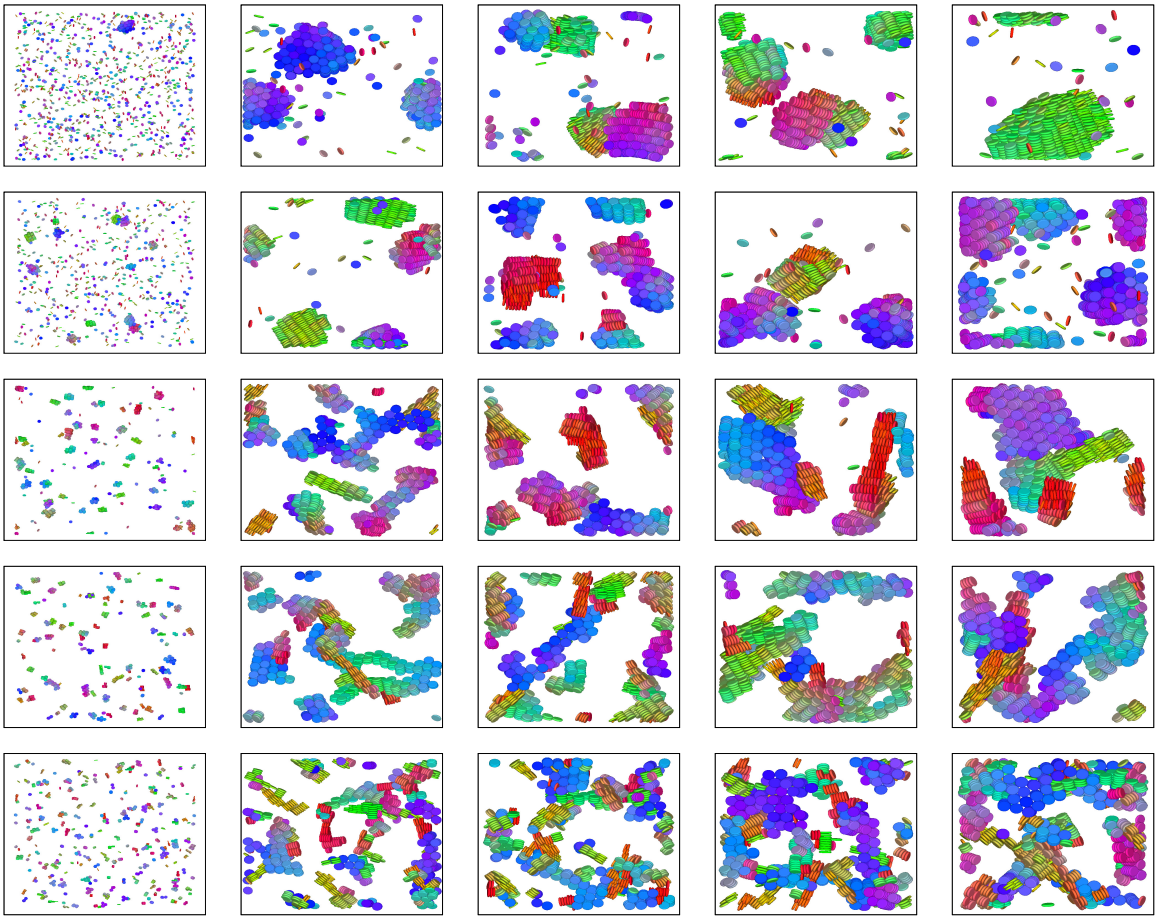

Figure 4.15: Snapshots of the final configurations obtained for the E potential at relevant states. From left to right, densities $\rho* = 0.01$, 0.2, 0.3, 0.4 and 0.5 from top to bottom temperatures $T^*/T_c^* = 1$, 0.95, 0.8, 0.5,0.1 (directions referenced from text orientation, and colours depicting particle orientations)

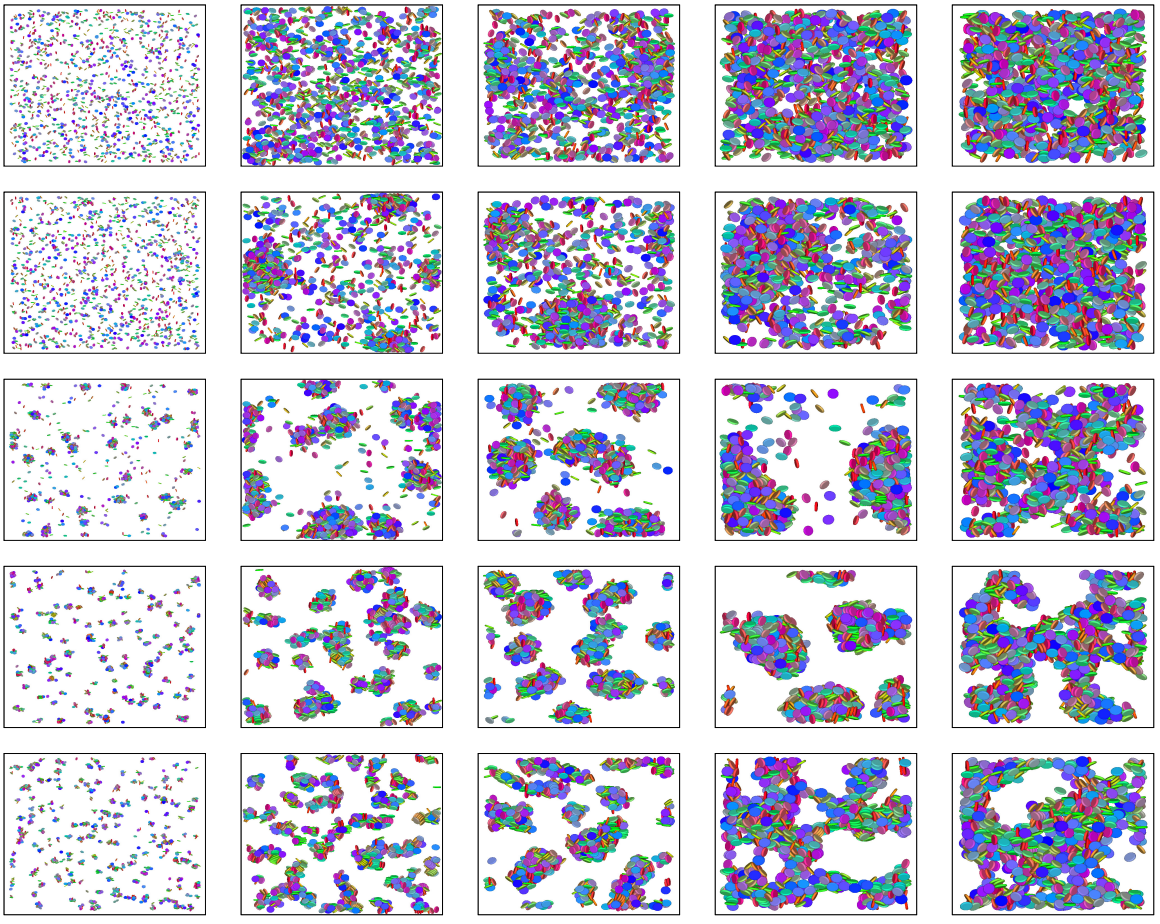

Figure 4.16: Snapshots of the final configurations obtained for the E potential at relevant states. From left to right, densities $\rho* = 0.01$,0.2,0.4 and 0,5 from top to bottom temperatures $T^*/T_c^* = 1$, 0.95, 0.8, 0.5 and 0.1 (directions referenced from text orientation, and colours depicting particle orientations)

4.5 Conclusions

In this work we compare three different potentials E, F and K, in the context of colloidal suspensions to gain some insight in the role played by anisotropic interaction potentials. In this chapter are investigated a rather wide range of densities, making in quenches at significant temperatures. On one hand this number of variables broadly explored, there can be found many similar features, as are the two regimes of aggregation, R_s where big clusters are slowly formed in cases of high densities easily integrating all particles in the system and R_f where small clusters are quickly formed and at high enough densities depending on the characteristic structure of the aggregates reaching percolation. Leaving aside the shape of the clusters, the estates found at $\rho^* = 0.01$ were qualitatively the same due to the low rate of collisions. On the other hand, the Arrhenius type aggregation model showed a direct correlation of the collision rate with the density, which would yield in a more effective aggregation in the case of the F potential than in the K, or less effective than the K for the E potential.

The radial distribution functions, are indubitable proof that, anisotropic interactions controls the internal structure and shape of the clusters, forming almost lenticular aggregates in the case of the E potential, columnar aggregates in the F potential and randomly oriented ones in the case of the K potential. However, its size and possible meta structures seem to rely on the thermodynamic history, specially we could check that deeper quenches yield smaller clusters.

The K potential showed a different behaviour just below the fluid region, compared to the E and F types, where the monomers tend to disappear. The K potential seems to achieve a coexistence of monomers and a unique cluster, to which the reversibly attach and detach, further research is needed to conclude if it is a vapour liquid coexistence [140, 141].

Chapter 5

Coarse grain model of a clay

Clays are present in many common products as paper, synthetic plastics or adhesives. Their applications are vast in number [143], from industrial drilling or surface coatings to drug delivery [144, 145]. Among them, the most common use is to control the rheological properties of consumer products, due to its rich behaviour in water and other fluids suspensions. This study is focused on the specific case of laponite [146], which is usually modelled as a thin disk of $1nm$ of height and $25nm$ of diameter, with its rim positively charged and its faces negatively charged (See figure 5.1). In laponite suspensions, salt concentration is used to control the formation of different phases, modulating the effective charge [147] as DLVO theory [148, 149] predicts.

The variance of the effective relative face to rim charge ratios is key to understand the formation of the different phases this substance can show [150], such as gels, repulsive and attractive glasses or Wigner glasses. The competition between short-range attraction and long-range repulsion has motivated several studies investigating how the charges in laponite surfaces affect its aggregation and phase behaviour [151–153], but its now clear that it is the patchy attractive

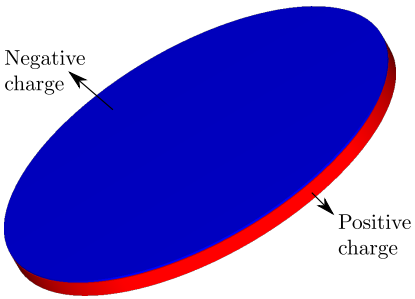

Figure 5.1: Laponite modelled as a cylinder of 1*nm* of height and 25*nm* of diameter, with its rim positively charged and its faces negatively charged

interactions, what controls the phase behavior and the long-term stability of the system [150].

To perform full atomistic MD simulations large enough in time and number of particles, to observe interesting results of multi-aggregate systems is out of reach for presently available computational facilities, therefore a coarse grain approach is needed. The attempt of Dijkstra *et al.* [106] to model laponite as an infinite thin disk with a quadrupole charge was enough to obtain the nanoporous structure known as "house of cards", and recently beads models [154, 155] have been successful in this aspect, arranging different charged spheres forming a flat disk shape. These models are easier to implement than effective pair interaction potentials, but more computationally expensive. Thus motivating the use of potentials like the Gay-Berne, as in these works of Ebrahimi *et al.* [156, 157] to fit it to atomistic simulations data. In this chapter the OGBK model explored in chapter 3 is extended to a laponite model, fitting its parameters to mimic the interactions that arise in this clay. With a functional form similar to others obtained with different approaches [158].

5.1 OGBK adapted to a clay

After a shallow observation of the interaction of Laponites, the attraction in a "T" configuration seems one of the most relevant features. This behaviour as we saw in chapter 3 can be achieved through many combinations of parameters of the OGBK model that satisfy the condition of having the global minimum in a "T" configuration.

In a first naive approach one can take the aspect ratio given by the manufacturer of this synthetic clays which is $L/D = 0.0368$ and look for a combination of parameters that has the global minimum in a "T" resulting "E","F" and "C" configurations much less attractive. This choice have a few caveats, the first one is that we can not avoid having a "C" configuration to be attractive and the second is inherent to the OGBK formulation since the set of parameters that allow for the "T" configuration to be the more attractive also implies the "E" to be less repulsive than the "C" which is rather unphysical. Therefore, to avoid this, the model was reformulated into a soft repulsive potential plus an attractive patchy for the "T" configuration. All this modulated by the Gay-Berne factor, keeping the Kihara approach to oblate particles. To explain it in a simpler manner, the previous Kihara formulation was separated into repulsive and attractive terms and the latter multiplied by Gaussian function with angular dependence in a similar approach to the ones of previous patchy models [159, 160]. If we take the revolution axis of two oblates $\mathbf{u_i}$,$\mathbf{u_j}$ and the normalized vector pointing from one centre to the other $\mathbf{r}$ due to particle symmetry, allows us to calculate the angles they form without any loss of information and operate with them in the following way:

$$\begin{aligned} a_{ij} &= \arccos(\mathbf{u_i}\mathbf{u_i}) - \pi/2 \\ a_{ir,jr} &= \arccos(|\mathbf{u_i}\mathbf{r}|) + \arccos(|\mathbf{u_j}\mathbf{r}|) - \pi/2 \end{aligned} \tag{5.1}$$

Those angles are used as arguments for a Gaussian function, which takes values

of one for "T" configurations and zero for any other:

$$P(a_{ij}, a_{ir,jr}) = \frac{[\exp(-\frac{a_{ij}{}^2}{\sigma_P}) - W] \cdot [\exp(-\frac{a_{ir,jr}{}^2}{\sigma_P}) - W]}{[1-W]^2} \tag{5.2}$$

Where $W = exp(-[\pi/2]^2/\sigma_P)$ plays the role of a normalization constant and σ_P gives us a measure of the angular width of the patch. For our purpose it was related to the aspect ratio of the oblates (see section 1.2.1) in the following way:

$$\sigma_P = 2\left[\arctan\left(\frac{\sigma}{L}\right)\right]^2 \tag{5.3}$$

Now the final expression for the potential is:

$$E_{OGBPK} = \varepsilon_{GB}\left[(\sigma/d_m)^{12} - (\sigma/d_m)^6 \cdot P(a_{ij}, a_{ir,jr})\right] \tag{5.4}$$

This is modulated as before by the Gay-Berne factor resulting in a oblate Gay-Berne Patched Kihara (OGBPK) potential. And finally it is truncated and shifted at $d_m = 3\sigma$ to make it continuous.

Now we are ready to set the parameters needed to provide the desired relative anysotropic interactions. To do, so we pick now the set of parameters $\kappa = 9$, $\nu = 1.9$ and $\mu = 0.2$, selected after filtering the data obtained from a similar exploration of parameters in the same ranges as the one performed in section 3.1, to meet the needs of this study. This set of parameters produce what we will call from now on P potential, which provide a ratio of -1.15 (negative sign due to opposite sign of energy) between the energy in F configuration at distance $r^* = 0.24$ (positive) and the minimum energy in the T configuration at $a_o = 0.15$ (negative). Which is as close as we can get to the given by Odriozola *et al.* [158] -1.23 for an average superficial charge. After that we only need to scale the temperatures to have a "T" configuration well of identical depth to any one we

desire. Meanwhile, other angular configurations are now repulsive and therefore at least qualitatively similar to laponite. But even after temperature scaling the potential shape are far from previous models accounting for interactions with ionized media (See fig.5.3). In those models [158, 161] repulsions appear to be softer and attractions, resulting in wider potential wells. In the OGBK model this is controlled by the aspect ratio, therefore to obtain functional shapes similar to previous models, we need to simply increase the anisotropy up to $a_o = 0.15$. A comparison of the same potential for the two anisotropies is displayed in figure 5.2, where we can see the potential energy as a function of the separation of the particles in the four canonical orientations, in it we can observe that repulsions also become softer. This motivates us to pick this anisotropy to run the simulations of the study.

To compare the data from Odriozola *et al.* [158] to the shape of the P potential we plotted figure 5.3 where we can observe that the increase in aspect ratio also displaces the location of the minimum. Nevertheless, if we displace the curve back exactly half the difference of the aspect ratios $((0.15 - 0.0368)/2)$ we observe a good overlap of simulation data and our functional form. Being this just a graphical check, not implying that the potential used in our simulations is corrected in that way.

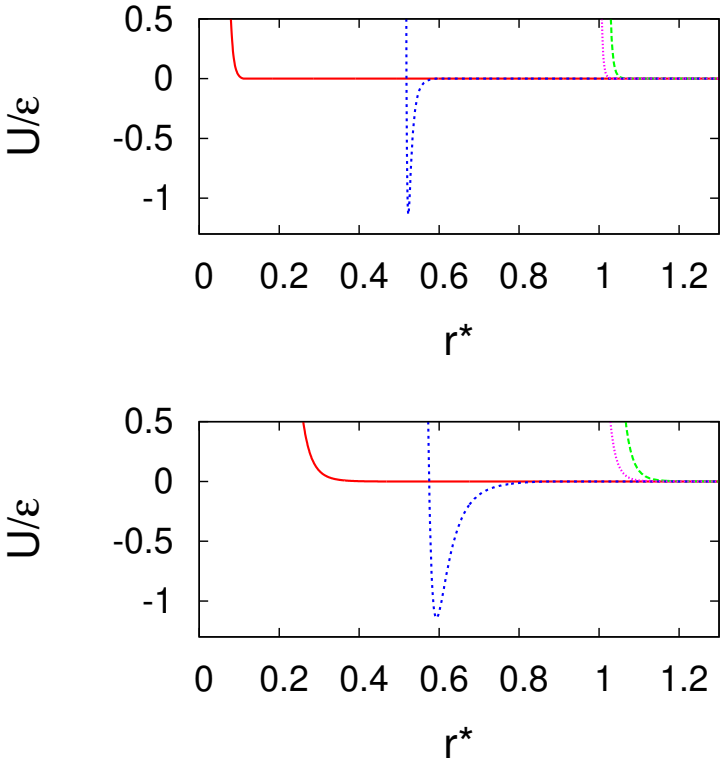

Figure 5.2: Patched type potential with parameters, ($\kappa = 9$), ($\nu = 1.9$), ($\mu = 0.2$) with shape anisotropy $a_o = 0.0368$ and $a_o = 0.15$ in top and bottom panels respectively. The configurations F, E, T, C in red solid, green long dashed, blue short dashed and pink doted lines respectively.

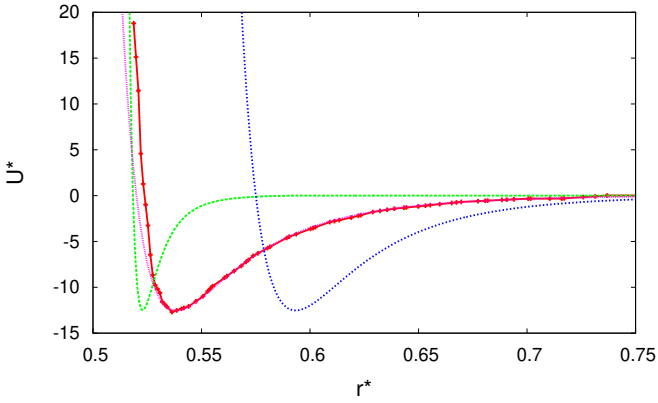

Figure 5.3: Detail of potential energy ($U^* = 10.96331 \times U/\varepsilon$) in the T configuration for the P potential for oblates of $a_o = 0.0368$ in green long dashed line, of $a_o = 0.15$ in blue short dashed line and this same curve displaced $-(0.15 - 0.0368)/2)$ in pink doted line. Red solid line are simulation results from [158].

5.2 Simulations details

Simulations at constant number of particles $N = 990$, were performed in the Isotension-Isothermal ensemble to check that particles under this potential behave as expected. From results of chapter 3 we know that the phases to be found at high enough temperatures would be similar to those found for hard oblates [121] of the same ratio which in this case ($a_o = 0.15$) yields isotropic, columnar and tilted phase. To roughly map the location of these phases isotherms lowering pressure at temperatures of 3.42, 3.0, 2.5, 2.0, 1.5, 1.0 ,0.8, 0.6, 0.38 and 0.2 T^*, where $T^* = T/\varepsilon$, starting from a tilted configuration (as a sanity check at the same pressures in $T^* = 3.42$, simulations starting from a columnar phase were run, arriving to the same phases). After a maximum of 8×10^5cycles to reach equilibrium in terms of energy and nematic order parameter, this states (from points in figure 5.4) showed stability during 8×10^5 cycles more. Where a cycle means N trials to move a particle (translate or rotate it) randomly chosen, with probability $(1/N)$ of this move to become instead a trial to change the shape of the simulation box.

5.3 Results

The phases found at high temperatures meet our expectations displaying isotropic, columnar and tilted phases (fig.5.4). But this results have a drawback when we aim to reproduce the phase behaviour of laponites since a nematic phase [162] should appear at intermediate packing fractions between the isotropic and the columnar regions. Absent in this case due to the employed anisotropy a_o.

Meanwhile at low temperatures in figure 5.4 can also be located new unexpected biaxial phase (See figure 5.5) with three main populations of particles oriented perpendicularly to the other two as the angular distribution functions

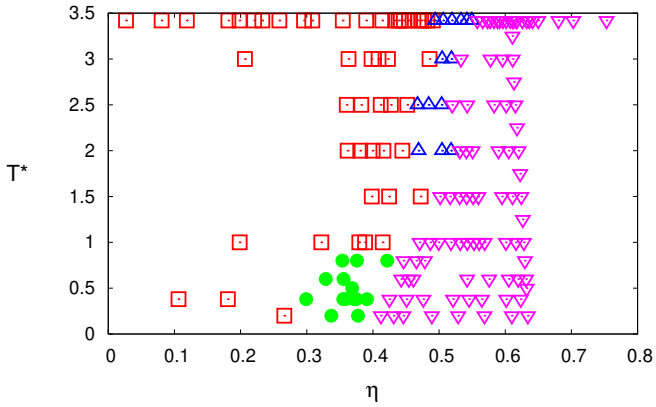

Figure 5.4: State diagram of the P potential obtained expanding a tilted configuration lowering pressure with NPTMC simulations, symbols indicate □ Isotropic, ● Biaxial, △ Columnar phase, ▽ Tilted phase.

shows. As we saw in section 3.4, at low temperature when the minimum energy in T configuration is a global minimum, we can find the uniaxial phase. But as it appears when we add to this, the repulsion in the rest of configurations, the system reaches higher ordering forming this new phase.

This is coherent with the information given by the radial distribution functions $g(r)$ and $g_2(r)$ when we compare them simultaneously. When the later reaches values close to 1 it means that most particles at these values of r are parallel, meanwhile values close to -0.5 would mean particles are oriented perpendicularly. Therefore, observing figure 5.6 we can say that particles are ordered at short distances in four main orientations. At $r^* = 0.3$ they are parallel to each other, but this changes abruptly after $r^* = 0.6$ where they are perpendicular. The small peaks before $r^* = 0.8$ and at $r^* = 1.2$ also represent particles oriented mostly perpendicular or parallel respectively to a particle set in the origin. This information is perfectly concordant with what can be observed in the snapshot,

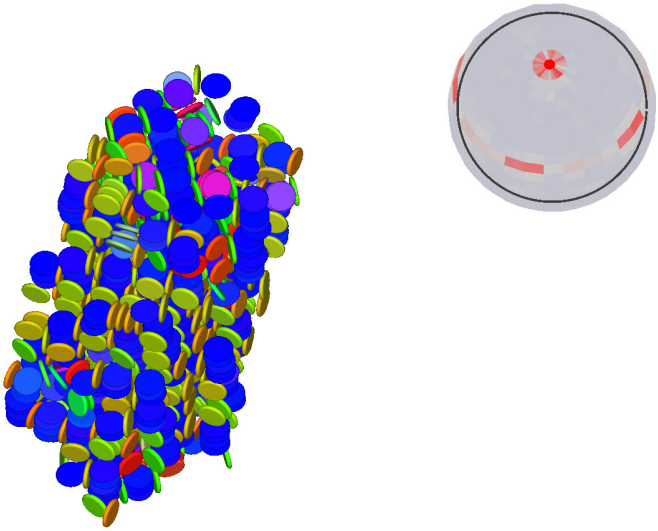

Figure 5.5: Snapshot at P=10 and T=0.38 for the P type potential (left), together with an histogram of the angular distribution of the particle orientations in 3D (colours depicting particles orientations).

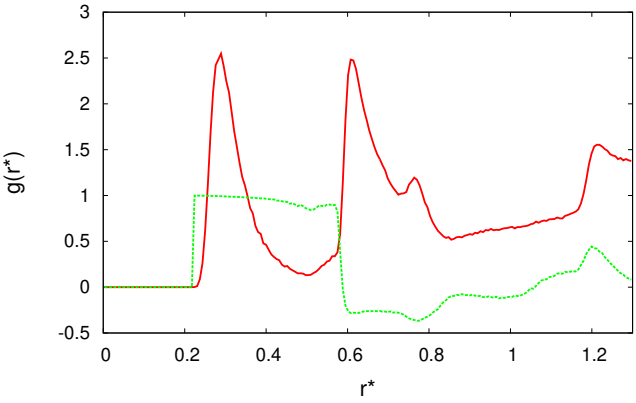

Figure 5.6: $g_2(r)$ and $g(r)$ at P=10 and T=0.38. Corresponding to a biaxial phase.

where we can observe three main populations of particles in three main orientations. Staring from any particle we will find particles of its same population oriented parallel closer than $r^* = 0.6$. Then at bigger distances particles from a second population would be oriented perpendicularly and at distances closer than $r^* = 0.8$ a third population perpendicular to both initial ones. Finally, at distances around $r^* = 1.2$ some particles from the first population still retain some degree of orientational order. This distribution functions show similar qualitative features as the ones provided in the literature for the particle arrangement known as "house of cards" [106, 158, 163], this features seem to be strengthened in the biaxial state due to higher compactness and therefore ordering and could be related to birefringence properties found in laponites [164] when they hold reminiscent order from a nematic phase.

5.4 Conclusions

To overcome the difficulty of a coarse grain model potential, to recreate particles having parts of its surface holding opposite charge at the same time it is proposed a modification of the OGBK potential trough and angular function. This modified coarse grain model shows similar functional shape to those obtained with charged beads distributed in a disk shape. The simulation results indicate that this potential easily produces the T shape conformation of particles at low temperatures, and what is even more interesting, a biaxial state at low temperatures, roughly between packing fractions $\eta = 0.3$ and $\eta = 0.4$, where we can observe three main populations of particles standing in perpendicular orientations to the rest. At high temperatures the phases obtained confirms that even after this modification of the model, the phase behaviour is similar to hard oblates spherocylinders of the same shape anisotropy $a_o = 0.15$. This makes the model deviate from expected phase behaviour of laponites where the nematic phase is expected [162]. This fact motivates the implementation of different functional forms in future studies, i.e. of Yukawa type.

Final Conclusions

The main conclusion of this thesis is that the interplay between shape anisotropy and interaction anisotropy of colloidal particles can lead to different scenarios according to thermodynamic state of interest. Through fine tuning of particles shape and interactions their self-assembly can be controlled to obtain a desired outcome. This thesis investigates the reach of specific properties of individual particles into the behaviour of the substance they compose. From all the results obtained the most important findings are concisely exposed below:

1. The ability of prolate particles in nematic liquid crystal phases to diffuse faster than their oblate counterparts, can be relatively quantified in different ways.

2. An ellipsoidal Gaussian distribution function can accurately model the apparent non Gaussianity of the diffusion of spherocylinders at intermediate times.

3. The same known phases of hard oblate spherocylinders appear at high enough temperatures for the OGBK model at shape anisotropies of 0.1.

4. Smectic-discotic state can be achieved if the edge to edge interaction is an absolute energy minimum of possible relative orientations.

5. Cubatic state can be achieved if the cross configuration interaction is an absolute energy minimum of possible relative orientations.

6. Uniaxial state can be achieved if the ”T” configuration interaction is an absolute energy minimum of possible relative orientations.

7. Oblate spherocylinders display different aggregation states in the same thermodynamic conditions if the intensity of their interactions is anisotropic.

8. Their aggregation rates increase if the more intense interaction is oriented towards the revolution axis of the oblate spherocylinder and decrease if it is oriented toward the edges of it. Provoking a subdiffusive regime in both cases at high temperatures where aggregation still occurs.

9. Aggregates of columnar shapes can be obtained in oblate spherocylinders where face to face interaction is an absolute energy minimum of possible relative orientations.

10. Aggregates of flat shapes can be obtained in oblate spherocylinders where edge to edge interaction is an absolute energy minimum of possible relative orientations.

11. The phases obtained at low density and temperature for oblate spherocylinders is dominated by anisotropies in their pair interactions, due to the formation of clusters with different shapes.

12. The proposed modification of the OGBK model is able to qualitatively reproduce the behaviour of laponite at low density and temperature. Forming new phase (Biaxial) with similar ordering to the previously known ”House of cards” structure, but higher packing fraction.

Bibliography

[1] P.-G. de Gennes, Nobel Lectures, Physics 1991-1995, ,. 1997.

[2] V. V. D. Demus, J. Goodby, G. W. Gray, H.-W. Spiess, Handbook of liquid crystals. 1998.

[3] G. Von Freymann, V. Kitaev, B. V. Lotsch, and G. A. Ozin, "Bottom-up assembly of photonic crystals," 2013.

[4] J. F. Galisteo-López, M. Ibisate, R. Sapienza, L. S. Froufe-Pérez, Á. Blanco, C. López, J. F. Galisteo-Lõpez, M. Ibisate, R. Sapienza, L. S. Froufe-Pérez, Ú. Blanco, and C. Lõpez, "Self-assembled photonic structures," Advanced Materials, vol. 23, pp. 30–69, jan 2011.

[5] T. Wöhrle, I. Wurzbach, J. Kirres, A. Kostidou, N. Kapernaum, J. Litterscheidt, J. C. Haenle, P. Staffeld, A. Baro, F. Giesselmann, and S. Laschat, "Discotic Liquid Crystals," Chemical Reviews, vol. 116, no. 3, pp. 1139–1241, 2016.

[6] L. Schmidt-Mende, A. Fechtenkötter, K. Müllen, E. Moons, R. H. Friend, and J. D. MacKenzie, "Self-organized discotic liquid crystals for high-efficiency organic photovoltaics," Science, vol. 293, no. 5532, pp. 1119–1122, 2001.

[7] R. J. B. U, O. R. Lozman, and R. J. Bushby, "Discotic liquid crystals 25 years on," Current Opinion in Colloid & Interface Science, vol. 7, no. 5-6, pp. 343–354, 2002.

[8] K. Ohta, K. Hatsusaka, M. Sugibayashi, M. Ariyoshi, K. Ban, F. Maeda, R. Naito, K. Nishizawa, A. M. de Craats, and J. M. Warman, "Discotic liquid crystalline semiconductors," Molecular Crystals and Liquid Crystals, vol. 397, no. 1, pp. 25–45, 2003.

[9] S. Kumar, "Self-organization of disc-like molecules: chemical aspects," Chemical Society Reviews, vol. 35, no. 1, pp. 83–109, 2006.

[10] S. M. Kelly and M. O'Neill, "Liquid crystals for electro-optic applications," in Handbook of advanced electronic and photonic materials and devices, pp. 1–66, Elsevier, 2001.

[11] T. Graham, "X. Liquid diffusion applied to analysis," Philosophical Transactions of the Royal Society of London, vol. 151, pp. 183–224, jan 1861.

[12] C. P. Royall and S. R. Williams, "The role of local structure in dynamical arrest," 2015.

[13] R. Brown, The miscellaneous botanical works of Robert Brown, vol. 27. Ray society, 1866.

[14] A. Einstein, "Zur theorie der brownschen bewegung," Annalen der physik, vol. 324, no. 2, pp. 371–381, 1906.

[15] M. Smoluchowski, "The kinetic theory of brownian molecular motion and suspensions," Ann. Phys, vol. 21, pp. 756–780, 1906.

[16] P. LANGEVIN, “Sur la theorie du mouvement brownien,” Compt. Rendus, vol. 146, pp. 530–533, 1908.

[17] M. J. Perrin, “Mouvement brownien et rÉalitÉ molÉculaire,” Annales de Chimie et de Physique, vol. 8ème série, no. 19, 1909.

[18] H. B. Callen., Termodinámica.

[19] J. N. c. J. Bertrán, Química Física, Vol I.

[20] P. G. Debenedetti., Metastable Liquids, Concepts and Principles.

[21] D. A. McQuarrie, Statistical Mechanics.

[22] C. Garrod., Statistical Mechanics and Thermodinamics.

[23] C. G. Gray and L. E. Gubbins., Theory of Molecular Fluids.

[24] L. L. Lee., Molecular Thermodinamic of Nonideal Fluids.

[25] D. P. L. y K. Binder, A Guide to Monte Carlo Simulations in Stattistical Physics.

[26] M. P. Allen, D. J. Tildesley, and J. R. Banavar, “Computer Simulation of Liquids,” Physics Today, vol. 42, pp. 105–106, mar 1989.

[27] B. Martínez-Haya, a. Cuetos, S. Lago, and L. F. Rull, “A novel orientation-dependent potential model for prolate mesogens.,” The Journal of chemical physics, vol. 122, no. 2, p. 024908, 2005.

[28] J. Gay and B. Berne, “Modification of the overlap potential to mimic a linear site–site potential,” The Journal of Chemical Physics, vol. 74, no. 6, pp. 3316—-3319, 1981.

[29] C. Vega and S. Lago, “A fast algorithm to evaluate the shortest distance between rods,” Computers and Chemistry, 1994.

[30] A. Cuetos and B. Martínez-Haya, "Columnar phases of discotic spherocylinders," Journal of Chemical Physics, 2008.

[31] D. Corbett, A. Cuetos, M. Dennison, and A. Patti, "Dynamic Monte Carlo algorithm for out-of-equilibrium processes in colloidal dispersions," Physical Chemistry Chemical Physics, 2018.

[32] A. Patti and A. Cuetos, "Brownian dynamics and dynamic Monte Carlo simulations of isotropic and liquid crystal phases of anisotropic colloidal particles: A comparative study," Physical Review E - Statistical, Nonlinear, and Soft Matter Physics, 2012.

[33] A. Cuetos and A. Patti, "Equivalence of Brownian dynamics and dynamic Monte Carlo simulations in multicomponent colloidal suspensions," Physical Review E - Statistical, Nonlinear, and Soft Matter Physics, 2015.

[34] I. R. M. J. P. Hansen, Theory of Simple Liquids.

[35] N. Metropolis, A. W. Rosenbluth, M. N. Rosenbluth, A. H. Teller, and E. Teller, "Equation of state calculations by fast computing machines," The Journal of Chemical Physics, 1953.

[36] D. Frenkel and B. Smit, Understanding Molecular Simulation.

[37] M. Parrinello and A. Rahman, "Crystal structure and pair potentials: A molecular-dynamics study," Physical Review Letters, 1980.

[38] M. Parrinello and A. Rahman, "Polymorphic transitions in single crystals: A new molecular dynamics method," Journal of Applied Physics, vol. 52, pp. 7182–7190, dec 1981.

[39] R. Najafabadi and S. Yip, "Observation of finite-temperature bain transformation (f.c.c. -r b.c.c.) in Monte Carlo simulation of iron," Scripta Metallurgica, vol. 17, pp. 1199–1204, oct 1983.

[40] S. Yashonath and C. Rao, "A Monte Carlo study of crystal structure transformations," Molecular Physics, vol. 54, pp. 245–251, jan 1985.

[41] D. J. Tildesley and M. P. Allen, Computer simulation of liquids. Oxford, 1987.

[42] H. Löwen, "Brownian dynamics of hard spherocylinders," vol. 50, no. 2, pp. 1232–1242, 1994.

[43] C. Vega and S. Lago, "Molecular dynamics study of propane using two simple potential models," The Journal of chemical physics, vol. 93, no. 11, pp. 8171–8179, 1990.

[44] H. Shimizu, "Effect of molecular shape on nuclear magnetic relaxation," J. Chem. Phys., vol. 37, no. 4, pp. 765–778, 1962.

[45] N. G. Almarza, "A cluster algorithm for Monte Carlo simulation at constant pressure," Journal of Chemical Physics, 2009.

[46] D. J. Ashton, J. Liu, E. Luijten, and N. B. Wilding, "Monte Carlo cluster algorithm for fluid phase transitions in highly size-asymmetrical binary mixtures," Journal of Chemical Physics, 2010.

[47] M. P. Allen, G. T. Evans, D. Frenkel, and B. M. Mulder, "Hard convex body fluids," Advances in chemical physics, vol. 86, pp. 1–166, 1993.

[48] J. P. Hansen and I. R. McDonald, Theory of Simple Liquids. 2006.

[49] L. Berthier, "Revisiting the slow dynamics of a silica melt using Monte Carlo simulations," Phys. Rev. E, vol. 76, no. 1, p. 11507, 2007.

[50] T. Abete, A. De Candia, E. Del Gado, A. Fierro, and A. Coniglio, "Static and dynamic heterogeneities in a model for irreversible gelation," Phys. Rev. Lett., vol. 98, no. 8, p. 88301, 2007.

[51] K. Martens, L. Bocquet, and J.-L. Barrat, "Connecting Diffusion and Dynamical Heterogeneities in Actively Deformed Amorphous Systems," Phys. Rev. Lett., vol. 106, no. 15, p. 156001, 2011.

[52] S. C. McGrother, D. C. Williamson, and G. Jackson, "A re-examination of the phase diagram of hard spherocylinders," The Journal of Chemical Physics, vol. 104, no. 17, p. 6755, 1996.

[53] P. Bolhuis and D. Frenkel, "Tracing the phase boundaries of hard spherocylinders," Journal of Chemical Physics, vol. 106, no. 2, pp. 666–687, 1997.

[54] R. Eppenga and D. Frenkel, "Monte Carlo study of the isotropic and nematic phases of infinitely thin hard platelets," Molecular physics, vol. 52, no. 6, pp. 1303—-1334, 1984.

[55] M. Marechal, A. Cuetos, B. Martínez-Haya, and M. Dijkstra, "Phase behavior of hard colloidal platelets using free energy calculations," Journal of Chemical Physics, vol. 134, no. 9, pp. 1–12, 2011.

[56] A. Cuetos, B. Martínez-Haya, S. Lago, and L. F. Rull, "Liquid crystal behavior of the Kihara fluid.," Physical review. E, Statistical, nonlinear, and soft matter physics, vol. 68, p. 011704, 2003.

[57] B. Martínez-Haya, A. Cuetos, S. Lago, and L. F. Rull, "A novel orientation-dependent potential model for prolate mesogens.," The Journal of chemical physics, vol. 122, no. 2, p. 024908, 2005.

[58] B. Martínez-Haya and A. Cuetos, "Columnar phases of discotics with orientation-dependent interactions," The Journal of chemical physics, vol. 131, no. 07, p. 074901, 2009.

[59] C. Care and D. Cleaver, "Computer simulation of liquid crystals," Reports on progress in physics, vol. 3, pp. 335–353, 2005.

[60] M. R. Wilson, "Progress in computer simulations of liquid crystals," International Reviews in Physical Chemistry, vol. 24, no. August 2013, pp. 421–455, 2005.

[61] S. Laschat, A. Baro, N. Steinke, F. Giesselmann, C. Hägele, G. Scalia, R. Judele, E. Kapatsina, S. Sauer, A. Schreivogel, and M. Tosoni, "Discotic liquid crystals: From tailor-made synthesis to plastic electronics," Angewandte Chemie - International Edition, vol. 46, no. 26, pp. 4832–4887, 2007.

[62] K.-S. Chu and D. Moroi, "Self-diffusion in nematic liquid crystals," in Le Journal de Physique Colloques, vol. 36, pp. C1–99, EDP Sciences, 1975.

[63] S. Hess, D. Frenkel, and M. P. Allen, "On the anisotropy of diffusion in nematic liquid crystals: test of a modified affine transformation model via molecular dynamics," Molecular physics, vol. 74, no. 4, pp. 765–774, 1991.

[64] E. de Miguel, L. F. Rull, and K. E. Gubbins, "Dynamics of the Gay-Berne fluid," Physical Review A, vol. 45, no. 6, p. 3813, 1992.

[65] S. Jabbari-Farouji and E. Trizac, "Dynamic Monte Carlo simulations of anisotropic colloids," The Journal of chemical physics, vol. 137, no. 5, p. 54107, 2012.

[66] M. Bier, R. van Roij, M. Dijkstra, and P. van der Schoot, "Self-Diffusion of Particles in Complex Fluids: Temporary Cages and Permanent Barriers," Physical Review Letters, vol. 101, no. 21, p. 215901, 2008.

[67] A. Patti, D. {El Masri}, R. van Roij, and M. Dijkstra, "Stringlike Clusters and Cooperative Interlayer Permeation in Smectic Liquid Crystals Formed by Colloidal Rods," Physical Review Letters, vol. 103, p. 248304, 2009.

[68] A. Patti, D. El Masri, R. van Roij, and M. Dijkstra, "Collective diffusion of colloidal hard rods in smectic liquid crystals: Effect of particle anisotropy," The Journal of Chemical Physics, vol. 132, no. 22, p. 224907, 2010.

[69] R. Matena, M. Dijkstra, and A. Patti, "Non-gaussian dynamics in smectic liquid crystals of parallel hard rods," Physical Review E, vol. 81, no. 2, p. 021704, 2010.

[70] A. Patti, S. Belli, R. van Roij, and M. Dijkstra, "Relaxation dynamics in the columnar liquid crystal phase of hard platelets," Soft Matter, vol. 7, no. 7, pp. 3533–3545, 2011.

[71] M. Piedrahita, A. Cuetos, B. Mart\'\inez-Haya, and B. Martínez-Haya, "Transport of spherical colloids in layered phases of binary mixtures with rod-like particles," Soft Matter, vol. 11, no. di, pp. 3432–3440, 2015.

[72] A. Fick, "Ueber Difusion," Annalen der physik, vol. 170, no. 1, pp. 59–86, 1855.

[73] T. Turiv, I. Lazo, A. Brodin, B. I. Lev, V. Reiffenrath, V. G. Nazarenko, and O. D. Lavrentovich, "Effect of collective molecular reorientations on

brownian motion of colloids in nematic liquid crystal," Science, vol. 342, no. 6164, pp. 1351–1354, 2013.

[74] S. Belli, A. Patti, R. van Roij, and M. Dijkstra, "Heterogeneous dynamics in columnar liquid crystals of parallel hard rods," The Journal of chemical physics, vol. 133, no. 15, p. 154514, 2010.

[75] A. Mura, M. S. Taqqu, and F. Mainardi, "Non-markovian diffusion equations and processes: analysis and simulations," Physica A: Statistical Mechanics and its Applications, vol. 387, no. 21, pp. 5033–5064, 2008.

[76] V. Sposini, A. V. Chechkin, F. Seno, G. Pagnini, and R. Metzler, "Random diffusivity from stochastic equations: comparison of two models for brownian yet non-gaussian diffusion," New Journal of Physics, vol. 20, no. 4, p. 043044, 2018.

[77] M. V. Chubynsky and G. W. Slater, "Diffusing diffusivity: a model for anomalous, yet brownian, diffusion," Physical review letters, vol. 113, no. 9, p. 098302, 2014.

[78] M. Matse, M. V. Chubynsky, and J. Bechhoefer, "Test of the diffusing-diffusivity mechanism using near-wall colloidal dynamics," Physical Review E, vol. 96, no. 4, p. 042604, 2017.

[79] J. Guan, B. Wang, and S. Granick, "Even hard-sphere colloidal suspensions display fickian yet non-gaussian diffusion," ACS nano, vol. 8, no. 4, pp. 3331–3336, 2014.

[80] A. Cuetos, B. Martínez-Haya, S. Lago, and L. F. Rull, "Parsons-Lee and Monte Carlo study of soft repulsive nematogens.," The journal of physical chemistry. B, vol. 109, no. 28, pp. 13729–36, 2005.

[81] A. Cuetos and B. Martínez-Haya, "Liquid crystal phase diagram of soft repulsive rods and its mapping on the hard repulsive reference fluid," Molecular Physics, vol. 113, no. 9-10, pp. 1137–1144, 2015.

[82] A. Cuetos, B. Martinez-Haya, L. F. Rull, and S. Lago, "Monte Carlo study of liquid crystal phases of hard and soft spherocylinders.," Journal of Chemical Physics, vol. 117, no. 6, pp. 2934–2946, 2002.

[83] A. Cuetos and B. Martínez-Haya, "Columnar phases of discotic spherocylinders," The Journal of chemical physics, vol. 129, no. 21, p. 214706, 2008.

[84] T. Boublík and I. Nezbeda, "PVT behaviour of hard body fluids. Theory and experiment," Collection of Czechoslovak chemical communications, vol. 51, no. 11, pp. 2301–2432, 1986.

[85] J. K. Dhont, An introduction to dynamics of colloids, vol. 2. Elsevier, 1996.

[86] A. L. Thorneywork, D. G. A. L. Aarts, J. Horbach, and R. P. A. Dullens, "On the Gaussian approximation in colloidal hard sphere fluids," Soft Matter, vol. 12, no. 18, pp. 4129–4134, 2016.

[87] G. D. J. Phillies, "In complex fluids the Gaussian Diffusion Approximation is generally invalid," Soft matter, vol. 11, no. 3, pp. 580–586, 2015.

[88] L. Berthier, "Nonequilibrium Glassy Dynamics of Self-Propelled Hard Disks," Physical Review Letters, vol. 112, p. 220602, June 2014.

[89] F. Noack, D. Demus, J. Goodby, G. W. Gray, H. Spiess, and V. Vill, Physical Properties: Diffusion in Liquid Crystals, pp. 582–593. 04 2008.

[90] A. Rahman, "Correlations in the Motion of Atoms in Liquid Argon," Physical Review, vol. 136, pp. 405–411, Oct. 1964.

[91] M. D. Ediger, "Spatially Heterogeneous Dynamics in Supercooled Liquids," Annual Review of Physical Chemistry, vol. 51, pp. 99–128, Oct. 2000.

[92] R. Richert, "Homogeneous dispersion of dielectric responses in a simple glass," Journal of Non-Crystalline Solids, vol. 172-174, pp. 209 – 213, 1994. Relaxations in Complex Systems.

[93] H. Margenau and N. R. Kestner, Theory of intermolecular forces. Pergamon Press, 1971.

[94] A. R. Leach, Molecular Modelling: Principles and Applications (2nd Edition). 2001.

[95] A. Vedani, "YETI: An interactive molecular mechanics program for small-molecule protein complexes," Journal of computational chemistry, vol. 9, no. 3, pp. 269–280, 1988.

[96] T. Kihara, "Virial coefficients and models of molecules in gases," Reviews of Modern Physics, vol. 25, no. 4, p. 831, 1953.

[97] B. J. Berne and P. Pechukas, "Gaussian model potentials for molecular interactions," The Journal of Chemical Physics, vol. 56, no. 8, pp. 4213–4216, 1972.

[98] J. G. Gay and B. J. Berne, "Modification of the overlap potential to mimic a linear site-site potential," The Journal of Chemical Physics, 1981.

[99] T. Heinemann, K. Palczynski, J. Dzubiella, and S. H. Klapp, "Angle-resolved effective potentials for disk-shaped molecules," Journal of Chemical Physics, 2014.

[100] D. Caprion, L. Bellier-Castella, and J. P. Ryckaert, "Influence of shape and energy anisotropies on the phase diagram of discotic molecules," Physical Review E - Statistical Physics, Plasmas, Fluids, and Related Interdisciplinary Topics, 2003.

[101] S. Fleming and A. Rohl, "GDIS: a visualization program for molecular and periodic systems : Zeitschrift für Kristallographie," Zeitschrift für Kristallographie, vol. 220, pp. 580–584, 2009.

[102] B. Martínez-Haya and A. Cuetos, "Columnar phases of discotics with orientation-dependent interactions," Journal of Chemical Physics, 2009.

[103] B. Martínez-Haya and A. Cuetos, "Nematic stability of discotic liquid crystals with orientation-dependent interactions," Physical Review E - Statistical, Nonlinear, and Soft Matter Physics, 2010.

[104] M. Spivak, "Calculus on Manifolds," in Lectures on the Geometry of Manifolds, pp. 81–140, WORLD SCIENTIFIC, sep 2007.

[105] S. Lang, Differential and Riemannian Manifolds, vol. 160 of Graduate Texts in Mathematics. New York, NY: Springer New York, 1995.

[106] M. Dijkstra, J. P. Hansen, and P. A. Madden, "Gelation of a clay colloid suspension," Physical Review Letters, vol. 75, no. 11, pp. 2236–2239, 1995.

[107] A. Mourchid, A. Delville, J. Lambard, E. Lécolier, and P. Levitz, "Phase Diagram of Colloidal Dispersions of Anisotropic Charged Particles:

Equilibrium Properties, Structure, and Rheology of Laponite Suspensions," Langmuir, 1995.

[108] M. Marechal, A. Cuetos, B. Martínez-Haya, and M. Dijkstra, "Phase behavior of hard colloidal platelets using free energy calculations," Journal of Chemical Physics, 2011.

[109] T. Heinemann, K. Palczynski, J. Dzubiella, and S. H. Klapp, "Coarse-grained electrostatic interactions of coronene: Towards the crystalline phase," Journal of Chemical Physics, 2015.

[110] P. D. Duncan, M. Dennison, A. J. Masters, and M. R. Wilson, "Theory and computer simulation for the cubatic phase of cut spheres," Physical Review E - Statistical, Nonlinear, and Soft Matter Physics, 2009.

[111] M. Marechal, A. Patti, M. Dennison, and M. Dijkstra, "Frustration of the Isotropic-columnar phase transition of colloidal hard platelets by a transient Cubatic phase," Physical Review Letters, 2012.

[112] A. Stroobants, H. N. Lekkerkerker, and D. Frenkel, "Evidence for Smectic Order in a Fluid of Hard Parallel Spherocylinders," Physical Review Letters, 1986.

[113] A. Nehring, T. N. Shendruk, and H. W. De Haan, "Morphology of depletant-induced erythrocyte aggregates," Soft Matter, 2018.

[114] J. Wang, M. A. Gayatri, and A. L. Ferguson, "Mesoscale Simulation and Machine Learning of Asphaltene Aggregation Phase Behavior and Molecular Assembly Landscapes," Journal of Physical Chemistry B, 2017.

[115] J. Hernández-Rojas, F. Calvo, and D. J. Wales, "Coarse-graining the structure of polycyclic aromatic hydrocarbons clusters," Physical Chemistry Chemical Physics, 2016.

[116] R. Ionov and A. Angelova, "A new type of arrangement of disc-shaped molecules in Langmuir-Blodgett films," Sensors and Actuators: A. Physical, 1995.

[117] D. Sun, H. J. Sue, Z. Cheng, Y. Martínez-Ratón, and E. Velasco, "Stable smectic phase in suspensions of polydisperse colloidal platelets with identical thickness," Physical Review E - Statistical, Nonlinear, and Soft Matter Physics, 2009.

[118] T. Iwata, R. Miyata, and A. Matsumoto, "Columnar and Smectic Mesophases Observed for Mixed Liquid Crystal Systems Using 4-Substituted Benzoic Acids," Chemistry Letters, 2013.

[119] N. Tasios and M. Dijkstra, "From 2D to 3D: Critical Casimir interactions and phase behavior of colloidal hard spheres in a near-critical solvent," The Journal of Chemical Physics, vol. 146, p. 134903, apr 2017.

[120] A. Cuetos, M. Dennison, A. Masters, and A. Patti, "Phase behaviour of hard board-like particles," Soft Matter, vol. 13, no. 27, pp. 4720–4732, 2017.

[121] M. Marechal, A. Cuetos, B. Martínez-Haya, and M. Dijkstra, "Phase behavior of hard colloidal platelets using free energy calculations," Journal of Chemical Physics, vol. 134, no. 9, 2011.

[122] K. Kroy, M. E. Cates, and W. C. K. Poon, "Cluster Mode-Coupling Approach to Weak Gelation in Attractive Colloids," Physical Review Letters, vol. 92, no. 14, pp. 1–4, 2004.

[123] E. Zaccarelli, "Colloidal gels: equilibrium and non-equilibrium routes," Journal of Physics: Condensed Matter, vol. 19, no. 32, p. 323101, 2007.

[124] G. Foffi, C. De Michele, F. Sciortino, and P. Tartaglia, "Scaling of dynamics with the range of interaction in short-range attractive colloids," Physical Review Letters, vol. 94, no. 7, pp. 1–4, 2005.

[125] W. C. Poon and M. D. Haw, "Mesoscopic structure formation in colloidal aggregation and gelation," Advances in Colloid and Interface Science, vol. 73, pp. 71–126, 1997.

[126] E. H. de Hoog, W. K. Kegel, A. van Blaaderen, and H. N. Lekkerkerker, "Direct observation of crystallization and aggregation in a phase-separating colloid-polymer suspension," Physical Review E - Statistical Physics, Plasmas, Fluids, and Related Interdisciplinary Topics, vol. 64, no. 2, p. 9, 2001.

[127] A. M. Puertas, M. Fuchs, and M. E. Cates, "Competition between glass transition and liquid-gas separation in attracting colloids," Journal of Physics Condensed Matter, vol. 19, no. 20, 2007.

[128] V. Trappe, V. Prasad, L. Cipelletti, P. N. Segre, and D. A. Weitz, "Jamming phase diagram for attractive particles," Nature, vol. 411, pp. 772–775, jun 2001.

[129] B. M. Mognetti, A. Šarić, S. Angioletti-Uberti, A. Cacciuto, C. Valeriani, and D. Frenkel, "Living clusters and crystals from low-density suspensions of active colloids," Physical review letters, vol. 111, no. 24, p. 245702, 2013.

[130] D. A. Weitz, J. S. Huang, M. Y. Lin, and J. Sung, "Limits of the Fractal Dimension for Irreversible Kinetic Aggregation of Gold Colloids," Physical Review Letters, vol. 54, pp. 1416–1419, apr 1985.

[131] M. Y. Lin, H. M. Lindsay, D. A. Weitz, R. C. Ball, R. Klein, and P. Meakin, "Universality in colloid aggregation," Nature, vol. 339, pp. 360–362, jun 1989.

[132] B. Ruzicka, E. Zaccarelli, L. Zulian, R. Angelini, M. Sztucki, A. Moussaïd, T. Narayanan, and F. Sciortino, "Observation of empty liquids and equilibrium gels in a colloidal clay," Nature Materials, vol. 10, no. 1, pp. 56–60, 2011.

[133] S. Asakura and F. Oosawa, "On Interaction between Two Bodies Immersed in a Solution of Macromolecules," The Journal of Chemical Physics, 1954.

[134] H. N. Lekkerkerker and R. Tuinier, Colloids and the Depletion Interaction. 2011.

[135] P. G. Bolhuis, A. A. Louis, and J. P. Hansen, "Influence of polymer-excluded volume on the phase-behavior of colloid-polymer mixtures," Physical Review Letters, vol. 89, no. 12, pp. 1283021–1283024, 2002.

[136] E. Zaccarelli and W. C. K. Poon, "Colloidal glasses and gels: The interplay of bonding and caging," Proceedings of the National Academy of Sciences, 2009.

[137] F. Sciortino, S. Mossa, E. Zaccarelli, and P. Tartaglia, "Equilibrium Cluster Phases and Low-Density Arrested Disordered States: The Role of Short-Range Attraction and Long-Range Repulsion," Physical Review Letters, vol. 93, p. 055701, jul 2004.

[138] P. J. Lu, E. Zaccarelli, F. Ciulla, A. B. Schofield, F. Sciortino, and D. A. Weitz, "Gelation of particles with short-range attraction," Nature, vol. 453, no. 7194, pp. 499–503, 2008.

[139] F. Sciortino and P. Tartaglia, "Structure Factor Scaling during Irreversible Cluster-Cluster Aggregation," Physical Review Letters, vol. 74, pp. 282–285, jan 1995.

[140] E. Meneses-Juárez, S. Varga, P. Orea, and G. Odriozola, "Towards understanding the empty liquid of colloidal platelets: Vapour-liquid phase coexistence of square-well oblate ellipsoids," Soft Matter, vol. 9, no. 21, pp. 5277–5284, 2013.

[141] M. A. Miller and D. Frenkel, "Competition of percolation and phase separation in a fluid of adhesive hard spheres," Physical Review Letters, vol. 90, no. 13, pp. 135702/1–135702/4, 2003.

[142] P. J. Lu, J. C. Conrad, H. M. Wyss, A. B. Schofield, and D. A. Weitz, "Fluids of clusters in attractive colloids," Physical Review Letters, vol. 96, no. 2, pp. 1–4, 2006.

[143] F. Bergaya, B. K. G. Theng, and G. Lagaly, Handbook of Clay Sience. 2006.

[144] C. Aguzzi, P. Cerezo, C. Viseras, and C. Caramella, "Use of clays as drug delivery systems: Possibilities and limitations," Applied Clay Science, 2007.

[145] R. Suresh, S. N. Borkar, V. A. Sawant, V. S. Shende, and S. K. Dimble, "Nanoclay Drug Delivery System," Internacional Journal Of Pharmaceutical Scineces and Nanotechnology, 2010.

[146] D. W. Thompson and J. T. Butterworth, "The Nature of Laponite and Its Aqueous Dispersions pH Titration of Laponite Dispersions Analysis of Laponite Dispersion Media and Measurements," Journal of Colloid and Interface Science, vol. 15, no. I, pp. 236–243, 1992.

[147] S. L. Tawari, D. L. Koch, and C. Cohen, "Electrical double-layer effects on the Brownian diffusivity and aggregation rate of Laponite clay particles," Journal of Colloid and Interface Science, vol. 240, no. 1, pp. 54–66, 2001.

[148] B. V. Derjaguin and L. D. Landau, "Theory of the stability of strongly charged lyophobic sols and the adhesion of strongly charged particles in solutions of electrolytes: Acta Physicochim URSS, v. 14," 1941.

[149] J. A. V. BUTLER, "Theory of the Stability of Lyophobic Colloids," Nature, vol. 162, pp. 315–316, aug 1948.

[150] B. Ruzicka and E. Zaccarelli, "A fresh look at the Laponite phase diagram," Soft Matter, vol. 7, no. 4, p. 1268, 2011.

[151] E. Trizac, L. Bocquet, R. Agra, J. J. Weis, and M. Aubouy, "Effective interactions and phase behaviour for a model clay suspension in an electrolyte," Journal of Physics Condensed Matter, vol. 14, no. 40 SPEC., pp. 9339–9352, 2002.

[152] B. Ruzicka, L. Zulian, E. Zaccarelli, R. Angelini, M. Sztucki, A. Moussaïd, and G. Ruocco, "Competing interactions in arrested states of colloidal clays," Physical Review Letters, 2010.

[153] S. Meyer, P. Levitz, and A. Delville, "Influence of the relative orientation of two charged anisotropic colloidal particles on their electrostatic cou-

pling: A (N,V,T) Monte Carlo study," Journal of Physical Chemistry B, vol. 105, no. 43, pp. 10684–10690, 2001.

[154] S. Mossa, C. De Michele, and F. Sciortino, "Aging in a Laponite colloidal suspension: A Brownian dynamics simulation study," Journal of Chemical Physics, vol. 126, no. 1, 2007.

[155] B. Jönsson, C. Labbez, and B. Cabane, "Interaction of nanometric clay platelets," Langmuir, vol. 24, no. 20, pp. 11406–11413, 2008.

[156] D. Ebrahimi, A. J. Whittle, and R. J.-M. Pellenq, "Mesoscale properties of clay aggregates from potential of mean force representation of interactions between nanoplatelets," The Journal of Chemical Physics, vol. 140, p. 154309, apr 2014.

[157] D. Ebrahimi, R. J. Pellenq, and A. J. Whittle, "Mesoscale simulation of clay aggregate formation and mechanical properties," Granular Matter, vol. 18, p. 49, aug 2016.

[158] G. Odriozola, M. Romero-Bastida, and F. De, "Brownian dynamics simulations of Laponite colloid suspensions," Physical Review E - Statistical Physics, Plasmas, Fluids, and Related Interdisciplinary Topics, vol. 70, no. 2, p. 15, 2004.

[159] E. G. Noya, M. M. Conde, and C. Vega, "Computing the free energy of molecular solids by the Einstein molecule approach: Ices XIII and XIV, hard-dumbbells and a patchy model of proteins," The Journal of Chemical Physics, vol. 129, p. 104704, sep 2008.

[160] N. Kern and D. Frenkel, "Fluid-fluid coexistence in colloidal systems with short-ranged strongly directional attraction," Journal of Chemical Physics, 2003.

[161] S. Kutter, J. P. Hansen, M. Sprik, and E. Boek, "Structure and phase behavior of a model clay dispersion: A molecular-dynamics investigation," Journal of Chemical Physics, 2000.

[162] P. Porion, M. Al Mukhtar, A. M. Faugère, R. J. Pellenq, S. Meyer, and A. Delville, "Water self-diffusion within nematic dispersions of nanocomposites: A multiscale analysis of1H pulsed gradient spin-echo NMR measurements," Journal of Physical Chemistry B, vol. 107, no. 17, pp. 4012–4023, 2003.

[163] M. Delhorme, B. Jönsson, and C. Labbez, "Monte Carlo simulations of a clay inspired model suspension: The role of rim charge," Soft Matter, vol. 8, no. 37, pp. 9691–9704, 2012.

[164] A. Mourchid, E. Lecolier, H. Van Damme, P. Levitz, E. Lécolier, H. Van Damme, and P. Levitz, "On Viscoelastic, Birefringent, and Swelling Properties of Laponite Clay Suspensions: Revisited Phase Diagram," Langmuir, vol. 14, pp. 4718–4723, aug 1998.